A Search for Lightly Ionizing Particles with the MACRO Detector

Thesis by

Christopher W. Walter

In Partial Fulfillment of the Requirements
for the Degree of
Doctor of Philosophy

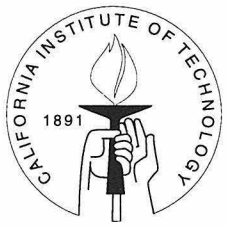

California Institute of Technology
Pasadena, California

1997
(Submitted May 27, 1997)

Acknowledgements

There are many people without whose help this thesis would not have been possible. First of all, I would like to thank my advisor Barry Barish who first started me on the path of this analysis, and my unofficial advisor Charlie Peck. Both of them have taught me an enormous amount about doing experimental physics. All of the other members of the Caltech group have been a great help. I would especially like to thank Doug Michael, Nat Longley, Eric Katsavounidis, Kate Scholberg, and Bob Nolty for many fruitful discussions. Without Bob Nolty the C++ based object oriented system for doing analysis could never have been developed.

Ed Kearns at Boston University not only designed and built the WFD system I used as the backbone of this analysis but was one of the most helpful people on the experiment in supporting my work and offering useful suggestions. The students at B.U. especially Chris Orth, Gary Ludlam, and Colin Okada were in a great part responsible for getting the MACRO detector running and in a state where useful LIP data was being taken. I am also thankful to all of the others who lived in Italy during the construction and commissioning of the experiment, especially Alec Habig, Jeff Steele, Ashutosh Sanzgiri, and Scott Nutter. Not only did these people help build MACRO, but without them, spending almost three years living in a foreign culture would have been a much more difficult experience.

All of our Italian collaborators deserve our thanks, and I am especially indebted to the Pisa Group. Gianrossano Giannini originally suggested the use of the low energy PHRASE trigger for the inputs to the LIP trigger and modified the PHRASE circuits to make this possible. Carlo Bemporad was generous enough to allow this modification and the entire INFN Pisa group has been nothing but supportive.

Finally, without my parents none of this would have been possible, and without the love and support of Kate I never could have achieved what I did. This thesis is for her.

Abstract

A search for lightly ionizing particles has been performed with the MACRO detector. A specially designed field programmable gate array based system was used for triggering, and the data analysis was performed on data recorded with a custom 200 MHz waveform digitizer system. Many novel techniques were used in the data analysis, including a neural network for timing reconstruction.

This search was sensitive to particles with charges between $\frac{1}{5}e$ and close to the charge of an electron. The detector is sensitive to particles with β of between approximately 0.25 and 1.0. Unlike previous searches both single track events and tracks buried within high multiplicity muon showers were examined.

In a period of approximately one year no candidates were observed. Assuming an isotropic flux, for the single track sample this corresponds to a 90% C.L. upper flux limit in the region of 100% efficiency of $\Phi \leq 9.2 \times 10^{-15}\ cm^{-2} sec^{-1} sr^{-1}$.

Contents

List of Figures

List of Tables

Chapter 1 Introduction

The standard model of particle physics [1, 2] described by the $\mathbf{SU(3)} \times \mathbf{SU(2)} \times \mathbf{U(1)}$ gauge symmetry has been very successful in describing the natural world. The standard model contains three doublets of leptons and their associated neutrinos, and three generations of quark doublets. To mediate forces there is the photon for electromagnetism and the heavy intermediate vector bosons for the weak force. There are eight massless gluons which carry the charge of color, and finally there is the yet undiscovered Higgs boson. Of these 24 building blocks of matter, only the quarks have electric charges which are not integral multiples of the charge of the electron.

Ever since Robert Millikan's historic experiment determined that the charge on matter comes in discrete units [3], experimenters have spent much time and effort first determining the precise value of that charge, and later trying to observe instances in nature where anything other than integer multiple version of that charge existed.

The first hint that such objects might in fact be present in nature were the results obtained from the deep inelastic scattering experiments at SLAC during the late 1960's [4]. These experiments first demonstrated that nucleons do in fact have substructure. By exploring the structure functions in these scattering experiments, it was discovered that the protons and neutrons were in fact constructed of smaller point-like partons, and that there were three of these partons in both the proton and the neutron [5].

It was soon realized that the partons observed in deep inelastic scattering experiments could in fact be described by SU(3) symmetry and the suggestion of the quark model by Murray Gell-Man [6]. Although in this model the quarks which make up the baryons and mesons have fractional charge, they are always combined in a way that results in a integrally charge baryon or meson. This is due to the fact that the quarks happen to have charges of 1/3 and 2/3. If (as in some models) there were extra quarks which had a charge of 1/6 [7], then when combining them with the normal

quarks, the resulting hadrons would have charges of 1/2.

It does not seem possible to observe a quark outside of a hadron or meson. This observation was reconciled with the quark model by the conjecture that all observed objects must be color singlets. In other words the color portion of the wave function of any collection of quarks must be a function which transforms into itself under the transformations of SU(3). It is not possible for a single quark to satisfy this requirement, and the resultant permanent binding of quarks inside hadrons is known as *confinement.*

The behavior of a quark which has been struck with another particle, with large momentum transfer, is described by the theory of *asymptotic freedom.* In this model, when a set of quarks are extremely close to each other, they act essentially as free particles. As they are separated, however, the energy density of gluons exchanged between them increases linearly with their distance. Eventually, there is enough energy to create a new quark-antiquark pair from the vacuum.

Because of asymptotic freedom, it is not possible to remove a quark from a hadron. As one quark is moved farther and farther away from its partners, eventually there is enough energy density in gluons present to form a quark-antiquark pair from the vacuum. One of these new quarks takes the place of the quark that was being removed from the original hadron and the other quark binds with the quark that was being removed to form a new meson.

Despite decades of searching no one has yet observed a quark free of its ever-present neighbors. Also, the search for electrons or other leptonic type particles with fractional charge has been in vain. These include larger and more sophisticated versions of Millikan's oil drop experiment, searches in bulk matter, experiments at accelerators, and searches in the cosmic radiation [8, 9, 10]. Nonetheless, people keep searching. Why? As of today there is no solid theoretical explanation for confinement or the lack of fractional charge in matter. A clear observation of fractional charge would be extremely important. Depending on the type of particle seen, it might mean that confinement breaks down under some circumstances or that entirely new classes of particles existed. If this were the case, then we would have an important clue as

to how to build the models we needed to describe the world as we know it.

1.1 Theoretical Motivation

Although it is true that the experimental reasons to search for fractional charge are strong (since a positive observation would have such far-reaching consequences), the same cannot be said of the theoretical motivation.

With the possible exception of very heavy GUT-scale particles with fractional charge, there seems little theoretical motivation for constructing theories with fractional charge in them. On the other hand, it is possible to construct such theories. In the middle 1980's there was a report that a team at Stanford had observed +1/3 charges on niobium spheres which were magnetically levitated. This claim was never experimentally confirmed, but there were some theorists who constructed models which would be able to accommodate such an observation.

In GUT theories it is relatively easy to accommodate fractional charge in color singlets by extending the unification group from **SU(5)** to a larger group. For example, an extension to **SU(7)** allows for charges of $\frac{1}{3}$ [11]. The extension to **SU(7)**, however, loses some attractive features of **SU(5)**. For example, in **SU(5)** there is a relationship between the three colors of the quarks and the fact that the electric charges of the quarks are in the units of $\frac{1}{3}$.

It is still possible to construct a theory with fractional charge and keep this relationship. One such model which allows for leptonic-type particles with charge $\frac{1}{3}$ e was proposed which adds an extra exact **U(1)** symmetry to nature [12]. Like other models, it extends the gauge group, this time to **SU(5)** $\times$ **SU(5)'**. Other GUT groups have been considered which allow for fractional charge, including **SU(8)** [13], **SO(14)** [14], and **SO(18)** [15]. Some theories of spontaneously broken QCD have also predicted free quarks [16], although these quarks would probably be contained in super-heavy quark-nucleus complexes with large non-integral charge.

1.2 Lightly Ionizing Particles in MACRO

This thesis presents a search for particles with fractional charge in the cosmic radiation. Particles with fractional charge deposit less energy in a detector than particles with unit charge. This is due to the fact the energy loss of a particle by ionization goes like [17]:

$$\frac{dE}{dx} \propto \frac{Q^2}{\beta^2}. \tag{1.1}$$

Here Q is the charge of the particle and β is its velocity. So, for example, a particle traveling at relativistic speed with charge of $\frac{1}{3}$ e will have an energy deposition only $\frac{1}{9}$ that of the muon. For this reason we call such particles *lightly ionizing particles*(LIPs).

The MACRO experiment is a large underground experiment located in Italy. Due to MACRO's large size, fine granularity, high efficiency scintillator, and high resolution tracking system, it is uniquely suited to look for LIPs, and in order to take advantage of this situation a special LIP trigger system has been built.

The LIP trigger allows a search for objects which interact electro-magnetically but deposit only small amounts of energy in the scintillator counters. The LIP energy threshold of about 1.2 MeV should be compared to the typical muon energy loss of about 40 MeV.

The MACRO detector is ideally suited to look for LIPs in regions of phase space that have never been explored. Although the current theoretical view is that fractionally charged particles probably don't exist, experimental answers often yield surprises.

1.3 Features of this Search

The use of this trigger allows a physics search for LIPs which is unique in many ways. Some of the main features which distinguish it are as follows:

1. Sensitivity down to $\frac{1}{5}$ equivalent fractional charge. Previous experiments have only checked for particles with charge $\gtrsim \frac{1}{3}$ [8].

2. Good acceptance from $\beta = 0.25$-1.0 . The lowest flux limits for LIPs now come from the very large water Čerenkov detector in Japan (Kamiokande)[18]. However, because of the nature of the Čerenkov process, water detectors are only sensitive to particles with $\beta \gtrsim 0.8$.

3. An extremely large area detector. The MACRO detector presents $\approx 800\ m^2$ of fiducial area to downward-going particles. The Čerenkov search at Kamiokande presents a nominal detection area of $130\ m^2$[18]. The best results from scintillator-based experiments come from even smaller detectors. The search by Kawagoe *et al.* [19] relied on a detector of only $6.25\ m^2$.

4. The possibility of searching within extremely large multiple muon bundles for fractional charge. Because of the size and granularity of the MACRO experiment, it is possible to isolate tracks located in large multiplicity muon bundles, and to check their energy deposition to see whether they are consistent with LIPs. For both smaller experiments and non-granulated experiments (such as single large volume water experiments like Kamiokande), multiple muon events are thrown out of the data sample. If fractional charge were being produced in extremely high energy collisions in the upper atmosphere, previous experiments may have missed the signature due to the particles being buried in the high-multiplicity shower.

5. Use of high resolution waveform digitizers for energy and timing reconstructions. At a trigger threshold of ≈ 1.2 MeV each scintillator counter fires at approximately 2 kHz. The use of a traditional ADC/TDC system has the problem of false starts due to this high rate (see for example [20]). A false start from a pulse just above threshold can partially gate a larger pulse happening just after the small pulse, producing a fake low ionization event.

6. Use of a high precision limited streamer tube tracking system. Previous underground experiments [18, 19, 21] did not have independent tracking systems. Since muons that clip the corners of scintillating volumes can be an important

source of background, the use of a tracking system is essential for the performance of an extremely low background search. In addition, without a tracking system it is hard to recognize the cases where the actual tracks pass between volumes and accompanying soft gamma rays enter into the scintillating volumes. This can be a source of background [21]. The use of a tracking system is also one of the reasons that MACRO can look for fractional charge in high multiplicity muon bundles.

Chapter 2 The MACRO Detector

The MACRO detector has been described in detail elsewhere [22, 23]. This chapter is designed to give the reader an overview and enough knowledge to understand the analysis that follows. This chapter emphasizes the detector elements themselves. The relevant electronic systems will be discussed in Chapter 3.

The MACRO detector was originally designed to detect GUT-mass magnetic monopoles [24]. Since these particles are expected to be very rare, the detector was designed with a large acceptance ($\approx 10000\ m^2$ sr) and redundant systems for detection. There are three main detector systems in MACRO: the scintillator system, the streamer tube system and the track-etch system. Of these three, only the scintillator and streamer tubes are relevant to this search and only they are described here.

MACRO is a international collaboration of about 150 physicists from six US and ten Italian institutions. The full list of MACRO collaborators and their institutions can be found in Appendix C.

2.1 MACRO Location

MACRO is located at the Gran Sasso laboratory in central Italy. Located under the largest peak in the Apennine mountain chain, the experimental halls of the Gran Sasso are approximately 1 kilometer underground. Figure 2.1 shows the location of the Gran Sasso laboratory in relation to Rome. The laboratory is located about 100 kilometers from Rome on the A24 highway.

Access to the lab is from the 10 kilometer long A24 highway tunnel which passes through the Gran Sasso mountain. The lab is composed of three main halls and several connecting tunnels. The layout of the laboratory is illustrated in figure 2.2. The MACRO experiment is located in Hall B , which is the middle of three large halls. The MACRO coordinate system is centered on the northern end of hall B and

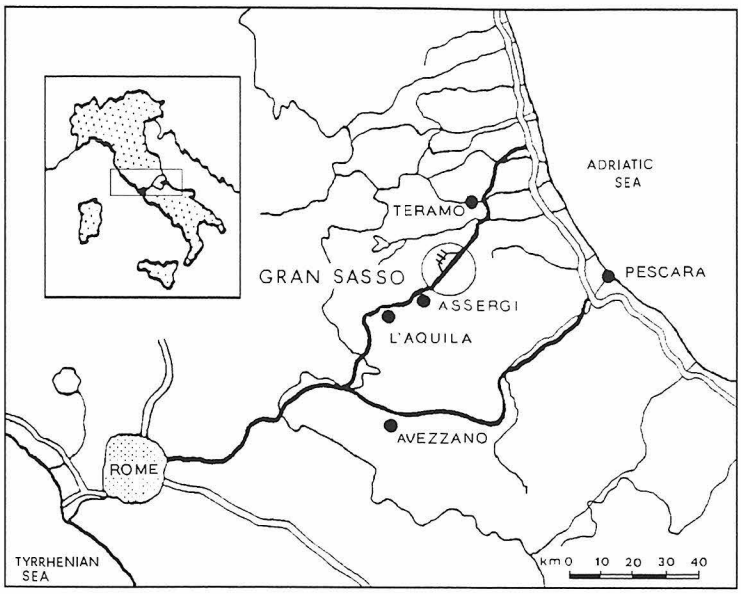

Figure 2.1: The location of the Gran Sasso laboratory. The Gran Sasso is located approximately 100 kilometers from Rome on the A24 highway.

is located at 13 ° 34' 28" E longitude and 42 ° 27' 09" N latitude. The detector has an elevation of 963 m above sea level. The minimum thickness of rock over MACRO is 1160 m (3150 m of water equivalent) and the average thickness is 1400 m (3700 meters water equivalent) [25].

There are external laboratory facilities located on the L'Aquila/Rome side of the traffic tunnel. A fiber optic link connects the underground and external laboratories for computer communications.

2.2 MACRO Detector Layout

The MACRO detector is 77 m long by 12 m wide by 9 m high. A sketch of the detector is shown in figure 2.3.

The detector can be thought of as a box completely surrounded by liquid scintillator, the lower half of which is filled with a sandwich of crushed rock and streamer tube tracking chambers. The detector is made of six identical sub-detectors called

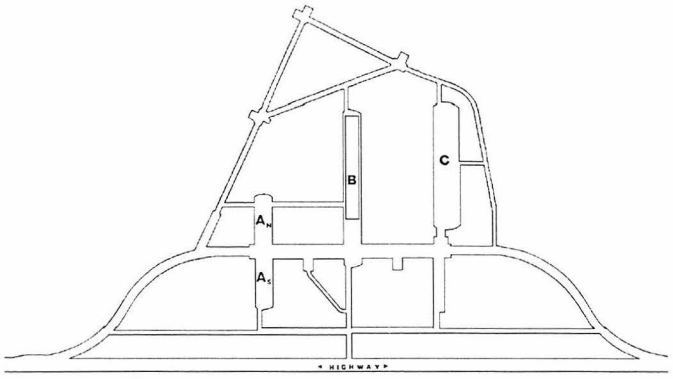

Figure 2.2: The layout of the underground Gran Sasso laboratory. There are three main halls and several connecting tunnels. MACRO is located in hall B and is drawn to scale as a box in this figure.

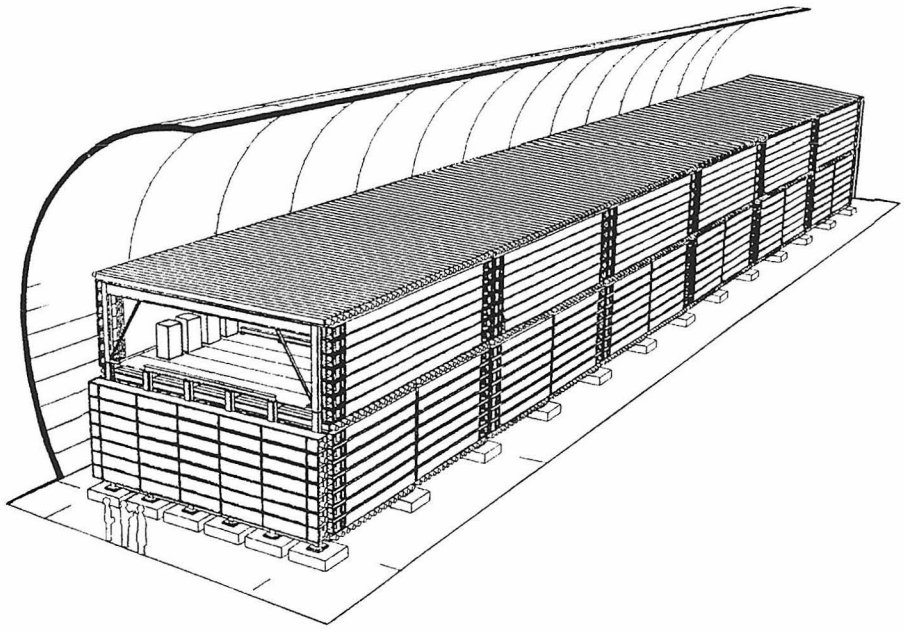

Figure 2.3: A sketch of the MACRO detector. The detector is 76 meters long by 12 meters wide by 9 meters high.

supermodules which are placed side by side. Each supermodule is 12 m long by 12 m wide by 9 m high. This substructure in the detector is visible in figure 2.3. The supermodules on the ends of the detector have walls of scintillator on their outside faces.

Each supermodule is surrounded on the top, bottom and sides by 12 m long PVC boxes filled with liquid scintillator oil. The two ends of each of these tanks are viewed with photo-multiplier tubes which measure the energy deposition of any particle that passes through them. In addition, there is a further layer of scintillator boxes inside each supermodule which separates the detector into a top and bottom half. The upper half of the detector is known as the *attico* and it holds the racks used for the detector electronics and acquisition readout. The lower half of the detector alternates between layers of crushed rock and streamer tubes. Once again the reader is referred to figure 2.3 to visualize this description.

Figure 2.4 is a closer detail picture of the lower half of one supermodule. In it one can see the position of the horizontal and vertical scintillator tanks, and also the positions of the horizontal and vertical streamer tube planes. The layers of crushed rock absorber set a minimum threshold of about 1 GeV for vertical muons to pass through the detector without stopping.

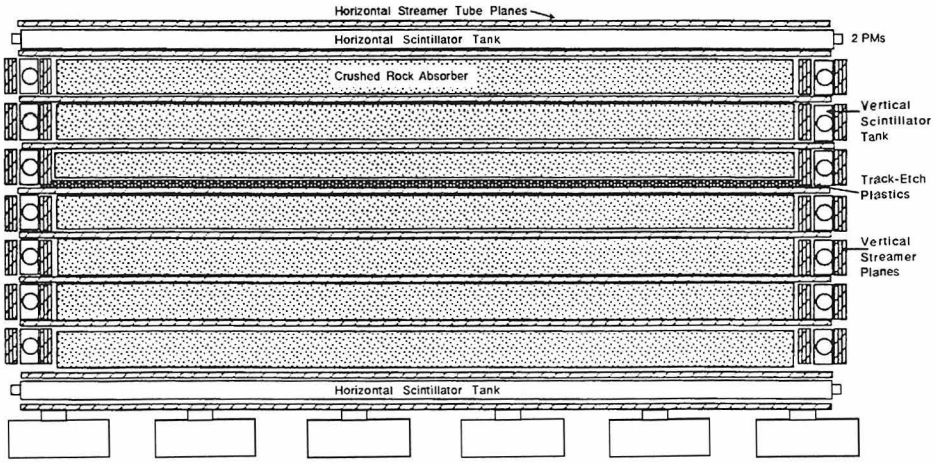

Figure 2.4: A cross section of the lower half of one supermodule.

In addition to the streamer tubes interspersed within the layers of crushed rock, there are two layers of streamer tubes above and below each horizontal scintillator plane. This can be seen in figure 2.4.

Each supermodule is triggered separately and each pair of supermodules has its own microvax for acquisition readout. These three microvaxes communicate with a central acquisition computer for event building and recording of events to disk. More details on the acquisition system can be found in [22].

2.3 The Scintillator System

The scintillator system is used to measure energy deposition. In each supermodule there are 49 horizontal scintillator counters and 28 vertical counters. There are some additional tanks on the north and south end of the detector but they are ignored in this analysis. In this analysis only the scintillator counters in the horizontal layers are used. There are 16 counters in the bottom and center layer of each supermodule and the top layer has 17 boxes.

2.3.1 Scintillator

The scintillator itself is a mix of:

- 96.4% mineral oil
- 3.6% pseudocumene
- 1.44 grams/liter PPO
- 1.44 milligrams/liter bis-MSB.

The mineral oil itself is very clear with an attenuation length of more than 20 m. The primary scintillator is the pseudocumene and the PPO and bis-MSB are wavelength shifters which shift the wavelength of the light given off by the pseudocumene up to the most sensitive region of the photo-multiplier tube's cathode at about 420 nm.

This mixture was chosen to maximize the light output for energy deposition while at the same time keeping the attenuation length long. With this mixture the attenuation length of the scintillator oil is over 12 meters.

2.3.2 Scintillator Counters

The horizontal scintillator counters used in this analysis are 12 m long and 75 cm wide. They are filled with 19 cm of liquid scintillator. The counters are constructed with 0.25" thick welded PVC. Each contains three chambers: an 11 meter long central chamber and two end chambers separated from it with a piece of 0.13" thick transparent PVC. The main chamber is filled with liquid scintillator and the two end chambers are filled with pure mineral oil. In addition to reducing sparking and discharges from the tubes (which are held at high voltage) the clear mineral oil matches the index of refraction on both sides of the clear PVC window and produces good optical coupling.

The inside of the main chamber is lined with FEP Teflon which causes all light to be totally internally reflected as long as its angle of incidence is less than 25.6°. The light produced inside the main volume of the counter is reflected and transmitted to the ends of the counter where it enters into the end chambers.

Each horizontal end chamber contains two 20 cm diameter photo-multiplier tubes. In order to increase the light collection efficiency, each is contained within a mirror to direct as much light entering the end chamber as possible onto the surface of its photo-cathode. Figure 2.5 shows schematically the positions of the phototubes and mirrors in a horizontal counter's end chamber.

2.3.3 Photo-Multiplier Tubes

The photo-multiplier tubes (PMTs) inside the horizontal counters are 20 cm diameter EMI-642s. The typical pulse from these tubes from a muon passing through 19 centimeters of scintillator oil at the center of the tanks is about 2.0 V with a rise time of about 15 ns. The phototubes have 13 dynodes arranged in a Venetian blind structure

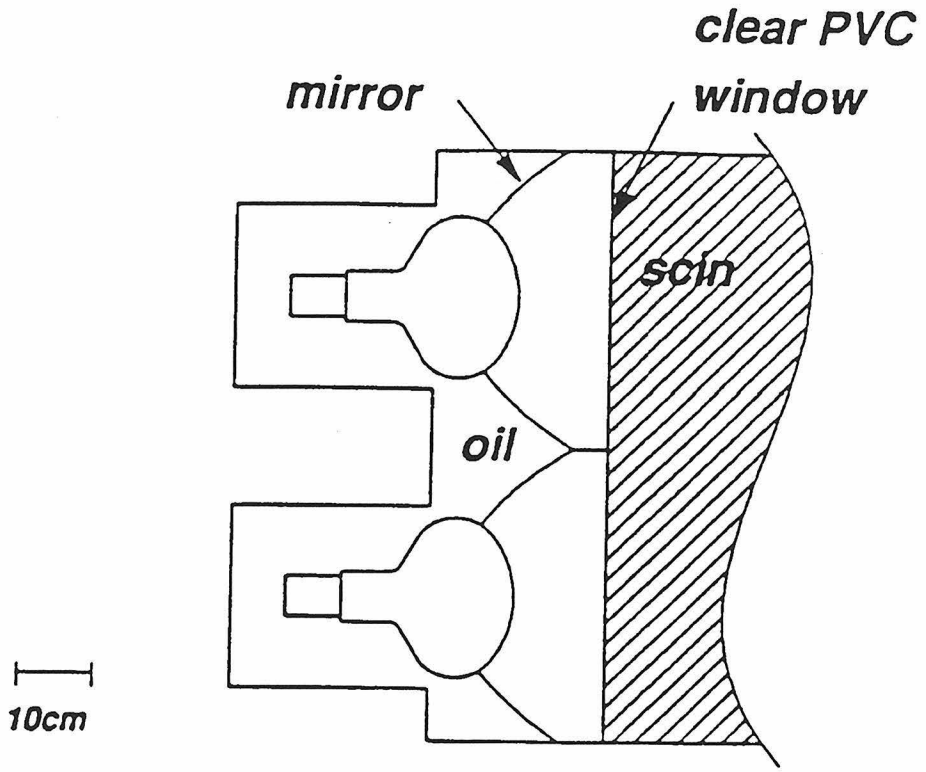

Figure 2.5: The end chamber for a horizontal counter. There are two phototubes each with a mirror to increase the light collection efficiency. The end chamber is filled with clear mineral oil to prevent high-voltage discharges and match the index of refraction with the oil in the main chamber.

and the base used in MACRO is designed to operate with typical applied voltages of -1600 V. This results in a gain which gives about -4 mV per photo-electron. The photo-cathode is held at negative voltage, which means that the signal cables can be attached without a blocking capacitor to the anode which is at ground.

2.4 The Streamer Tube System

The MACRO streamer tubes are made of extruded PVC and are heat sealed into 2.9×2.7 cm^2 cells. The anode of each cell is a metal silvered Be-Cu wire, supported every meter by plastic spacers. The cathodes are made from three of the plastic sides of the cell itself, which are coated with low resistivity graphite.

The streamer tubes are constructed in $3.2 \times 25 \times 1200$ cm^3 chambers, each of which contains eight cells. In the lower half of each supermodule, 48 streamer tube chambers are placed side by side to form the horizontal planes. There is a gap in the middle of the supermodule for the steel support structure. There is no such gap on the top of the detector and there are 51 chambers used there.

The anode wires give readout in the X direction. A second view is obtained by 3 cm pick-up strips which are placed under the streamer chambers at a 26.5° angle with respect to the wires. This layout is illustrated in figure 2.6.

The gas mixture used in the tubes is 73% helium and 27% n-pentane. The high proportion of helium in our tubes is a somewhat unusual choice. This was done because the Drell-Penning effect [26] (which can increase the energy loss of slowly moving monopoles in gaseous detectors) can be calculated for the case of helium.

The MACRO streamer tubes run in limited streamer mode [27] and the typical streamer tube high voltage is +4250 V. At this voltage the tube is within its plateau region. The plateau region is a fully efficient range which is more than 700 V wide. Figure 2.7 shows the singles rate from radioactive background as a function of high voltage applied to the wire.

At this voltage LIPs can still trigger the streamer tubes. The key to the good sensitivity of the streamer tubes even to extremely small amounts of ionization, is

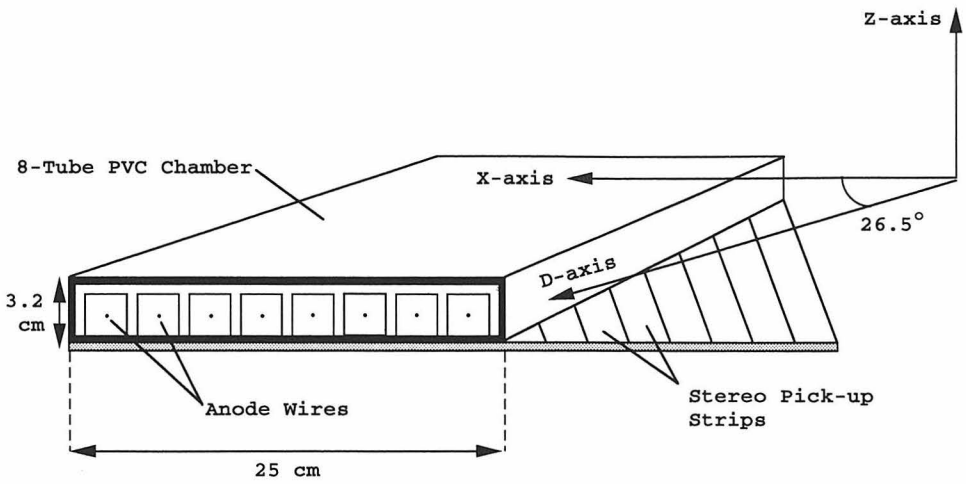

Figure 2.6: Streamer tube and pick up strip layout. There are eight cells in each chamber of streamer tubes.

that when a single ion-electron pair is produced, there is still the chance that a full streamer will be formed. A single free electron falling towards the wire is enough to start the avalanche that results in a streamer.

This probability has been measured for different gas mixtures and cell sizes to be $\gtrsim 20\%$ [28] at our operating voltages. In addition, a test was done with MACRO streamer tubes using the MACRO gas mixture. The measured single ion-pair efficiency for the MACRO tubes and gas mixture was over 30% [29]. In the next section the triggering efficiency of the streamer tube trigger will be explored.

2.4.1 Sensitivity of Streamer Tubes to LIPs

In order to calculate the efficiency of the streamer tube system, we must first calculate the average number of electron-ion pairs produced for a particle passing through a streamer tube cell. First we calculate the average energy loss for a muon passing vertically through a 3 cm cell. It should be stressed that this is a minimum ionization since there will undoubtedly be extra delta rays which enter the thin plastic of the streamer cell and the ionization in the chamber itself has a Landau tail from the delta rays that are produced.

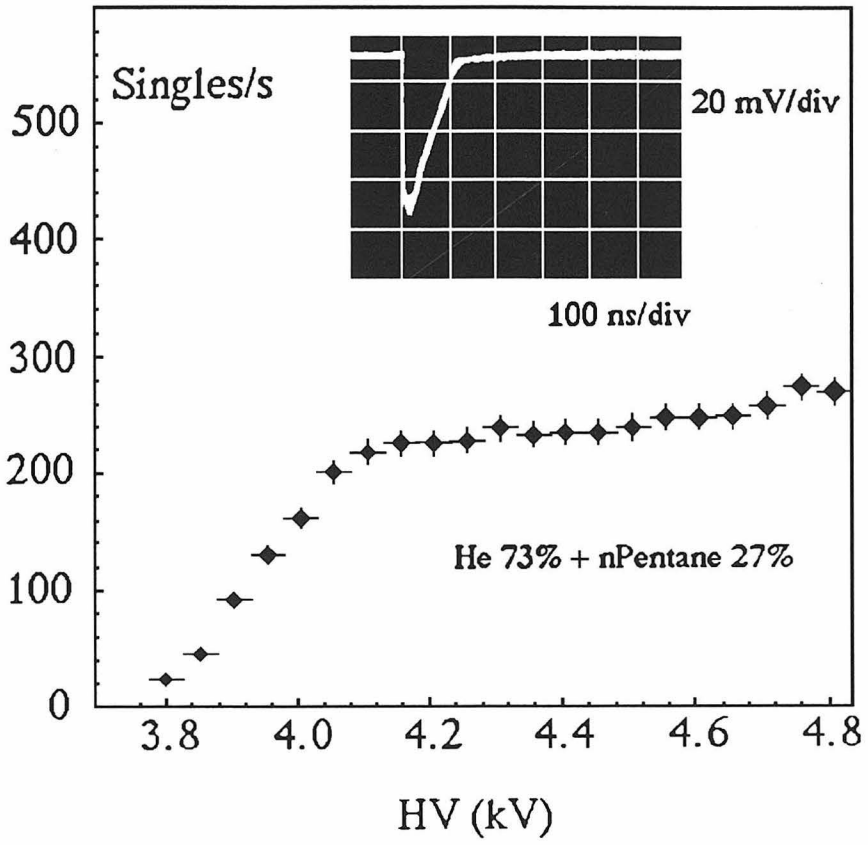

Figure 2.7: Singles rate as a function of high voltage. Above 4200 volts the tubes become 100% efficient. The inset shows the voltage output of a wire pulse in a streamer tube.

To perform this calculation we use the parameters for isobutane (C_4H_{10}) which should be similar and produce slightly less ionization than n-pentane since the density is only slightly less than n-pentane and the electron structure is similar. To our knowledge these paramaters have not been measured for n-pentane. The following parameters are used [17, 30]:

$$\begin{aligned} Density_{Helium} &= 0.178 \times 10^{-3} \ \frac{g}{cm^3} \\ \left(\frac{dE}{dX}\right)_{Helium} &= 1.94 \text{ MeV } \frac{cm^2}{g} \\ Energy\_Pair_{Helium} &= 41 \ \frac{eV}{pair} \end{aligned} \tag{2.1}$$

$$\begin{aligned} Density_{Isobutane} &= 2.67 \times 10^{-3} \ \frac{g}{cm^3} \\ \left(\frac{dE}{dX}\right)_{Isobutane} &= 2.22 \text{ MeV } \frac{cm^2}{g} \\ Energy\_Pair_{Isobutane} &= 23 \ \frac{eV}{pair} \end{aligned} \tag{2.2}$$

where Energy_Pair is the amount of energy deposition necessary to produce one ion-electron pair in the gas. In general, to determine the number of pairs (N) which are produced, we use:

$$N = \frac{\frac{dE}{dX} \times \text{Density}}{\text{Energy\_Pair}}. \tag{2.3}$$

For the two specific gases in our mixture we use equation 2.3 to determine:

$$\begin{aligned} N_{helium} &= 8.4 \text{ pair/cm} \\ N_{isobutane} &= 257.7 \text{ pair/cm.} \end{aligned} \tag{2.4}$$

So the number of pairs created in our 3 cm tube with 73% He + 27% n-pentane should be roughly:

$$\mathrm{N} = 3\ cm \times (0.73 \times 8.4 + 0.27 \times 257.7)\,\mathrm{pairs/cm} = 227. \tag{2.5}$$

The number of pairs produced by a minimum ionizing particle with charge Q should be:

$$N_{LIP} = N_{muon} Q^2. \tag{2.6}$$

So for example, a $\frac{1}{3}e$ charged particle should leave $\frac{227}{3^2} = 25$ ion-electron pairs. If we know that the probability of a single ion-electron pair causing a streamer to occur is ε, then we can calculate the probability that N pairs will create at least one streamer. The probability that none of the pairs cause a streamer is:

$$P_{notfired} = (1 - \varepsilon)^{(NQ^2)}, \tag{2.7}$$

and the probability that at least one of them started the streamer production process is:

$$P_{fired} = 1 - P_{notfired}. \tag{2.8}$$

As will be discussed in Chapter 3 the LIP trigger requires a streamer tube trigger in the lower half of the detector. There are several conditions which can cause the streamer tube trigger to be activated [22]. One of these conditions is that six out of ten of the horizontal streamer tube planes have fired. This trigger condition is the one most likely to be satisfied in the LIP analysis. Because we require all three horizontal scintillator planes, the track must also cross all of the lower streamer tube planes.

To calculate the probability that this condition is satisfied we first calculate the probability that N planes out of the ten have streamers formed in them. This probability is the probability that N planes fired, multiplied by the probability that $10 - N$

planes did not fire, multiplied by the number of ways that N out of ten planes might fire. We call the probability that N planes out of ten fired P_N.

$$P_N = \begin{pmatrix} 10 \\ N \end{pmatrix} (P_{notfired})^{10-N} (P_{fired})^N . \tag{2.9}$$

Now we can calculate the probability that *at least* N out ten planes fired. This probability is the sum of the probabilities that N fired, N+1 fired, etc.

$$P_{\geq N} = \sum_{i=N}^{10} P_i \tag{2.10}$$

For the case we are interested in, Q=$\frac{1}{5}e$, ε=30%, and a minimum of six out of ten planes must fire. The probability of a streamer tube trigger being formed in this circumstance is well over 99%. Figure 2.8 shows the probability of a trigger being formed for the case of a $\frac{1}{5}e$ charged particle as a function of ε and the number of ion-electron pairs formed by a muon.

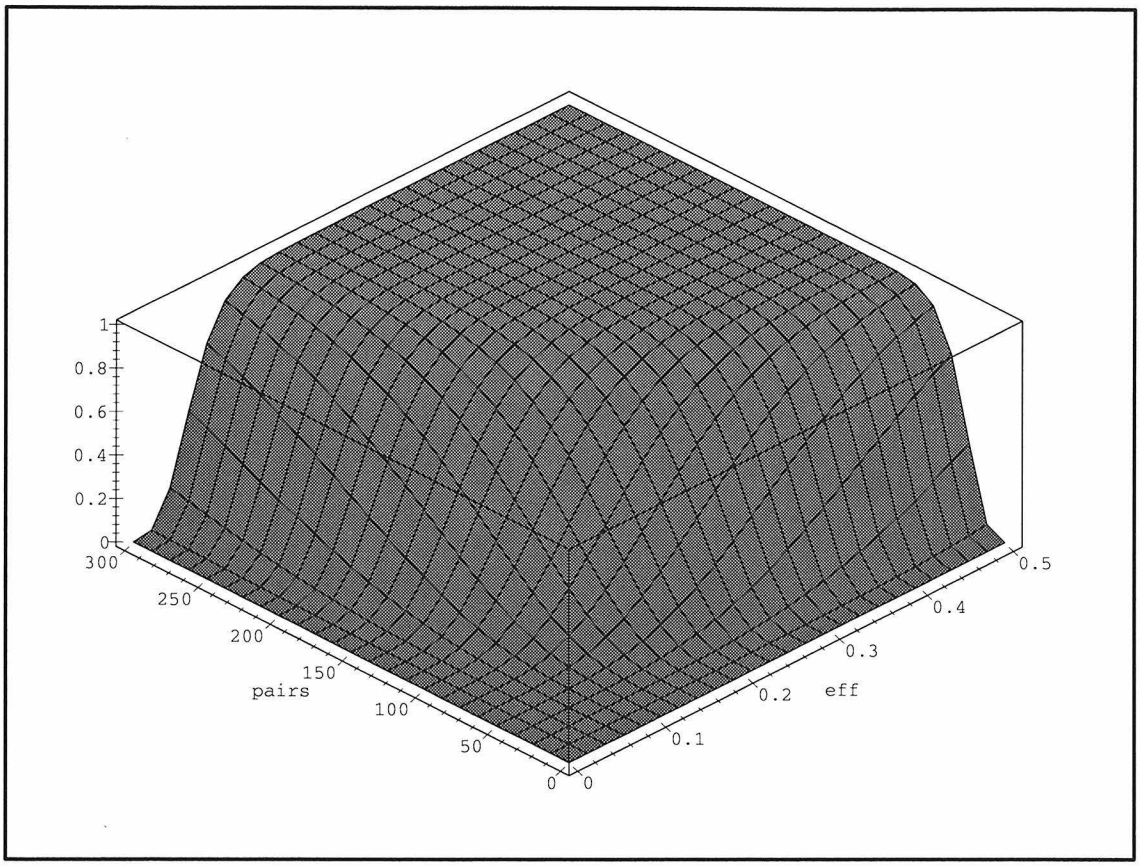

Figure 2.8: Streamer tube trigger efficiency for a $\frac{1}{5}$ e charged particle as a function of the number of ion-electron pairs produced in a streamer tube cell by a muon (axis labeled pairs) and the probability that a single ion-electron pair will cause a streamer (axis labeled eff).

Chapter 3 Electronics

The LIP search makes use of many of the sub-systems of MACRO. Most of these systems are described elsewhere. However, the LIP trigger itself, the stop master, and the waveform digitizers are described more fully in this section. The reader should refer to other references for descriptions of the PHRASE [31] and Streamer Tube [22] systems.

3.1 The LIP Trigger

The LIP trigger uses the lowest level energy-based scintillator trigger available in MACRO. The inputs are the individual box low energy triggers produced in the PHRASE (one of the gravitational collapse triggers) which have a trigger threshold of about 1.2 MeV. The LIP trigger uses XILINX-based field programmable gate array circuits to form coincidences between counters in the three scintillator faces of MACRO.

The singles rates in each counter are approximately 2 KHz. Because of timing delays in both the detector and the electronics, the coincidence time between counters can be no shorter than about 100 nano-seconds. The resulting accidental coincidence rate is approximately 10 Hz and must be reduced by further logic. This rate reduction is provided by a coincidence with the limited streamer tube system.

The LIP trigger requires that the streamer tube trigger in the lower half of MACRO has fired. If both the streamer tube and scintillator coincidence requirements are met, then the system produces a trigger which is used to stop the 200 MHz wave form digitizer system. Since a well reconstructed streamer tube track will be required in the analysis, requiring the streamer tube trigger to be present only reduces accidental coincidences and does not reduce the efficiency of the search.

In addition to triggering an event, the LIP trigger records which tanks were in-

volved in the event and presents this information to the acquisition system. Then, during the event readout, those tanks involved in the event are read out of the WFD system. More details about the LIP trigger can be found in Appendix B.

The LIP trigger is sensitive to particles with β of between 0.25 and 1.0 . Figure 3.1 shows the triggering efficiency as a function of β. The efficiency was calculated with a Monte Carlo.

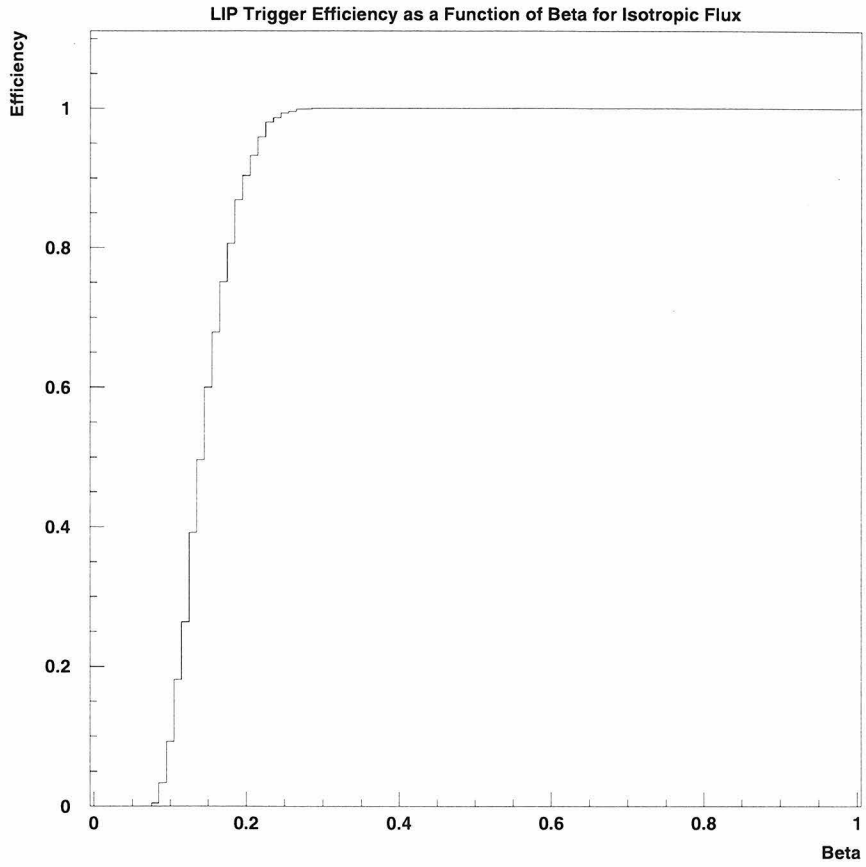

Figure 3.1: The triggering efficiency of the LIP trigger as a function of β.

As is described more fully in Appendix B the LIP trigger is designed to wait for 6.4 μsecs after the scintillator coincidence for a trigger from the streamer tube system. The LIP trigger was designed with the understanding that the streamer tube signal would always arrive long enough after the passage of the particle through the detector

that the LIP trigger would have already created the scintillator coincidence.

In fact, in high-multiplicity muon events, the streamer tube trigger can arrive during the time that the scintillator coincidence is being formed in the LIP trigger. These events are characterized by very large numbers of hits in the streamer tube system. If the streamer tube signal arrives at the LIP trigger too early then the efficiency for triggering is no longer 100%. Figure 3.2 shows the measured efficiency for the LIP trigger as a function of event multiplicity. The measured efficiency is the efficiency that the LIP trigger in every supermodule involved in the event fired. For the highest multiplicity examined in this thesis the triggering efficiency is 60%.

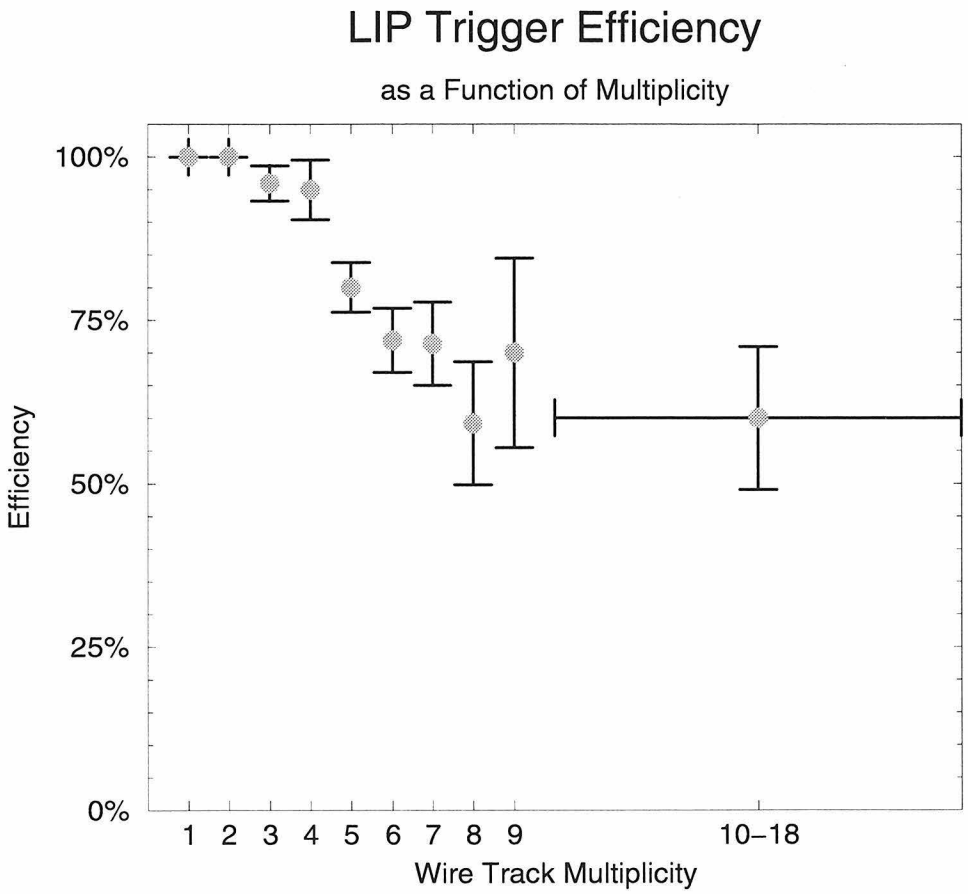

Figure 3.2: The efficiency that the LIP trigger in every supermodule involved in the event fired as a function of the track multiplicity of the event. The streamer tube trigger for large multiplicity events sometimes arrive at the LIP trigger before the scintillator coincidence has been formed.

3.2 The Waveform Digitizer

The waveform digitizers (WFDs) and their read-out scheme are also described in other references [32, 33]. For the purposes of understanding this search, it is enough to have a basic understanding of the operation.

The WFDs are a custom-built 200 MHz VME-based system. Each WFD card has four channels and each channel has four inputs. The four inputs of each channel are fanned in to one single flash ADC. It is possible to determine which input is firing, however, since a discriminator records which inputs have passed a ± 2.5 mV threshold on any given sample. Each end of a scintillator tank needs its own WFD input, and one WFD card can handle eight MACRO tanks. Figure 3.3 shows the fan-in scheme used in MACRO.

Every five ns , each channel which has at least one input over threshold is digitized by an eight-bit flash ADC. Every 20 ns these ADCs are written into a memory buffer along with a time stamp. The data are recorded and readout zero-suppressed. The time stamp allows the full time information to be reconstructed. By only digitizing the analog signal when it is over voltage threshold, the effective depth of the WFD card's memory in time is increased.

When a "STOP" signal arrives at the WFDs, they immediately cease digitizing. Then, they write into a register on the WFD board the address in memory that the last digitized data was written. Every WFD board is stopped simultaneously. Later, when the acquisition system is ready to read out the WFD system, the memory address from the register is read out and the data starting at this point in memory is transferred over the VME bus to MACRO's VME based micro-Vax. At present 1 ms of data is transferred for each channel for which a trigger has been requested.

At the end of an event a "START" signal is sent to the WFDs and they resume digitizing and recording data.

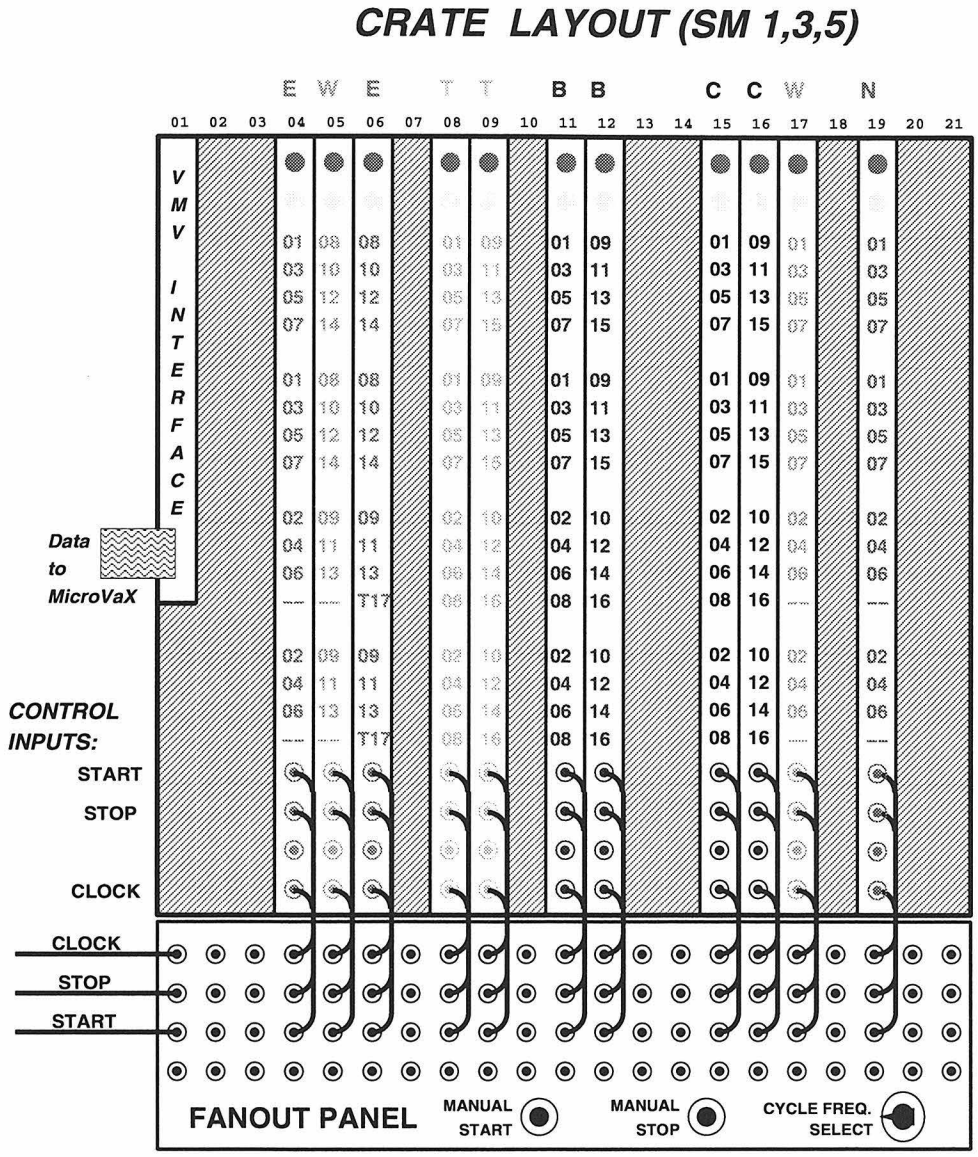

Figure 3.3: The fan-in scheme for the WFD system. The above diagram represents one crate of WFDs, which is responsible for digitizing the signals from one entire supermodule. Each card can handle four tanks. The B,C,T,E,W,N in the diagram stand for bottom, center, top, east, west, and north faces respectively. The tank numbers are shown for each input of each card. For example, the first card accepts inputs from tanks 1, 3, 5, and 7 of the east face. Since there are two sides to each tank, each has two inputs. Also shown in this figure is the cabling for the global STOP, START, and CLOCK signals.

3.3 The Stop Master

The stop master is also described in detail elsewhere [34]. In order to understand this search, it is only necessary to understand the basic theory of operation of the stop master.

The job of the stop master is to manage the trigger signals from all of the subsystems which want to readout the waveform digitizer system (e.g., the LIP, and Slow Monopole Trigger).

When the first trigger arrives at the stop master, it starts a counter and counts for 1 ms. At the end of this time, a "STOP" signal is generated and sent to the WFDs. The stop master also records the relative times of later triggers that arrive at the stop master. During the data acquisition these times are read out and later can be used to determine exactly where in the 1 milli-second of data the feature that caused the trigger to occur is located.

Chapter 4 Calibration

In order to use the WFDs effectively to both reconstruct the amount of energy deposited in the scintillator volumes, and the position in the tank where the energy was deposited, each channel of the WFDs and its associated counter must be calibrated.

The calibration procedure yields the relationship between the amount of charge measured in each scintillator counter, and the amount of energy lost by a particle. It also produces the timing offsets needed to calculate the position of passage through a counter of a particle.

The techniques used for calibration in this analysis are quite different than those used for other analysis in MACRO. For the energy calibration, most MACRO analyses use a relationship between the signal sizes observed and the amount of energy lost by muons which pass though the MACRO counters. This calibrates the tanks using energies on the order of 40 MeV.

However, in this analysis we are concerned with typical energy losses of around 1 to 5 MeV. Because of this, instead of using muons, naturally occurring low energy γ lines in this energy range are used. In practice, the muons are used to make a provisional energy calibration and then the low energy γ lines are used to refine this calibration. This technique is described in detail in section 4.1.

Throughout this discussion we assume that in the range of energies between 1 and 40 MeV there is a linear relationship between the energy lost by a LIP which passes through scintillator and the amount of charge measured by the WFDs. Effects which could cause this assumption to be invalid include scintillator saturation, and non-linearities in the WFD system. Such effects cause the calibration constants to differ in accuracy as a function of energy. Chapter 6 will show that no more than 10% of extra smearing of the accuracy of the calibration constants are introduced.

The first step to calculate the amount of energy deposited in a scintillator volume is to reconstruct the amount of charge measured by the photo-multiplier tubes in

the event. To calculate the amount of charge deposited in an event, the area below the voltage waveform as recorded by the WFD is integrated. The area under the waveform is proportional to the charge collected by the phototube. This technique is illustrated in figure 4.1.

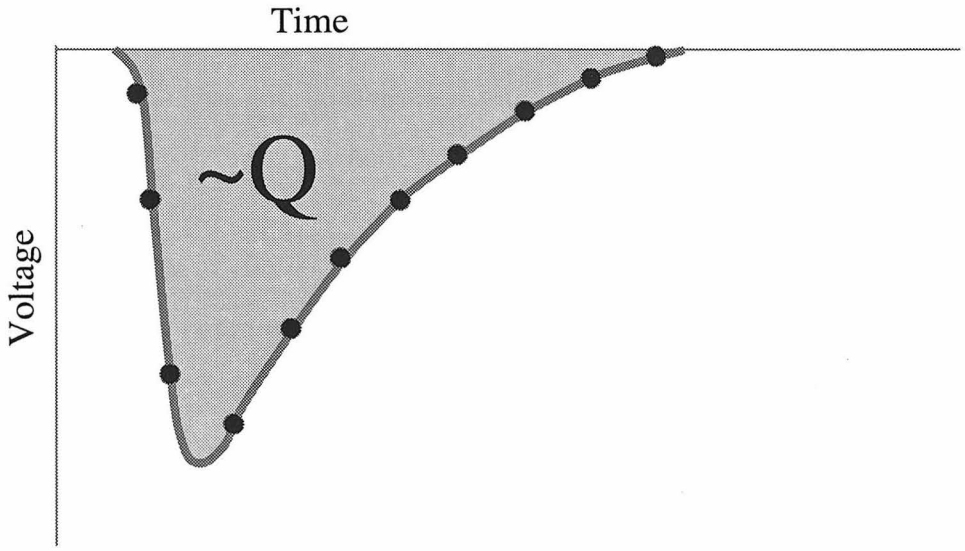

Figure 4.1: The technique used to determine the charge left by a pulse. The area underneath the waveform is integrated. The result is proportional to the charge.

In order to absolutely calibrate the energy scale, both low energy and high energy calibration points are used. On the high energy side ($\approx$ 40 MeV) the distribution of the energy deposition caused by muons which transverse the detector is used, while on the low energy side, the energies of several low energy (1-3 MeV) γ lines from natural radioactivity coming from the walls of the hall and the structure of the detector are used. It is important to note that both of these sources are present in the normal data so no special calibration runs are required.

For the case of a relativistic particle which passes through a scintillator volume, the amount of charge deposited is proportional to the path length of scintillator transversed. In order to account for the effect of particles traversing the counter at different angles, the energy in each tank is normalized to the energy loss of a particle passing through 19 cm of scintillator, the vertical thickness of the liquid scintillator.

The amount of charge measured at each phototube is also a function of where the energy is deposited. This is due to the fact that the light is attenuated by the liquid scintillator mixture in the tank, with an attenuation length of about 12 m. This is illustrated in figure 4.2 which shows an estimate of the number of photo-electrons (which is proportional to the charge collected) collected at one of the phototubes as a function of the distance away from the phototube. This function of position is known as the *response function* and is measured individually for each tank. The function is used to normalize the energy loss of a particle to that of one which passes through the center of the tank.

The position reconstruction, on the other hand, requires fitting the relative times of occurrence of the leading edges of the pulses reaching each side of the tank, and determining the position by subtracting the times at which each pulse arrives at the two ends of a scintillator tank.

In this analysis a simple linear fit of the leading edges of the pulses is used to simulate a constant fraction trigger [17, see chapter 17]. This rough guess is then refined by use of a neural network which is trained by using the streamer tube positions, and learns to do the tasks normally assigned to time walk corrections. The neural network produces better agreement with the streamer tube data than does our traditional TDC system. Once again, in this system no special calibration runs are required. All of the information needed for calibration is contained in normal running.

It should be noted that the streamer tubes alone can be used to determine the position of a particle which passes through a tank. However, the agreement between the position as reconstructed by the streamer tubes and scintillator system is an important check in the analysis procedure.

The following sections examine both the energy and timing calibrations in more detail.

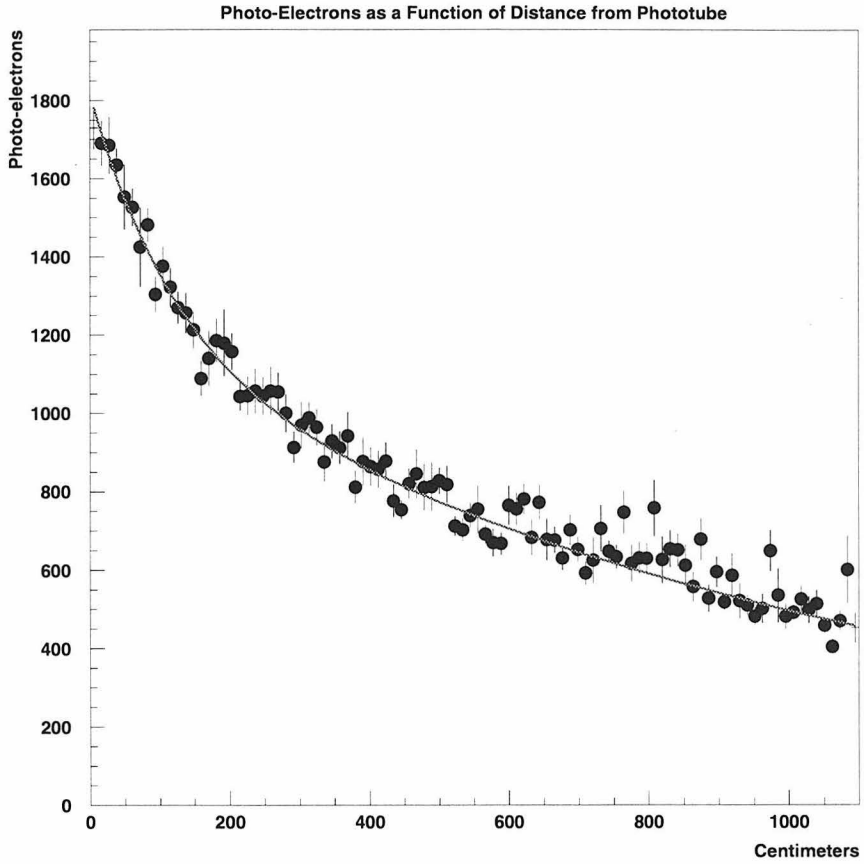

Figure 4.2: The number of photoelectrons in a scintillator box measured as a function of distance from the phototube in centimeters. The number of photoelectrons has been normalized to a 19 cm path length. The curve is fit by two exponentials: A long component of the attenuation length which is about 12 m ; and a shorter component which is about 1 m.

4.1 Energy Reconstruction

First of all, it is important to have an idea of the relevant energy scale for the LIP search. While previous searches have restricted themselves to $\frac{1}{3}$ equivalent charge, this search attempts to reach $\frac{1}{5}$ the charge of an electron. For muons with average path lengths through our detector, this is equivalent to an energy deposition of about

$$40 \text{ MeV} \times \left(\frac{1}{5}\right)^2 \approx 1.6 \text{ MeV} \tag{4.1}$$

in each scintillator box. In order to be able to reconstruct LIPs which pass through MACRO, it is necessary to reconstruct energies between 1.5 and 40 MeV. Most of the relevant signal region of this search ($\frac{1}{5}\epsilon$ to $\frac{1}{3}\epsilon$) fall between 1.5 and 5 MeV.

Figure 4.3 shows the energy loss of muons as measured by one scintillator counter in MACRO. This distribution (especially its peak) gives a convenient high energy point for calibration. There also exist several low energy γ lines in the natural radioactivity of the Gran Sasso.

4.1.1 Natural Radioactivity Sources

Below 5 MeV the Gran Sasso laboratory is bathed by low energy γ-rays which originate from the walls and floor of the tunnel, and the materials of the detector itself. They are dominated by the strong line from ^{40}K at 1.46 MeV and the decay chains of the naturally occurring ^{232}Th and ^{238}U. In the ^{232}Th decay chain one of the most intense (and most relevant) lines comes from $^{208}_{81}$Tl. It produces a 2.6 MeV γ-line from the radioactive decay process:

$$\begin{aligned} &{}^{208}_{81}\mathrm{Tl} \\ &\quad\hookrightarrow\ {}^{208}_{82}\mathrm{Pb}^{*} + \beta^{-} + \overline{\nu_e} \\ &\qquad\hookrightarrow\ {}^{208}_{82}\mathrm{Pb} + \gamma\ (2.6\mathrm{MeV}). \end{aligned} \tag{4.2}$$

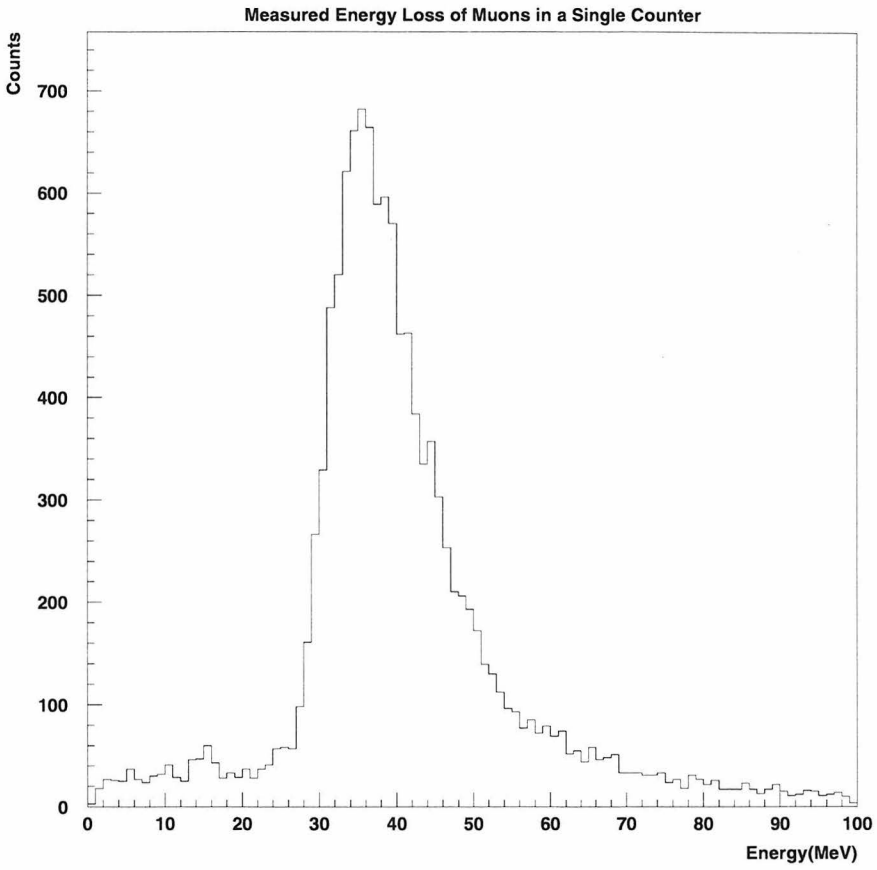

Figure 4.3: The measured energy loss for muons in one tank in MACRO.

Figure 4.4 [35] is an energy spectrum of the naturally occurring radioactive background in the Gran Sasso tunnel. This spectrum was taken with a small (7.5 cm radius, 10.0 cm length) NaI detector. It should be stressed that this spectrum was taken in an open hall and *not* inside the MACRO detector itself. Because of this fact, the relative proportions of the various radioactive elements will not necessarily be the same inside a MACRO scintillator volume. In particular, the amount of ^{40}K present may be different since it occurs in the PMT glass among other places.

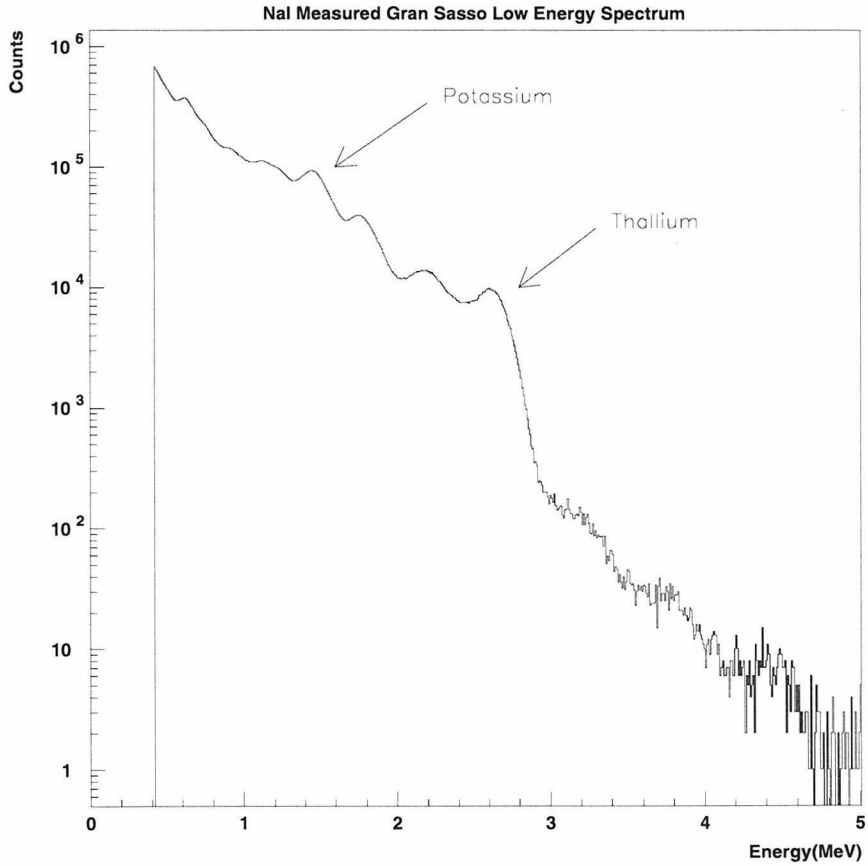

Figure 4.4: The naturally occurring radioactive background energy spectrum of the Gran Sasso hall as measured by a NaI detector. The large peaks from potassium at 1.46 MeV and thallium at 2.6 MeV are clearly visible.

In figure 4.4 the large peak from ^{40}K at 1.46 MeV is clearly visible and the last

large peak before the sudden drop off at about 3.0 MeV is due to the smearing together of the dominant $^{208}_{81}$Tl line at 2.6 MeV and a few other less intense lines.

4.1.2 Monte Carlo of Radioactive Background and Detector Response

In order to have an absolute low energy calibration, it is imperative to accurately simulate the apparatus and incorporate several important physical effects. These are:

- The detector size and geometry. The energy loss mechanism is Compton scattering, and the larger the detector, the less likely the γ is to escape the detector before losing all of its energy.

- The number of photons produced by the scintillating material in the detector. If the detector only produces a small amount of light, the resolution will be dominated by photo-electron statistics. In this case the resolution goes like the square root of the number of electrons produced at the PMT. This will determine how clearly peaks in the spectrum can be separated from each other.

- Any saturation effects that take place either in the scintillator itself or in the PMT. If the scintillator becomes locally saturated (because the local rate of energy loss is so high that there are no longer any free scintillation molecules available [17, see chapter 7]), then the amount of light produced will not be proportional to the amount of energy deposited.

To determine the absolute energy scale for MACRO scintillator counters a full GEANT [36] simulation has been performed both for the small NaI detector which took the background spectrum and for a full-size horizontal MACRO tank. The purpose of first simulating the smaller NaI detector was to verify that the simulation was working correctly and to set the relative numeric proportions of the three decay chains of ^{40}K, ^{232}Th, and ^{238}U. Once these values were set, the same proportions were used with the geometry and materials of a MACRO tank. As was pointed out

before, there is in fact no *a priori* reason to assume that these ratios will be the same inside of a scintillator volume itself. However, using the same relative proportions of ^{40}K, ^{232}Th, and ^{238}U in both the NaI and scintillator Monte Carlos produces spectra which are consistent with both experimentally measured spectra.

The MACRO tank spectrum looks qualitatively different from the NaI spectrum because the amount of light produced is much less, which causes several lines to smear together and appear as only two broad lines. Also the scintillator saturates differently from NaI which causes the amount of light produced and detected to not be proportional to the amount of energy deposited.

Table 4.1 contains a list of the energies of the γ-ray lines used in the Monte Carlo, organized by the decay family. The relative intensities within each decay family are set assuming all of the daughter states are in equilibrium.

Energy in MeV of γ Lines for Each Family		
Uranium	Thorium	Potassium
0.609	0.583	1.461
0.769	0.911	
0.935	0.960	
1.120	2.614	
1.238		
1.378		
1.400		
1.509		
1.728		
1.764		
1.848		
2.117		
2.204		
2.445		

Table 4.1: Energies of lines used in the low energy Monte Carlo.

NaI Monte Carlo: In the NaI simulation an estimate for the light output was used based on commonly used NaI detectors and then was adjusted until the resolution of

the lines agreed with the measured spectrum in figure 4.4. The resulting resolution is consistent with typical NaI detectors. Also, the relative proportions of the three families of radioactive decay chains were adjusted until the relative heights of the peaks in the spectrum matched those in figure 4.4.

Figure 4.5 is the result of the NaI Monte Carlo superimposed on the measured NaI spectrum that was already presented in figure 4.4. The comparison of the calculated with the observed spectrum indicates that the calculated precision is sufficient for our purposes. Although the absolute normalization is not exactly correct, it is the positions of the peaks, and the shape of the spectrum which is most important. Also, as was already pointed out, there is no reason to believe that the relative proportions of the families of radioactive decay chains will be exactly the same in the detector and in the hall. Since the purpose of the NaI Monte Carlo is to determine the ratios to use in the MACRO detector Monte Carlo, general agreement is good enough.

One important thing to note is that there is a host of very low energy γ lines and α-rays which are not simulated here. Because of the small amount of light, they are all smeared together in the measured spectrum. This has been phenomenologically approximated by adding a falling exponential to the produced spectrum.

MACRO Scintillator Counter Monte Carlo: Using the same ratios of radioactive families and using the materials and geometry of a MACRO counter, the simulation was then run again. The number of photo-electrons per MeV was adjusted until the widths of the peaks were consistent with what is observed in the data.

In the case of horizontal counters, this number was about 30 photo-electrons per MeV and is consistent with previous calculations [37]. This corresponds to a resolution of

$$\frac{\Delta E}{E} = 18\% \left(\frac{1 \text{ MeV}}{\text{E}}\right)^{\frac{1}{2}}. \tag{4.3}$$

Once again, a phenomenological exponential was added to the generated spectrum in order to simulate the many low energy lines which are not individually included.

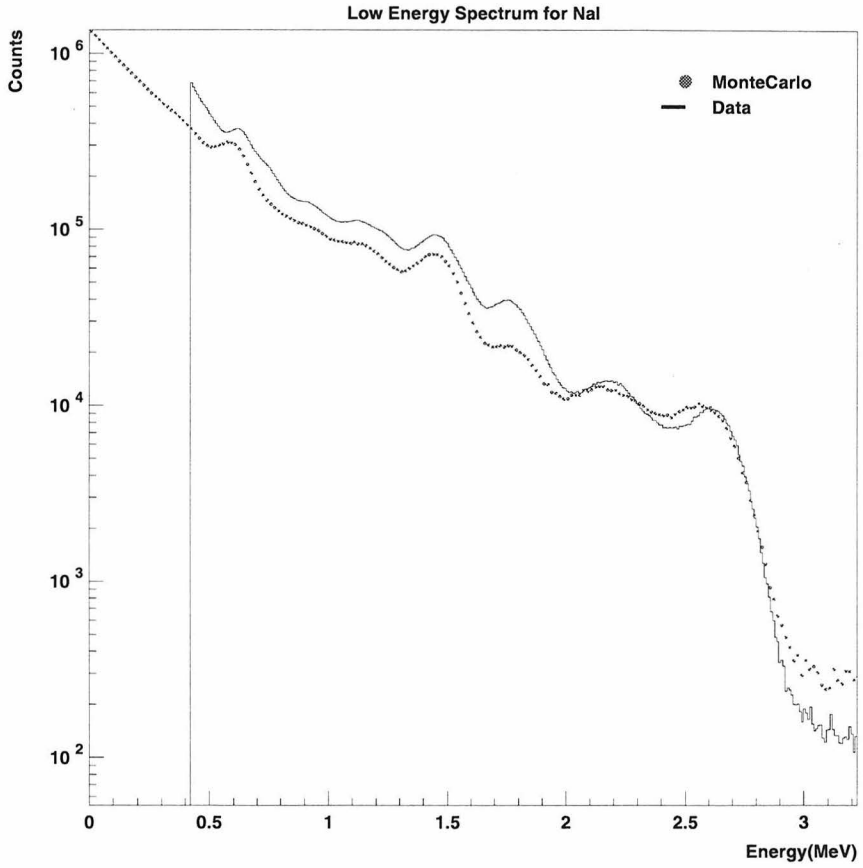

Figure 4.5: Result of the NaI Monte Carlo superimposed on the measured NaI spectrum. The measured spectrum was presented earlier in figure 4.4.

Figure 4.6 shows the result of the scintillator Monte Carlo. This spectrum has been fit to a falling exponential and two gaussians. The same fit is done to the real data, and the normalization for each tank is determined by looking at the ratios of the values of the fits to the gaussians between the real data and the Monte Carlo.

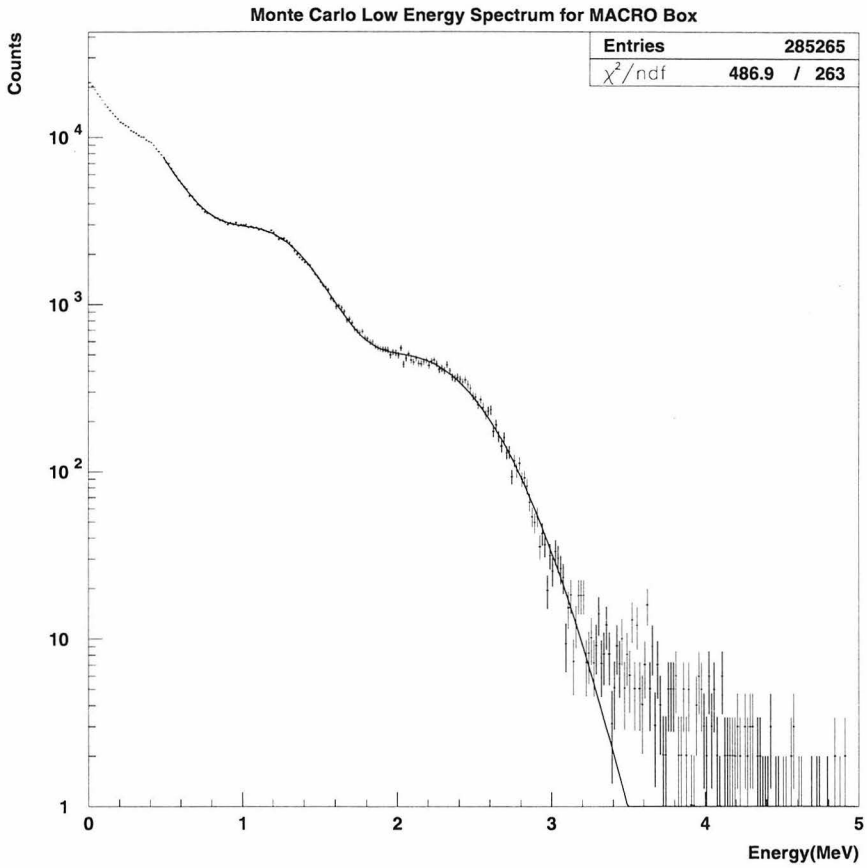

Figure 4.6: Result of the MACRO scintillator box Monte Carlo. The fit to the two peaks (1.15 MeV and 2.2 MeV) gives the absolute energy normalization which will be used to normalize the real data.

The spectrum produced by the Monte Carlo for the MACRO scintillator counter has fewer features than the spectrum for the NaI detector. This is because the smaller number of photons which reach the phototubes results in worse resolution and causes lines to smear together.

For this method of calibration, another important effect must be taken into account: scintillator saturation. If the effect were neglected, the calibration constant (which converts between estimated photo-electrons and energy) would be underestimated by 10-15%.

The γ-rays which enter the tank lose energy mostly by Compton scattering (*i.e.* the scattering off atomic electrons). The typical energy of the electrons that are produced is between 50 and 200 KeV. Figure 4.7 is a distribution of the initial kinetic energies of the Compton electrons made in this process. Electrons of this energy lose energy at a higher rate than minimum ionizing particles and stop very quickly (see figure 4.8).

The actual details of light production and scintillator saturation are quite complicated and the reader is referred to [17, 36, 38] for more information.

The scintillation characteristics of the MACRO scintillator have been measured [39]. One parameterization of scintillator linearity is Birk's formula [17, 36, 38], it can be expressed as follows:

$$\frac{dL}{dX} = \frac{A\frac{dE}{dX}}{1 + \frac{\kappa}{\rho}\frac{dE}{dX}}. \tag{4.4}$$

In equation 4.4 A and κ are characteristic constants of the scintillator: κ parameterizes non-linear response, and ρ is the density of the mineral oil. The measured value of κ for MACRO scintillator is 11.6 ± 0.6 mg cm^{-2} MeV $^{-1}$ [39]. These constants are used in the GEANT simulation to properly simulate the measured energy spectrum.

The effect of this nonlinearity is to move the 2.6 MeV peak in the spectrum down to 2.2 MeV. There are also higher-order versions of Birk's formula which contain more than one non-linearity parameter. We have not used them here but have instead relied on equation 4.4.

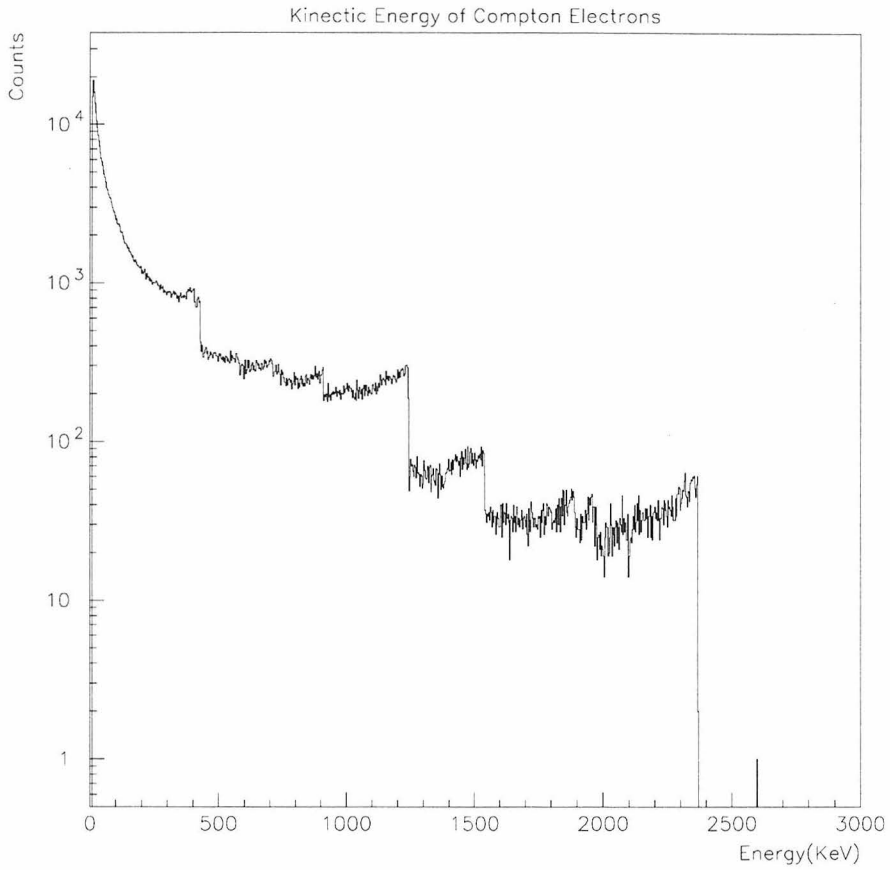

Figure 4.7: The distribution of the initial kinetic energy of the electrons produced by Compton scattering. This distribution was generated by the same Monte Carlo that produced the scintillator counter measured energy distribution. There are several energies of gamma rays and the Compton edge for each energy is clearly visible in this figure.

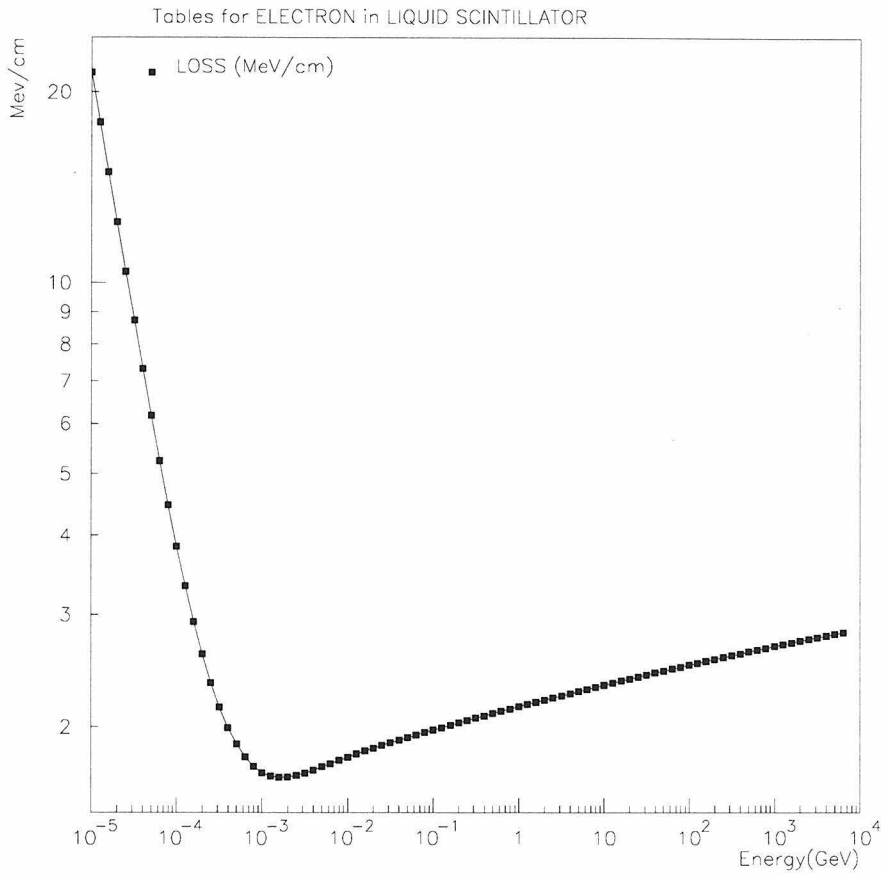

Figure 4.8: The energy loss of electrons in scintillator. The horizontal energy scale is in GeV. Most of the electrons have initial kinetic energies of a few hundreds of keV (about 10^{-4} on the horizontal scale). It is clear in this graph that this energy is below the point of minimum ionization and can result in saturation. This calculation was performed by GEANT.

4.1.3 Calibration of Scintillator Counters Using Radioactivity

Once the Monte Carlo results are known, they can be used to calibrate the detector. If we can reconstruct the expected energy spectrum in a scintillator counter then we can normalize it to the Monte Carlo to have an absolute calibration.

Since one to five MeV is the important signal region for the LIP search, reconstructing the low energy spectrum in this region is proof that we can also reconstruct LIPs in this region. For this reason, we require a counter to have a good calibration in order to use it for the LIP analysis.

The analysis has been restricted to horizontal counters where the low energy spectrum can be well fit. There are a few reasons why calibrating the vertical counters at low energy is more difficult then calibrating horizontal counters. First of all, the resolution is worse because with only one phototube and one mirror per side of the tank, fewer photons are collected so the photo-electron statistics are worse. Also, for the same period of data collecting, it is harder to collect enough statistics necessary for a good fit. This is due both to acceptance and the fact that there are three and not four tanks plugged into each waveform digitizer card as is the case for the horizontal scintillator counters. The importance of this latter condition will be made clearer in the following description.

Because of the requirements of monopole physics, one millisecond worth of data is collected for every counter after every event which causes a readout of the WFDs. The radioactivity pulses collected in this period make it possible to reconstruct the low energy spectrum. Figure 4.9 is an example of this for one of the horizontal counters. A provisional energy scale based upon the expected muon energy deposition was used for this histogram.

The solid line is an exponential fit to a falling radioactivity spectrum plus two gaussians. The result of the calibration procedure is the ratio of the provisional energy assignment to the energy loss determined by the Monte Carlo calculation. In the example given the second gaussian has a peak at the provisional energy of

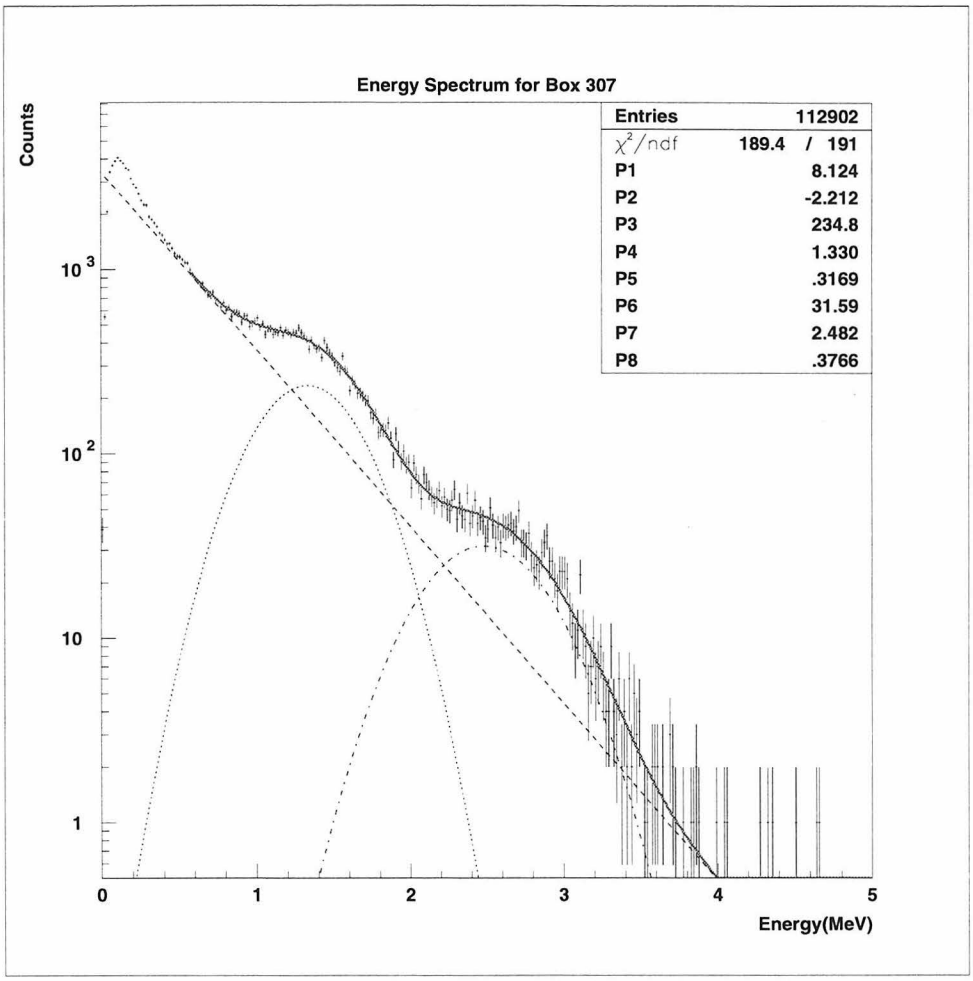

Figure 4.9: A fit to low energy WFD data with a falling radioactive spectrum, and a Gaussian associated with both the 2.6 MeV γ(Tl) and 1.4 MeV γ(K) line. Each energy bin is 16.7 keV wide. The eight parameters of the fit are the normalization and slope for an exponential and the normalization, mean, and width for the two Gaussians. This figure should be compared with figure 4.6 (the Monte Carlo calculation for a MACRO scintillator counter).

2.5 MeV. Based on the results of the Monte Carlo, the true location of the gaussian (after taking into account saturation and smearing) is 2.2 MeV. Thus all provisional energies for the tank are corrected to true values by multiplying by the calibration constant 2.2/2.5 .

The details of how the energy spectrum is constructed are as follows:

- As was described earlier in section 3.2, each WFD channel has four inputs. For each WFD channel that has only one input with a corresponding high energy muon (ERP) trigger, the one millisecond of radioactivity data in the other three inputs are examined.

  By only looking at data from tanks that have no muons passing through them, there is no danger that the after-pulsing and late light that can happen for some time after a large PMT pulse will distort the energy spectrum. The ERP trigger is used instead of the LIP trigger because the acceptance of this trigger is higher so more calibration data is collected for each run.

  In each of these channels the data from each side of the tanks are examined individually. Any isolated pulses in a window of $\pm$ 150 ns are retained for analysis. The purpose of this is to avoid ambiguities when the peaks on the two ends of the tanks are matched together and reconstructed.

- Next, the data from the two sides of the tank are scanned for pulses which may have come from the same physical source of light. If the two sides of a tank have a pulse within 140 ns of each other, then those two pulses are integrated and corrected for their tank position as reconstructed by the neural network technique described in section 4.2.

- The average of the two sides weighted by photo-electron statistics is entered into a histogram for that scintillator counter. This histogram is fit to a falling radioactive spectrum plus two gaussians in order to determine the calibration constant for that counter.

4.2 Time Reconstruction

As was previously mentioned, a unique aspect of this LIP search is the use of a fast custom WFD system rather than the more traditional technique of using ADCs and TDCs. The WFD data in an event can be used to reconstruct the position of a particle's passage through a counter. This is important for two reasons. First of all, it is necessary, when doing energy reconstructions, to correct for the light attenuation in the tank due to the mineral oil in the counter when there is no streamer tube information available. This is the case for the reconstruction of the low energy radioactivity data described in section 4.1.3.

Second, during the LIP analysis itself, an important requirement is that the position as reconstructed by the scintillator system agrees with the position inferred by the streamer tube reconstruction. This cut assures that a small radioactivity pulse which happens elsewhere in the counter, followed by a track passing through a crack in the detector cannot fool the analysis. The width of the position resolution determines how tightly this cut can be made.

Figure 4.10 is a pictorial representation of the light traveling inside a scintillator counter after a muon passes through and the resulting waveforms.

4.2.1 A Simple Software Constant Fraction Trigger

The actual position of a particle's passage through a tank can be calculated using the WFD information by:

$$\text{pos} = \frac{\Delta t \times v}{2} \tag{4.5}$$

where Δt is the difference in arrival times between the pulses on the two sides of the tank (as estimated from the waveforms), and v is the effective speed of light in the tank. In this analysis v is the same for every tank. It is taken from the empirical measurement of light travel time in one tank ($18.50\ cm/ns$). If the value of v is systematically too high or too low, the value reconstructed for position should be

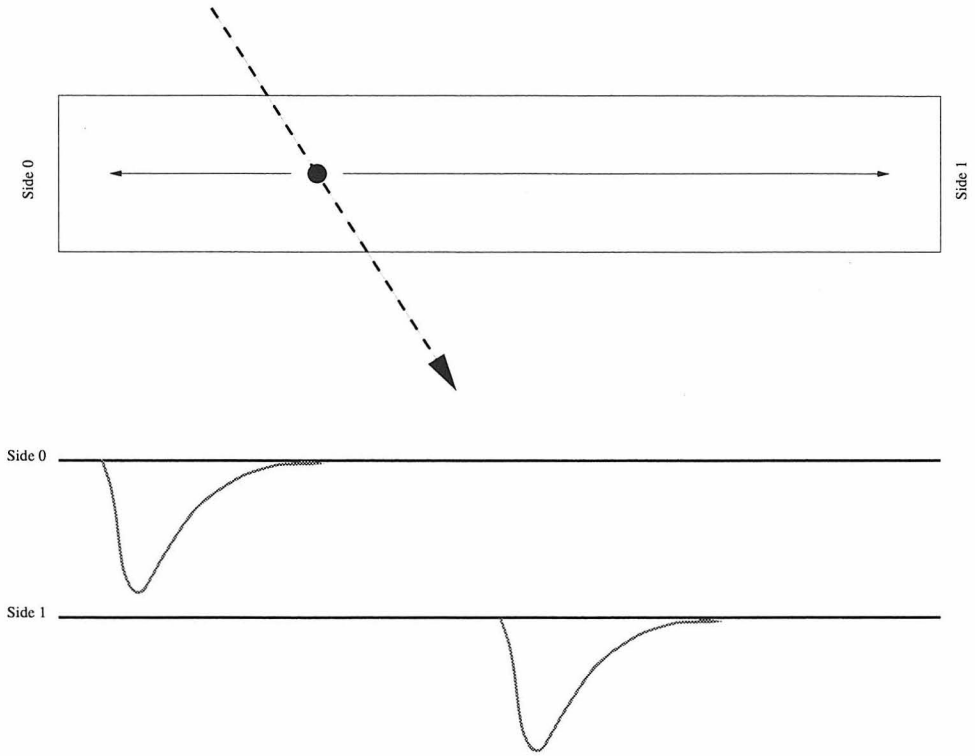

Figure 4.10: When a muon passes through a counter, the produced light has to travel a different distance to the two sides of the counter. Because of this the waveform on one side of the counter will see the pulse first. The position of the light production inside the counter can be estimated from the difference in time between these two pulses if the speed of light in the counter is known.

compensated for this fact by the neural network technique described in section 4.2.

In order to calculate this time difference, a software emulation of a constant fraction trigger [17] is used. This circuit triggers at the point on the leading edge of a pulse which is a fixed fraction of the maximum height of the pulse. However, because the pulse is sampled every 5 ns instead of continuously, the actual maximum isn't known. Instead, the maximum digitized sample (lowest voltage since the pulses are negative) is used as an estimate.

In order to estimate at what time the pulse crosses the fixed fraction of the maximum peak voltage (20% is used for this analysis) a simple linear fit is used between the two samples closest to the point of crossing. Figure 4.11 is a pictorial representation of this.

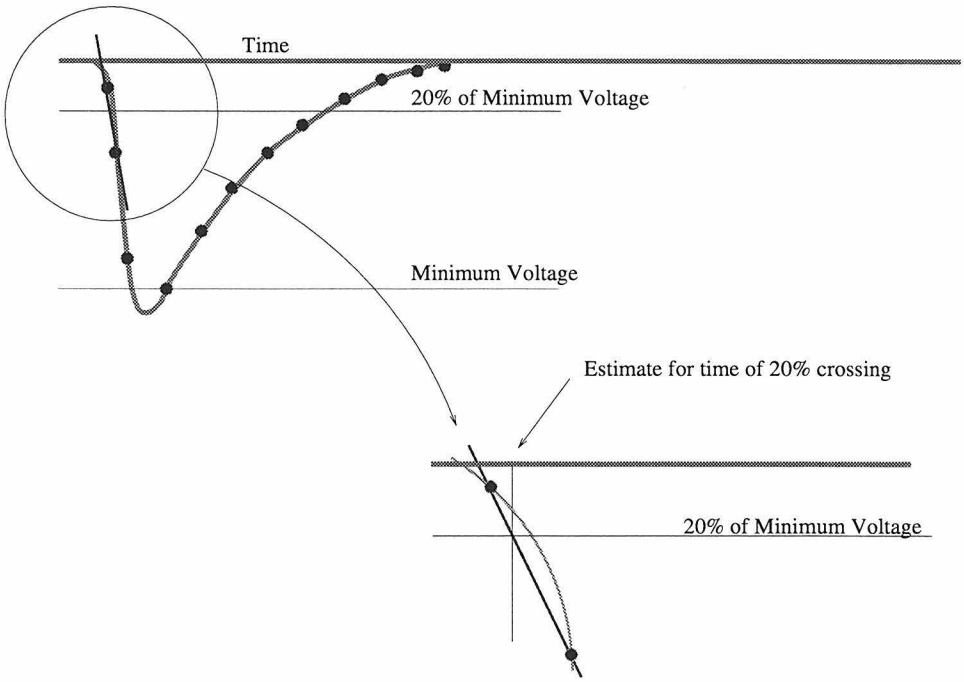

Figure 4.11: A simple software simulation of a constant fraction trigger. First the lowest digitized point is used as an estimate of the peak voltage of the pulse. Then, to estimate where the pulse crosses 20% of this value, a straight line fit is performed between the two samples straddling the point. The intersection of this line with the 20% point determines the guess for the crossing point.

This simple linear fit and application of equation 4.5 gives a result comparable to

our traditional TDC system (at least for muon size pulses). In order to get better resolution and, even more importantly, handle the differences due to the fact that the pulse shape changes as a function of pulse height, a neural network technique was used.

4.2.2 The Neural Network Correction

The linear fit already described was used to make an initial estimate for the position in the tank. Then, a neural network was used to make a correction to this estimate. The final position used is the estimate plus the neural network's generated correction.

In order make a better estimate of the position in the tank than that produced by the simple fit described above requires fitting the leading edge of the pulses more carefully. Unfortunately, the shape of the pulse which comes from the phototube is a function of its magnitude. Finding a general shape function which can fit all pulses as a function of magnitude and position in the tank is a very difficult task. In addition, it is quite computationally intensive. For every event there are at least three tanks, each with two sides, each of which has a photo-tube pulse to be fit.

An alternative approach is to use a neural network. By training a neural network to improve the estimate obtained with the simple constant fraction trigger fit, the difficult task of fitting the shape of every pulse can be avoided. Appendix A gives an introduction to neural networks works and how they are trained for the reader not familiar with the subject.

Figure 4.12 is a representation of the network used in this analysis. The network is trained by using the positions in the tanks as reconstructed by the streamer tube system. There is one hidden layer made of sigmoid neurons and one linear output neuron. This relatively simple configuration works well and more complicated architectures did not perform better.

The first important thing to note is that there are a fixed number of inputs in the network. The question then becomes: what should the inputs to the network be for this problem? One simple solution is to present all waveform samples recorded in

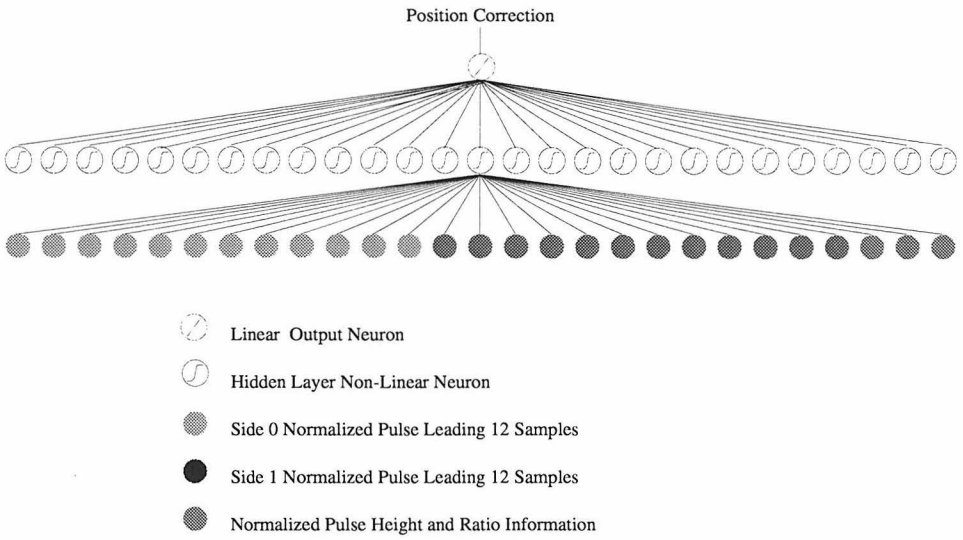

Figure 4.12: The network architecture used. There are 27 inputs, 27 sigmoid neurons in a hidden layer, and one linear output which gives the correction to the initial simple constant fraction trigger guess for the position. Note: All neurons are fully connected; for clarity of the figure however, only two of the neurons have their connections shown.

an event to the network. This is clearly not a good idea for several reasons. First of all, the number of waveform samples differs from event to event and from channel to channel. Secondly, most of the waveform data are not useful for doing the calculation we want.

Instead, what is done is to present only the first 12 samples from each pulse on either side of the tank to the network. The initial estimate from the linear fit is used to determine where the pulse starts and to select the 12 samples to present to the network.

In general, any work that the user can do for the network is something it need not be trained to do later. By reducing the number of tasks that the network must perform in order to reach the desired answer, the complexity of the network architecture and the training time can be reduced. For this reason, it is common to pre-process the data in some way before passing it to the network.

In our case, the digitized waveform samples are normalized to the maximum pulse height so that the network always sees the same size of pulse (i.e., the pulses are

normalized so that the peak sample has a height of one). This is done independently for each side of the tank so that the network does not need to scale the pulses to compare them to each other.

There is, however, information in the relative pulse heights between the two sides of each tank. The attenuation of the light in the scintillator counters maps the ratio of the heights between the two sides of the tanks to a position along the tank. In order to tell the network about this information, three additional inputs are used. Two inputs contain a scaled version of the original heights of each pulse and the third contains their ratio.

To train the network we use positions reconstructed with the streamer tube system. This requires no Monte Carlo and the data are continuously available. Since this data is always available, it is also possible to continuously determine whether the values which have been chosen for the weights of the network are still valid by comparing the positions reconstructed in the tank by the waveforms and the streamer tubes as a function of time.

If the constant time offsets (due to cable length delays or photo-electron propagation time, *etc*) are removed for each channel, then one single network works for every tank in MACRO. There are two advantages of having only one network. First, it eliminates the need to keep a database with many constants for each tank. Second, if every tank can be used, it only takes a short amount of time to amass enough data for training the network. One standard MACRO run produces enough data. The cost of having only one network is that the resolution is not as good as it might be if one had a network trained for each tank. However, for our purposes the advantages outweigh this cost.

Figure 4.13 shows the difference in position of a muon which passed through a scintillator tank, as calculated from the streamer tube and the WFD after correction by the neural network. Since the position resolution of the streamer tube system is a centimeter or less, the error here is mostly due to reconstructing the scintillator information. The sigma of the fit is about 8.5 cm, when data for all tanks used in the analysis are combined. Individual tanks typically have a smaller sigma. Figure 4.14

is the same distribution for a randomly chosen tank in MACRO, with a sigma of 6.5 cm.

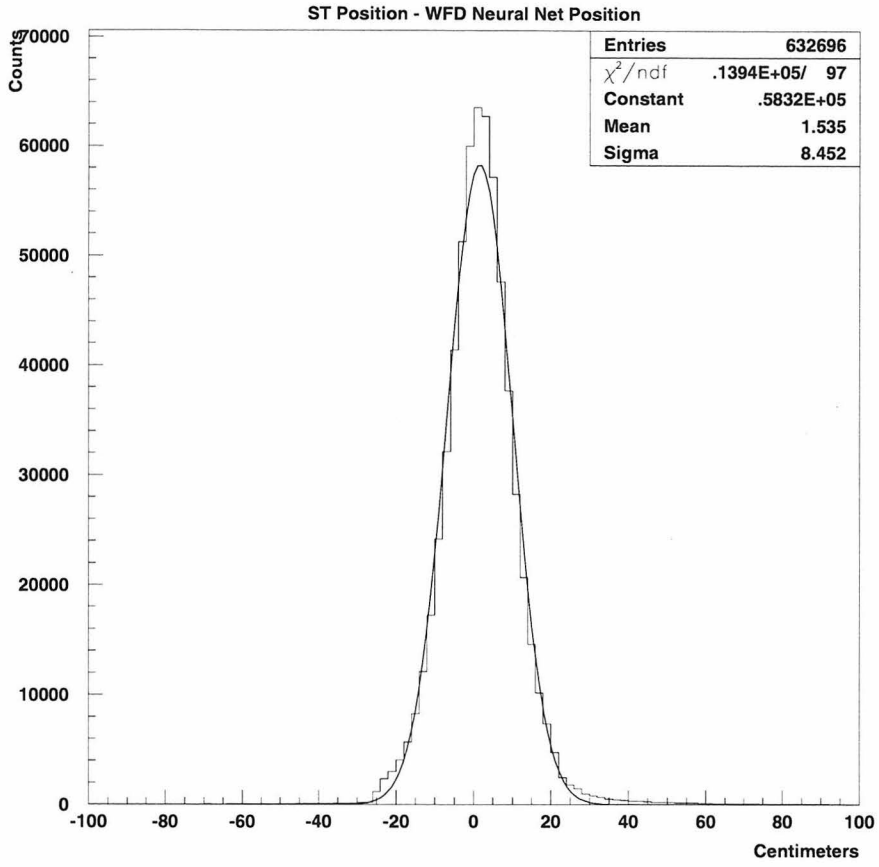

Figure 4.13: Neural network corrected WFD time position - ST position. The sigma is 8.5 cm. This histogram is for *all* good tanks in MACRO used in the analysis. Individual tanks have smaller sigmas.

Figure 4.13 contains entries over the entire range of energy deposition. It is dominated by muons with path-lengths of 19 cm or more. Because of this, most of the entries come from energy depositions on the order of 40 MeV. It is also important to investigate how well the procedure works for lower energies, specifically in the signal region of 1-5 MeV. We can investigate this by choosing particles which leave small amounts of energy in the tanks. This happens often because sometimes the path

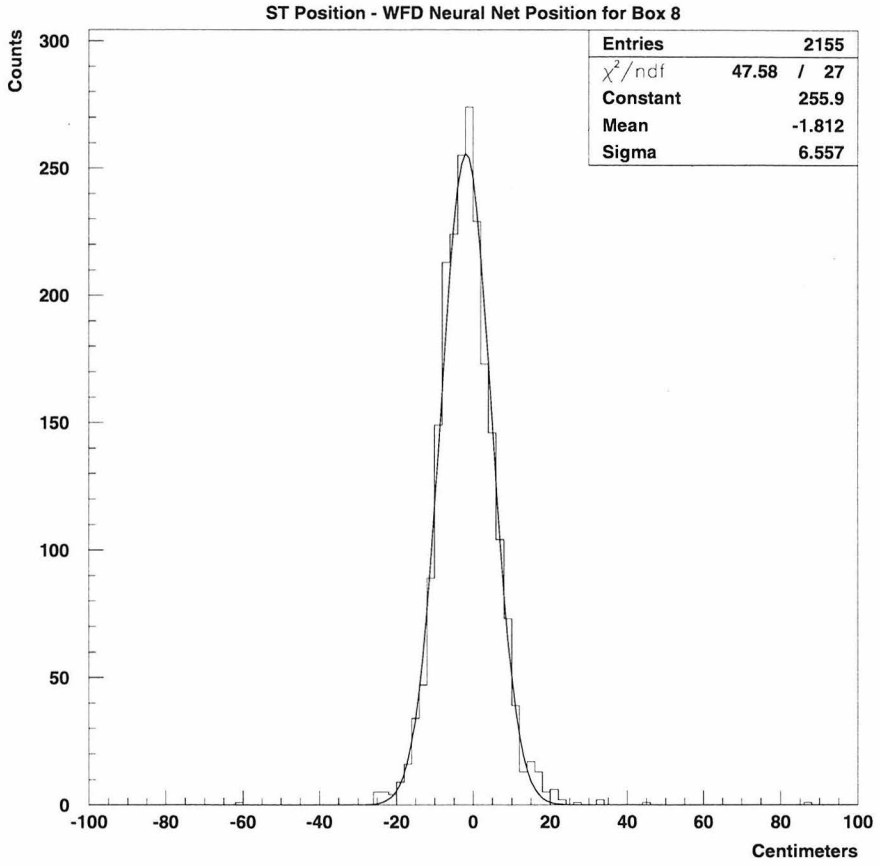

Figure 4.14: Neural network corrected WFD time position - ST position for one tank in MACRO. The sigma is about 6.5 cm. This width is 25% less than the width for the distribution made with all tanks.

length though a scintillator box can be very small.

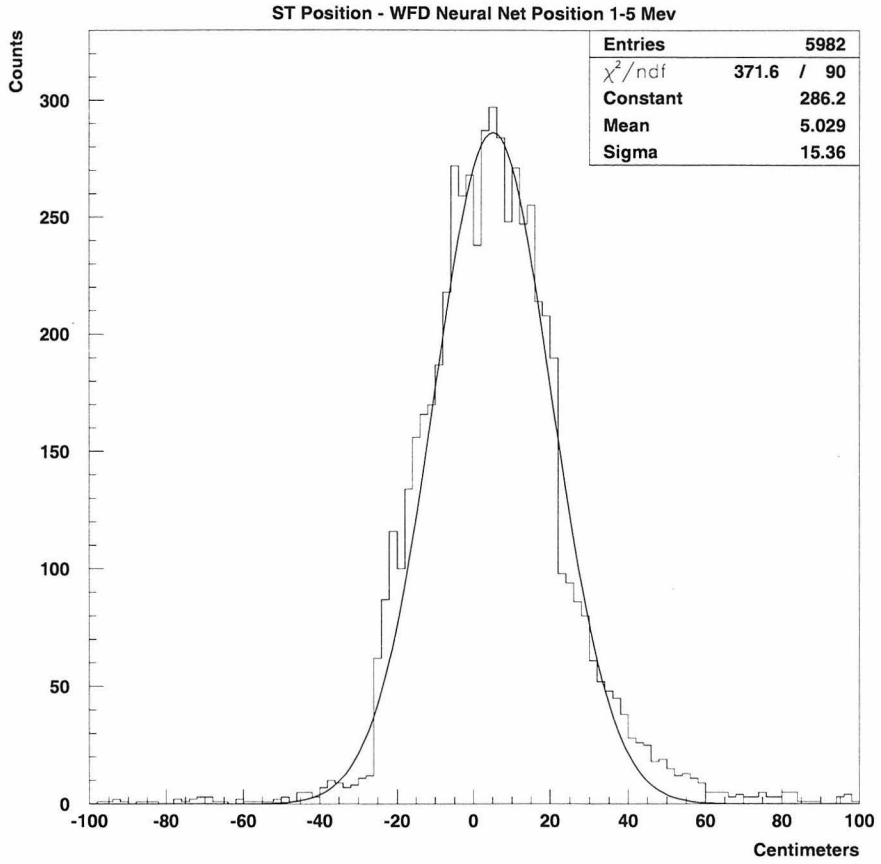

Figure 4.15: Neural network corrected WFD time position - ST position for cases where the energy deposited is between 1 and 5 MeV. The sigma is about 15 cm. This histogram is for *all* good tanks in MACRO used in the analysis.

Figure 4.15 is the same as figure 4.13 except that only boxes with energies from 1-5 MeV have been used. In this histogram, the sigma is slightly less than twice that of the previous histogram. This determines the value of the cut which can be used in the data analysis for comparing the streamer tube and scintillator reconstructed positions. In this analysis the value of the cut is $\pm 45\ cm$. The resolution of the low energy events is lower because photo-electron statistics cause fluctuations in pulse height at low energy and there is more training data at higher energies.

One can also take the root mean square (RMS) of the resolution distribution. Although especially sensitive to non-gaussian tails, the RMS is nonetheless useful to look at it as a function of energy. Figure 4.16 shows the RMS of the resolution distribution as a function of energy for both the waveforms and the ERP. This figure shows that the neural net correction performs better than the traditional TDC method across all energies and is particularly better at very low energies.

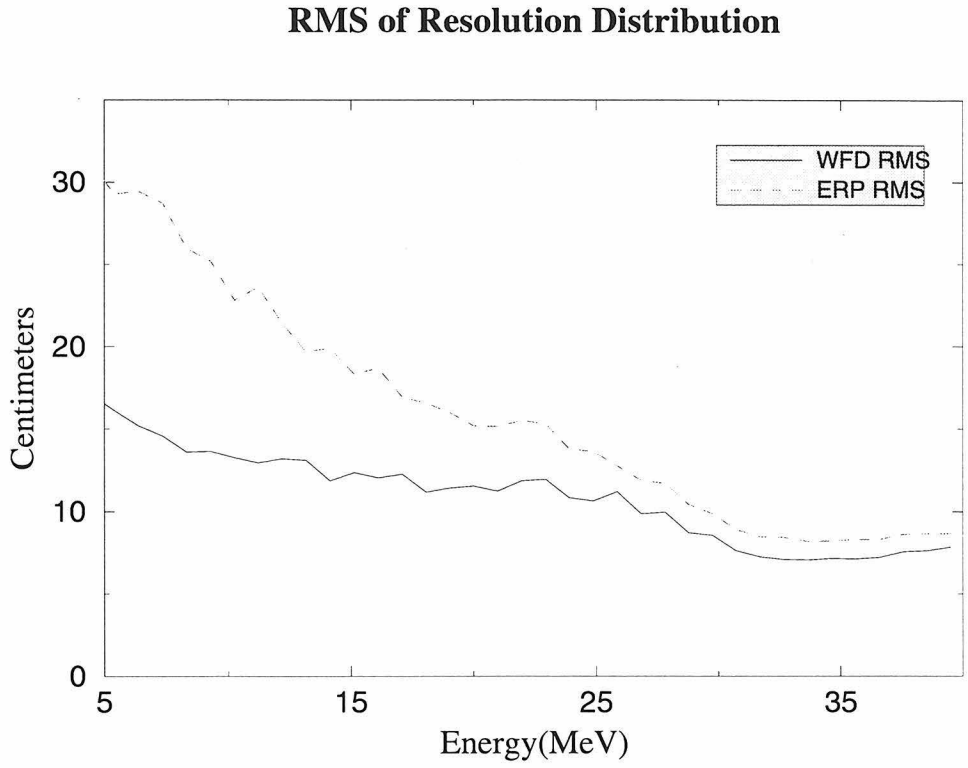

Figure 4.16: The RMS for the resolution distribution as a function of energy. The data is shown both for the neural network corrected WFD and for the TDC system of the ERP. The RMS is not as good a measure as a fit to the gaussian since the RMS is affected by tails of the distribution. Nonetheless, it is clear that the neural network correction performs better than the traditional TDC procedure across all energies.

Chapter 5 The LIP Search

Once the energy and time calibrations are complete it is a relatively simple procedure to look for LIPs in the data.

5.1 Data Sets

The data for this search come from two periods. The first ran from July 24 to October 12 of 1995. The second period ran from December 17 1995, to November 16 1996. These were both periods of uninterrupted waveform and LIP operation with the entire MACRO detector.

The first two month period was the initial commissioning for the waveform system. The time between the first and second period was used to install new hardware, fix broken waveform channels, and reset the photo-multiplier tube gains. The live-times for the complete data set are presented in section 5.3.

Also, for most of the first period of running, the inter-SM LIP trigger was not yet working properly and so the cables between the LIP modules in each supermodule were unplugged.

5.2 Data Reconstruction

Before searching through the data for LIP candidates, the raw data was reduced into a form more acceptable for data analysis. In order to reduce the data set size down from an initial size of approximately 500 Gigabytes, only information relevant to the LIP analysis was retained. Only events with LIP or fast streamer tube triggers were kept and the energy and timing information for a scintillator counter was only reconstructed and saved if a streamer tube track intersected with it. The events with only a streamer tube trigger are kept for efficiency studies.

In order to reduce backgrounds, we require that a streamer tube track pass though each counter that we examine, and that the positions as reconstructed by the WFD algorithms and the streamer tubes agree. This reduces the chances that the energy we are examining is actually from a pulse of coincident but random radioactivity. Because of this, the data set can be broken into two exclusive pieces: a single track and a multiple track set. The next section discusses how these data sets are constructed.

5.2.1 Tracking Requirements

In any given event where the LIP trigger is present, there can be zero or more tracks in the wire, strip, and lateral views. The lateral view is constructed from streamer tube hits in the vertical streamer chambers and also uses the hits in the wires and strips. For single tracks which pass through the vertical walls of MACRO the combination of this view with the wire view often does a better job of track reconstruction than the combination of wire and strip views since the addition of the vertical streamer planes adds more information.

In some cases one single unambiguous three-dimensional track in space can be reconstructed, and in other cases there are ambiguities which must be resolved.

Single Track Events

Approximately 90% of the events that have streamer tube tracks associated with the trigger are single track events. In this case there is one and only one track in the wire view and a track in either or both of the strip or lateral views. If only a wire track and a strip track exist, they are combined together to make a three-dimensional space track. If a lateral track also exists, it (not the strip track) is combined with the wire track to make the space track.

Multiple Track Events

It may be the case that there is more than one track in either the wire or strip views. For multiple track events the lateral view is ignored in this analysis. This situation

is more complicated than the case presented before, because there is more than one way to combine the tracks from the wire and strip views into three-dimensional space tracks. Although it is true that not all combinations of wire and strip tracks result in physically possible tracks (i.e., tracks that fall inside the detector), there are many possibilities which are ambiguous. In order to determine which wire tracks should be combined with which strip tracks, information from the scintillator is used to check the consistency of all the possible streamer tube tracks with the scintillator information.

The procedure used to resolve the ambiguities is as follows:

1. Combine all possible wire and strip tracks into three-dimensional space tracks.

2. Keep those possibilities where space tracks pass through three scintillator faces. By requiring only tracks that pass through three faces, we reduce the chances that a non-physical space track agrees with the scintillator positions in all of the volumes that we check.

    - For each of these tracks, reconstruct the position in scintillator volumes that the tracks pass through.
    - Keep only those cases where the scintillator and streamer tube positions agree. This should retain only physical space tracks.

3. Reject multiple tracks passing through the same scintillator counter. In order to recognize a LIP, it must pass without any other particles through each scintillator volume, because it is difficult to distinguish a single muon from a muon and LIP summed together.

4. Resulting tracks are analyzed to determine whether their energy loss is consistent with that of being a LIP. These are referred to as *analyzable tracks.*

Unfortunately, the efficiency of this algorithm for isolating tracks in high multiplicity bundles is not high. This is due mostly to the fact the the WFDs have a four-to-one fan-in. In a muon shower with many tracks, there is a significant chance

that more than one particle will pass through counters attached to the same WFD channel. In this case, since the particles arrive at approximately the same time, the resulting wave form is a superposition of more then one PMT pulse and the WFD reconstruction algorithms do not work properly. This is less of a problem on the outside edges of a shower where the particle density is not as high. Therefore, the algorithm works best outside the core.

Figure 5.1 shows the wire multiplicity distribution for this data set, and figure 5.2 shows the multiplicity distribution of the number of analyzable tracks found in the events in the data sample. To see the correlations in these two distributions, figure 5.3 shows for this data set the number of analyzable tracks that were found in the event as a function of the multiplicity as measured by looking in the wire view. In this data set the highest wire multiplicity observed was 19 while the largest number of analyzable tracks found in an event was 7. In that event, 7 of the 11 tracks were able to be unambiguously reconstructed.

In order to understand how well the algorithm performs as a function of distance to the core of the shower, an estimate of the shower's core position is made by averaging the X position at the half-height of MACRO for all of the wire tracks, and averaging the D position at the half-height of MACRO of all of the strip tracks. The D position in the detector can be converted into a Y position by the following simple geometric transformation [40]:

$$Y = \frac{-\sin(\beta - \alpha)X + D}{\cos(\beta - \alpha)}, \tag{5.1}$$

where

$$\begin{aligned} \beta &= 101.912 \times \frac{\pi}{180^\circ} \\ \alpha &= 38.412 \times \frac{\pi}{180^\circ}. \end{aligned} \tag{5.2}$$

Once the position of the core of the shower is estimated, the shortest distance to the core can be calculated for each analyzable track. This distance is the line

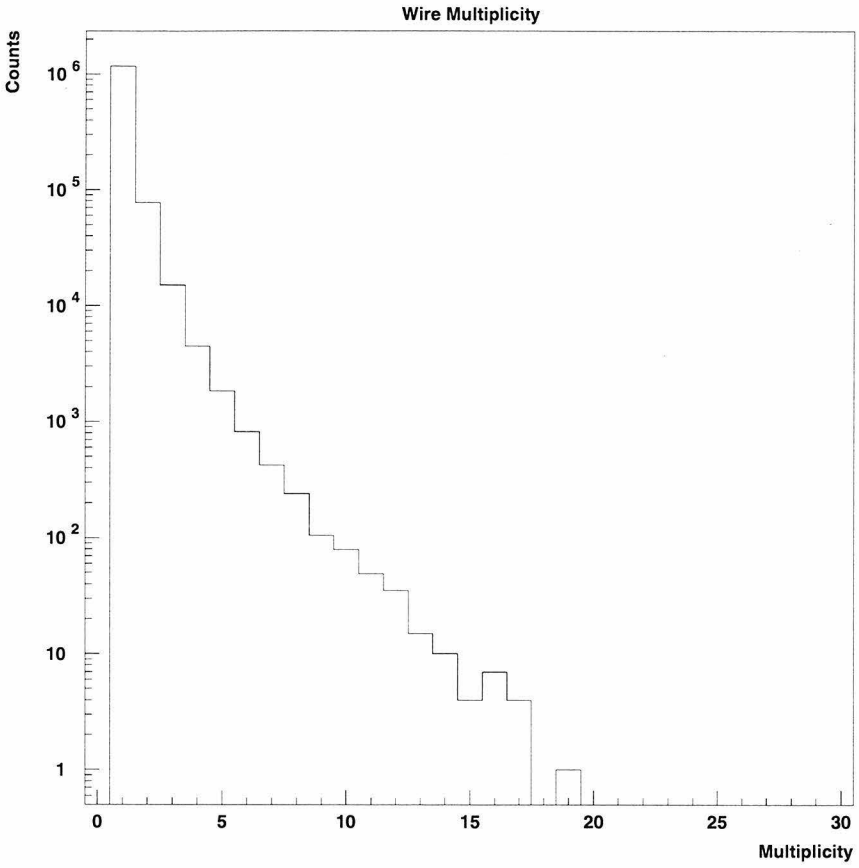

Figure 5.1: Track multiplicity measured in the wire view.

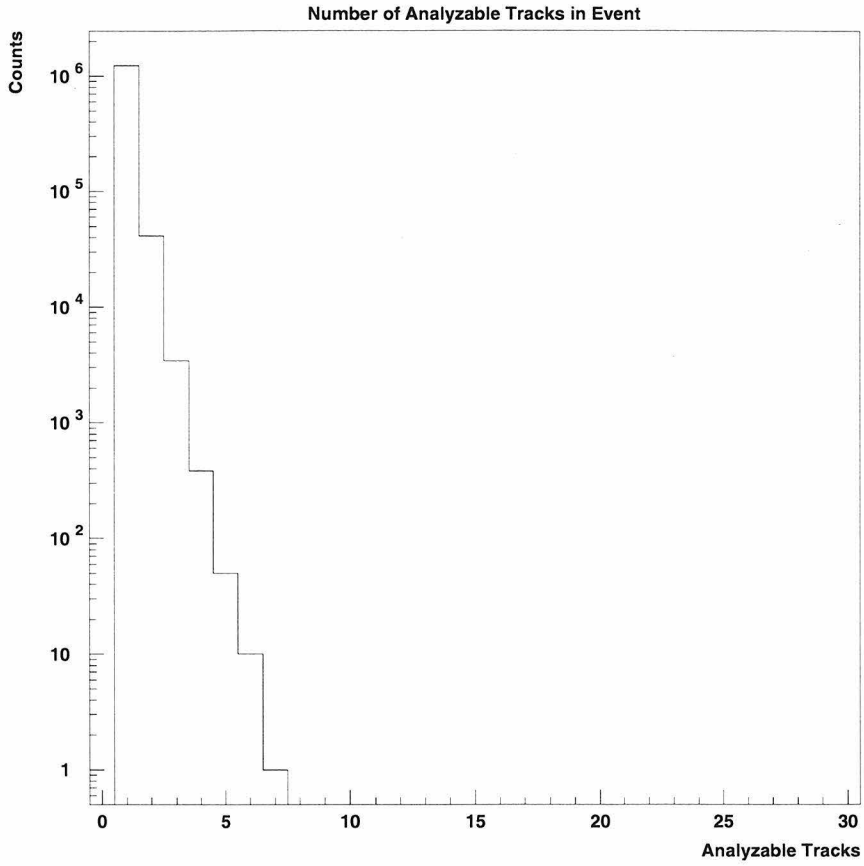

Figure 5.2: The distribution of the number of analyzable tracks in each event.

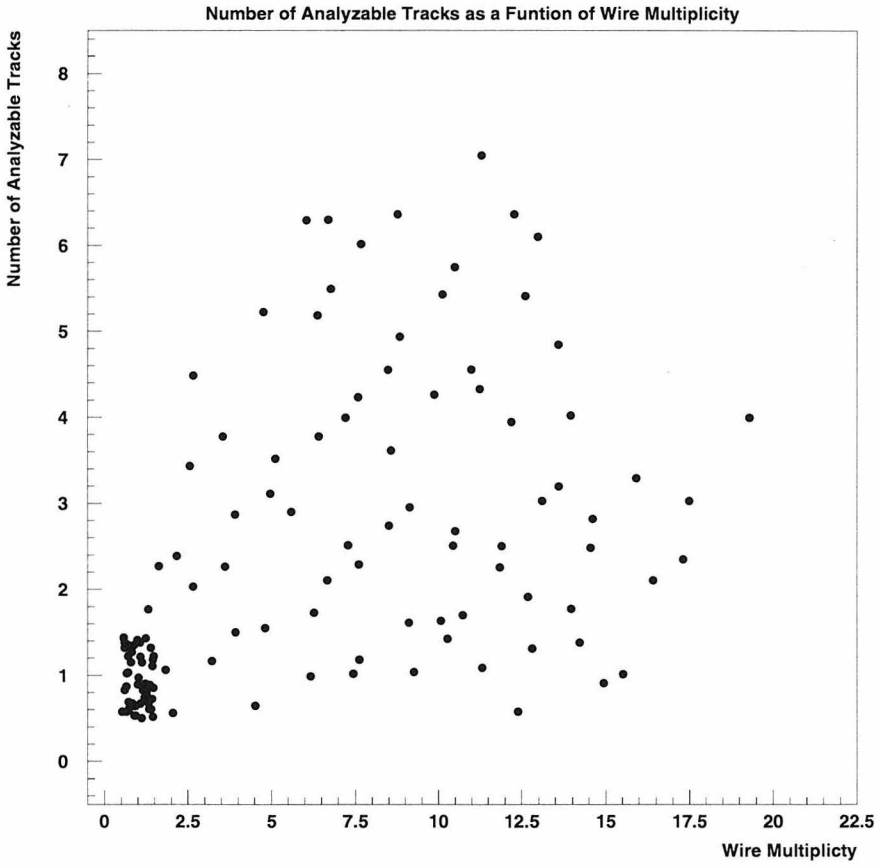

Figure 5.3: The number of analyzable tracks as a function of multiplicity measured in the wire view.

perpendicular to the track which intersects the three-dimensional point at the core.

Figure 5.4 shows the number of events as a function of distance from the core and multiplicity. A double muon event with one muon that passes through one end of MACRO and another muon which passed though the other end of MACRO would have two entries in this histogram (one for each track) and the distance for each from the core would be about 35 m (half the length of MACRO).

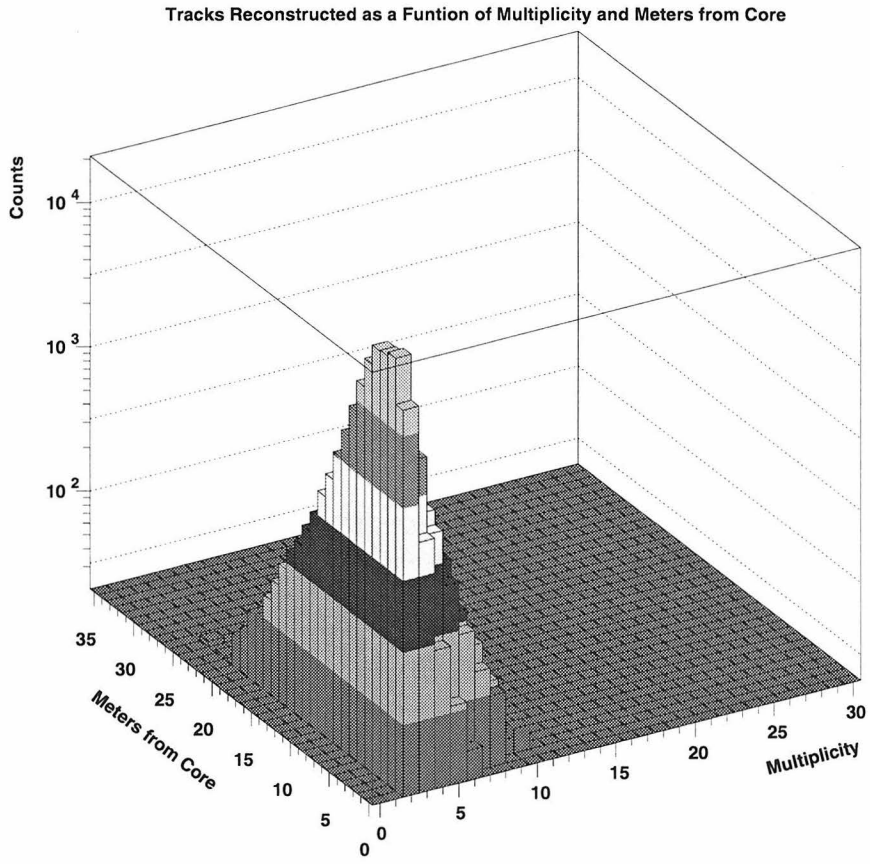

Figure 5.4: The number of analyzable tracks as a function of multiplicity and distance from the shower core.

If one once again takes the wire multiplicity as an estimate for the multiplicity of the event, it is possible to estimate the efficiency for the track matching algorithm as a function of multiplicity. Figure 5.5 shows the fraction of tracks which were

successfully analyzed as a function of the multiplicity of the event.

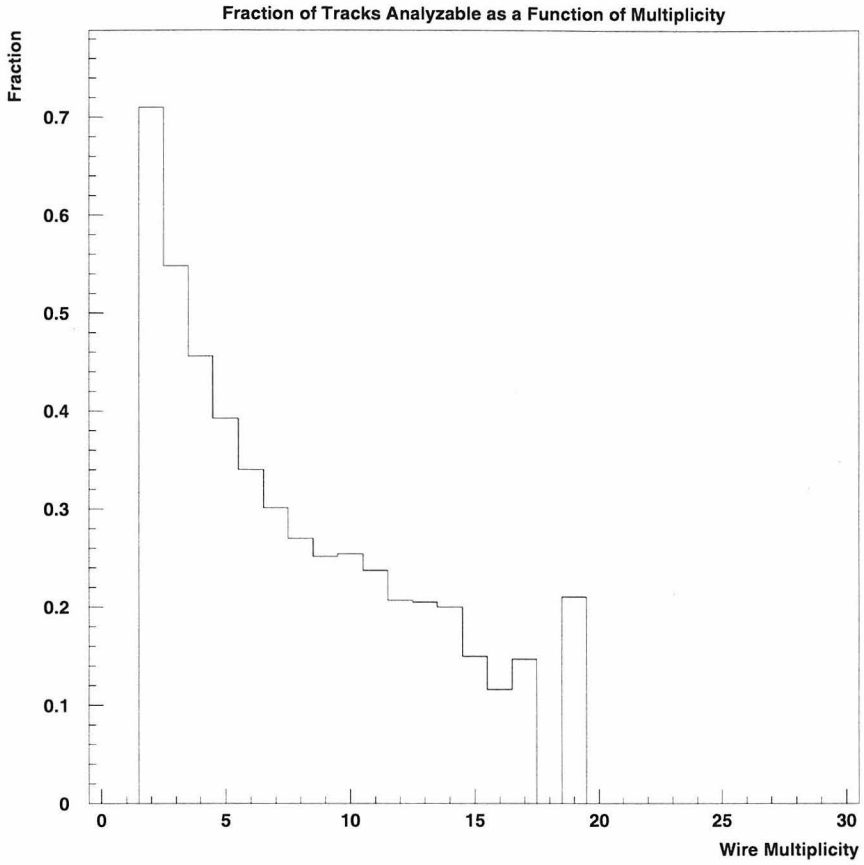

Figure 5.5: The fraction of tracks which are analyzable as a function of multiplicity. For any given multiplicity the fraction is the total number of tracks analyzed for events with that wire multiplicity divided by the number of tracks at that wire multiplicity.

5.3 Event Selection

The following conditions must be met for an event to be considered in the LIP analysis:

1. The event must contain at least one analyzable space track. The requirements to construct an analyzable space track are described in section 5.2.1.

2. The LIP trigger must have fired.

3. There have been no CAMAC errors. Such an error indicates that some piece of hardware was not working properly.

4. The stop master must have been working properly. If the stop master does not work properly during an event, the waveform data will not correspond to the time the trigger happened. This could result in accidently integrating small radioactive pulses.

5. All three faces (top, center, and bottom) must have been hit by the track. The requirement that the track does not pass through the vertical walls (necessary for calibration reasons described in section 4.1.3) reduces the acceptance by about a factor of two for an isotropic flux. The track also must have gone through counters which have had their energies reconstructed without any errors. There are a few reasons a counter might not have a good reconstruction:

   - The counter might not have good calibration constants for some time period.
   - The box may have been dead for some period of time (either because its supermodule was not operational or because of maintenance).

Data from the time period described in section 5.1 were examined. Table 5.1 shows how many events met each of the above requirements.

Requirement	Number of events which satisfied requirement
Good Track	5,356,651
LIP trigger present	3,259,886
No CAMAC error	3,259,183
STOP Master functioning properly	3,041,755
Three good horizontal tanks hit	1,276,590

Table 5.1: The number of events which met the event selection requirements.

5.4 Live Times

For each track there are two ways the LIP trigger can fire. If the track is completely contained inside one supermodule, then the LIP trigger for that supermodule will fire independently. For most of the first period of running this was the only way a LIP trigger could be formed.

In the second period of running the inter-supermodule LIP trigger was fully enabled. This enhancement allows particles passing from one supermodule to another to also cause a LIP trigger to be formed. In this case the LIP module in each of the two supermodules that the particle passes through forms a trigger. The details of how the inter-supermodule LIP trigger works are explained in Appendix B.

The acceptances (see chapter 7) and live times are calculated for the single supermodule and inter-supermodule case independently, to account for times when only a subset of the supermodules are active. In order to determine exactly when different parts of the detector are operational for this search, the live time for each supermodule and inter-supermodule pair is calculated by subtracting the times of the first and last track which meet all the requirements of Table 5.1 for that particular piece of apparatus. Table 5.2 shows the calculated live times for each supermodule and inter-supermodule pair. Since the average time between events is less than one percent of the average run time, this is a good approximation of the actual live time.

5.5 Analysis Cuts

Each of the events that meet the event selection criteria must then be checked to determine whether they are consistent with being a LIP. For each box the reconstructed energy is scaled to a 19 cm path length, the signature of a LIP being that all of the boxes on a track exhibit energy deposition per unit length significantly less than that of of muon.

The expected signals from LIPs will be discussed more fully in Chapter 6. Roughly, the trigger becomes efficient at about 1.2 MeV and quickly rises to 100% efficiency.

SM	Live Time
1	229.3 days
2	235.8 days
3	221.9 days
4	183.7 days
5	249.7 days
6	240.6 days
1/2	177.6 days
2/3	175.1 days
3/4	58.4 days
4/5	127.2 days
5/6	185.2 days

Table 5.2: The calculated live time for each supermodule and inter-supermodule pair. The live time is the subtracted time of the first and last track in each supermodule or pair which meets the event selection criteria. The average time between events that pass the cuts in a supermodule is about 1 minute and runs are typically 6 hours long.

Then, at about 20 MeV, the efficiency quickly drops to zero because a cut must be made to reject muons.

At least three boxes are hit by each track, and there are several ways to ask whether the energy deposition in these boxes is consistent with a LIP. The technique used here is to pick one number which characterizes the energy loss for all the tanks on that track. Perhaps the most obvious choice is the average of the reconstructed energies of these boxes. The problem with this approach is that the average energy loss can be low if only one box has a low energy, which can result from tracking errors.

Another measure, the one used here, is the maximum energy in **any** box on the track. Thus only in the case where **all** of the boxes are anomalously low will a low event energy be returned. Figure 5.6 is a histogram of this distribution for all of the tracks that pass the selection criteria.

Before any cuts, there are events in the region where LIPs would be expected to appear ($\lesssim$ 20 MeV). These result from two classes of reconstruction errors. First, there are cases where tracks passed close to the edge of a scintillator counter or very close to a phototube and the energy was incorrectly reconstructed. Fiducial cuts reduce the number of these events.

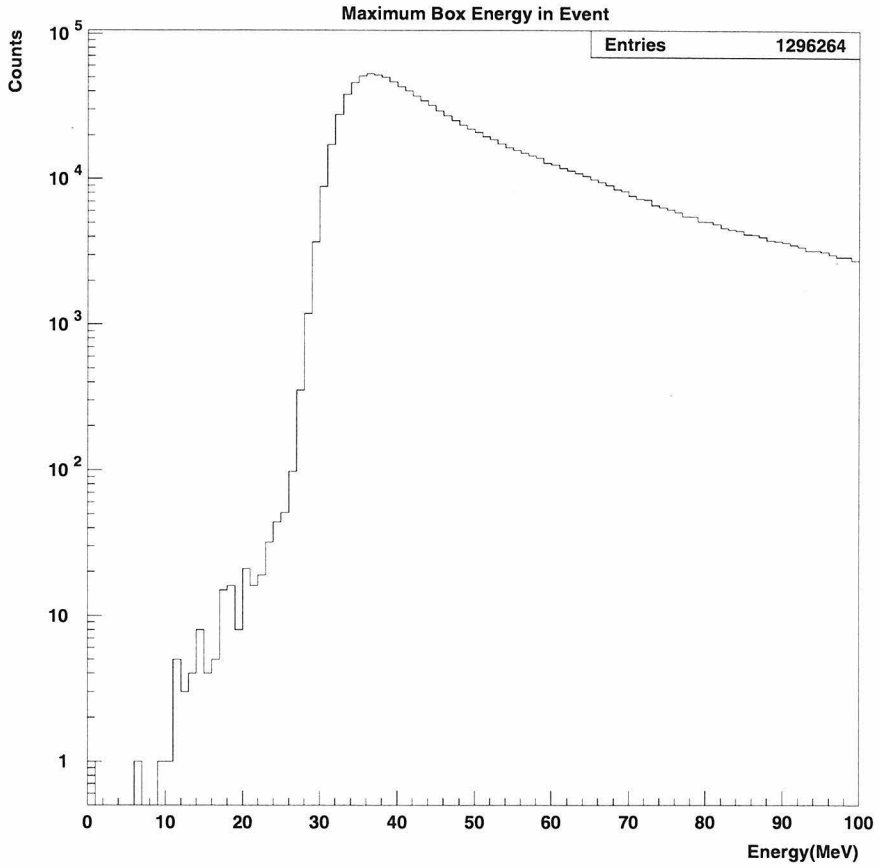

Figure 5.6: The maximum energy reconstructed for any box on the track. Only an event in which every box has a low energy will show up as having low energy in this histogram.

There are also events in which for some reason the position reconstructed by the WFDs is inconsistent with that of the tracking system. There are a few things which can cause this to happen. One is the tracking algorithm might not have worked properly for some event. It is important that the tracking algorithm work properly since we rely on the calculated path length in the box to determine the energy loss per unit centimeter.

Other possibilities include additional energy deposition in the form of electron and photon showers spread over a large area, causing the WFD reconstructions to fail; rare hardware failures in the acquisition system; and random coincident radioactivity. The last is relatively unlikely because the WFD timing algorithm chooses the largest pulse in the buffer and a muon track is required to hit the counter. So long as the passing particle deposits more energy than the radioactivity the algorithm should work properly. A cut on the agreement between the reconstructed streamer tube and WFD positions will be made to reduce the numbers of these events.

We require that the position of particle passage as reconstructed in the streamer tubes agrees with the position as reconstructed by the neural network timing procedure to within $\pm$ 45 cm. This resolution is approximately 3 σ if one uses the resolution measured in figure 4.15. This cut removes about 1.8% of the data.

Because the multiple track sample is more likely to have tracking errors, and the efficiency of the reconstruction varies as a function of the multiplicity, the single track sample is presented first. The distribution of maximum box energy for the single track sample after the position agreement cut only is shown in figure 5.7.

As was discussed earlier, it is also important to make some fiducial cuts. Because the correction for light attenuation is large at the very end of the tank (Figure 4.2) very small errors in position can lead to large errors in the energy. We therefore also exclude tracks which at their center in the scintillator volume are located in the final 10 cm of a scintillator counter.

This geometrical effect is taken into account in the acceptance Monte Carlo. By requiring that all tanks hit by the track have this fiducial requirement, the number of events in the single track sample is reduced by $\approx$ 4%.

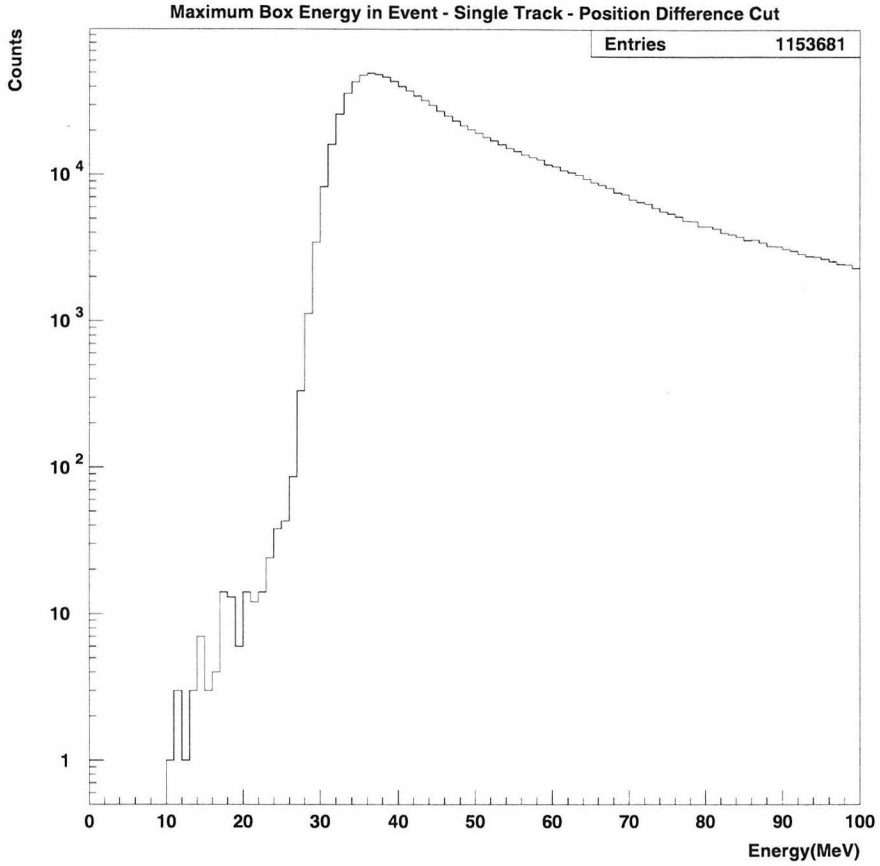

Figure 5.7: The maximum energy reconstructed in any box on the track in the event for the single track sample. In addition, the streamer tube and scintillator position reconstruction must agree to within $\pm$ 45 cm.

Tracks close to the edges of the scintillator are also sensitive to small position errors because a small mismeasurement produces a large fractional error in path length. If this situation happens in all of the boxes that the track passed through, then it is possible that an error might be made in all three faces. Also it must be stressed that a real LIP passing through this configuration would not be a believable candidate because of the above worries.

It is therefore best to remove these events from the sample and account for this in the geometrical acceptance. For this reason, any event for which **all** of the boxes on the track are hit within 2 cm of the walls of the volume (as measured from the center of the path through the counter) are rejected. This removes less than 0.4% of the data and is accounted for in the acceptance Monte Carlo. In practice this cut only removes events which are close to large gaps in the detector, because in most cases the scintillator volumes are close together, and a track passing through a small part of one counter close to its wall, will also pass through the counter next to it with a larger path length. Figure 5.8 shows the maximum energy distribution after the position difference and fiducial cuts for the single track events. The fiducial cuts remove all remaining events from the signal region.

Now the same cuts are applied to the multiple track sample. The resulting distribution is shown in figure 5.9.

There are four events in the multiple tracks sample with maximum energies between 20 and 23 MeV. The minimum entry in the distribution for the single track sample was at 23 MeV. These four events were examined by hand. All four of these events were reconstructed as double muons by the tracking algorithm. In three of the four cases, the tracking algorithm failed and assigned a track where one really did not exist. This nonexistent track intersected boxes that were actually hit, but the calculated path lengths with the fake track were incorrect. The fourth event had a maximum energy loss of 23 MeV. This event is fine and is consistent with the lowest energy seen in the single track sample.

There are no events in the data sample which have a maximum box energy less than 23 MeV. It will be shown in Chapter 6 that this is consistent with the background

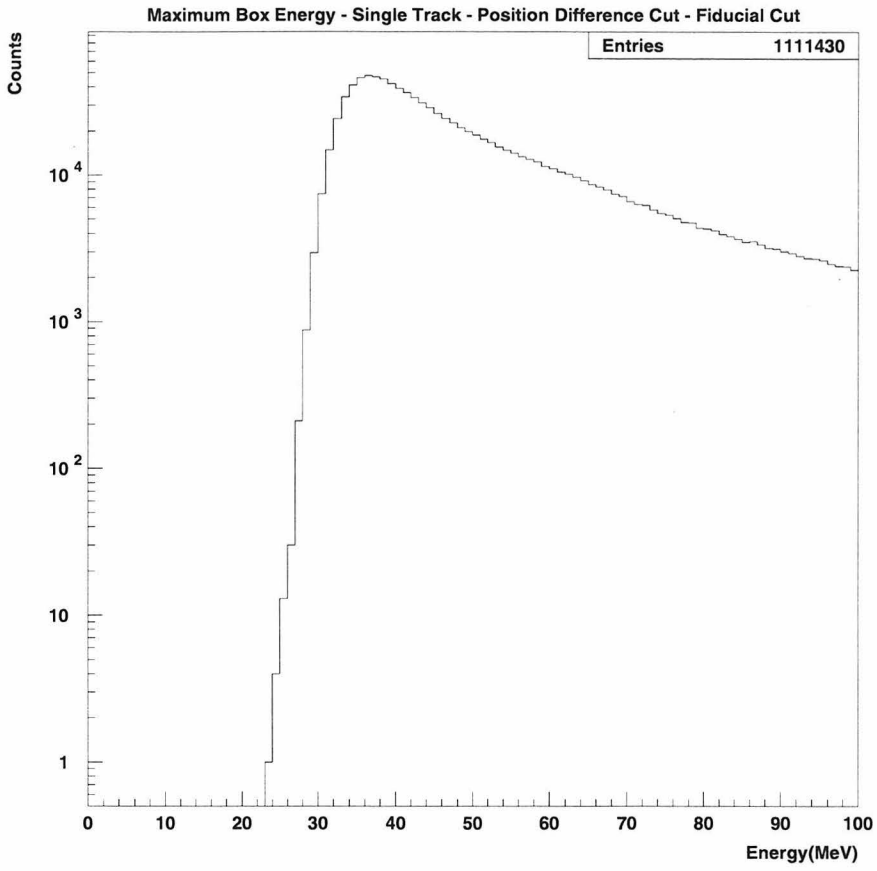

Figure 5.8: The maximum energy reconstructed in any box on the track in the event for the single track sample. The streamer tube and scintillator position reconstruction have been required to within $\pm$ 45 cm, and fiducial cuts in the scintillator volume have been been applied.

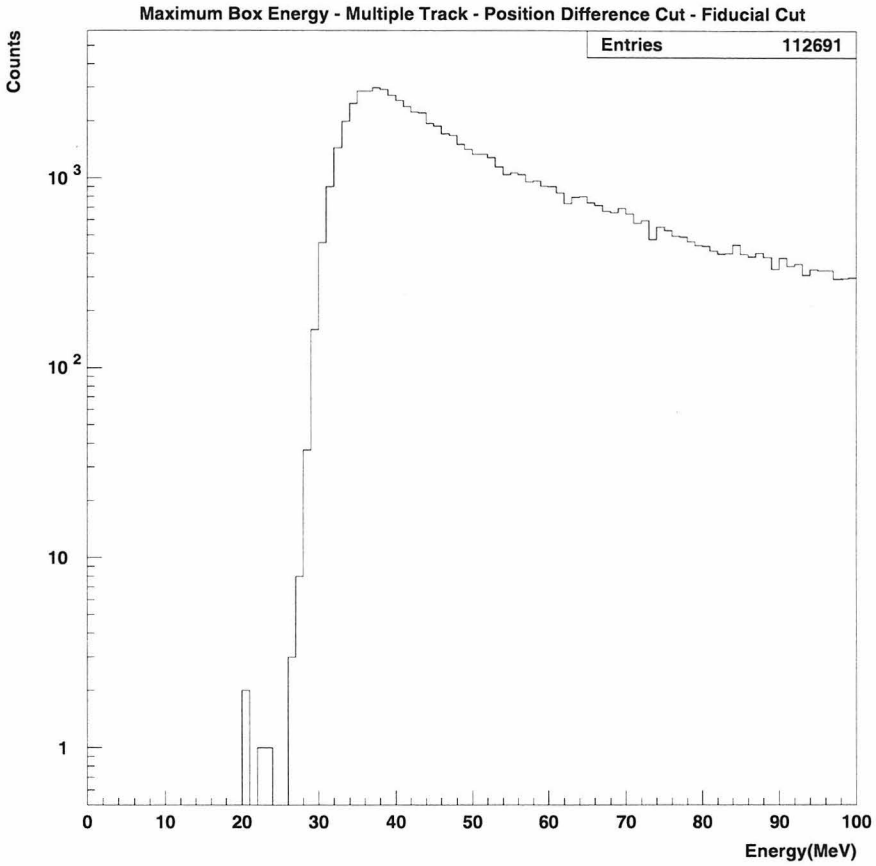

Figure 5.9: The maximum energy reconstructed in any box on the track in the event for the multiple track sample. The streamer tube and scintillator position reconstruction have been required to agree to within $\pm$ 45 cm, and fiducial cuts in the scintillator volume have been applied.

we expect from muons. Therefore, there are no candidates consistent with being a LIP in the data that was examined. When calculating the efficiency of this analysis for detecting LIPs in Chapter 6 we will consider 20 MeV the cut below which maximum box energies will be considered consistent with a LIP.

Chapter 6 Trigger and Analysis Efficiency

In this chapter we examine how efficient this search is to LIPs with different fractional charge.

6.1 PHRASE Trigger Efficiency

As was described in chapter 3, the inputs to the LIP trigger are the low energy triggers of the PHRASE circuit. Each scintillator counter of the detector has its own PHRASE circuit and they all trigger independently. Figure 6.1 is a single box spectrum taken from a free running PHRASE circuit [41].

The reason that this spectrum looks qualitatively different from the WFD counterpart in figure 4.9 is that there is no trigger threshold in the WFD spectrum. That data was taken from radioactivity in the WFD buffers and is cut off not by an energy threshold, but by the requirement that the pulses be at least a 2.5 mv high and that they be visible on both ends of the tank. In the PHRASE spectrum the ^{40}K peak is not visible because the energy threshold occurs close to the same energy as the peak.

The PHRASE spectrum is fit with a falling exponential, a gaussian centered around the $^{208}_{81}$Tl line, and a threshold function. This threshold function is a function of energy and is constructed by integrating a gaussian centered at the energy threshold, with sigma as given by the electronic resolution at that threshold, from - ∞ to the energy. This can be expressed as follows:

$$\epsilon(x) = \frac{1}{\sqrt{2\pi}} \int_{-\infty}^{x} \exp\left(-\frac{y^2}{2}\right) dy, \tag{6.1}$$

where

$$x = \frac{E - E_{threshold}}{\sigma_{resolution}}. \tag{6.2}$$

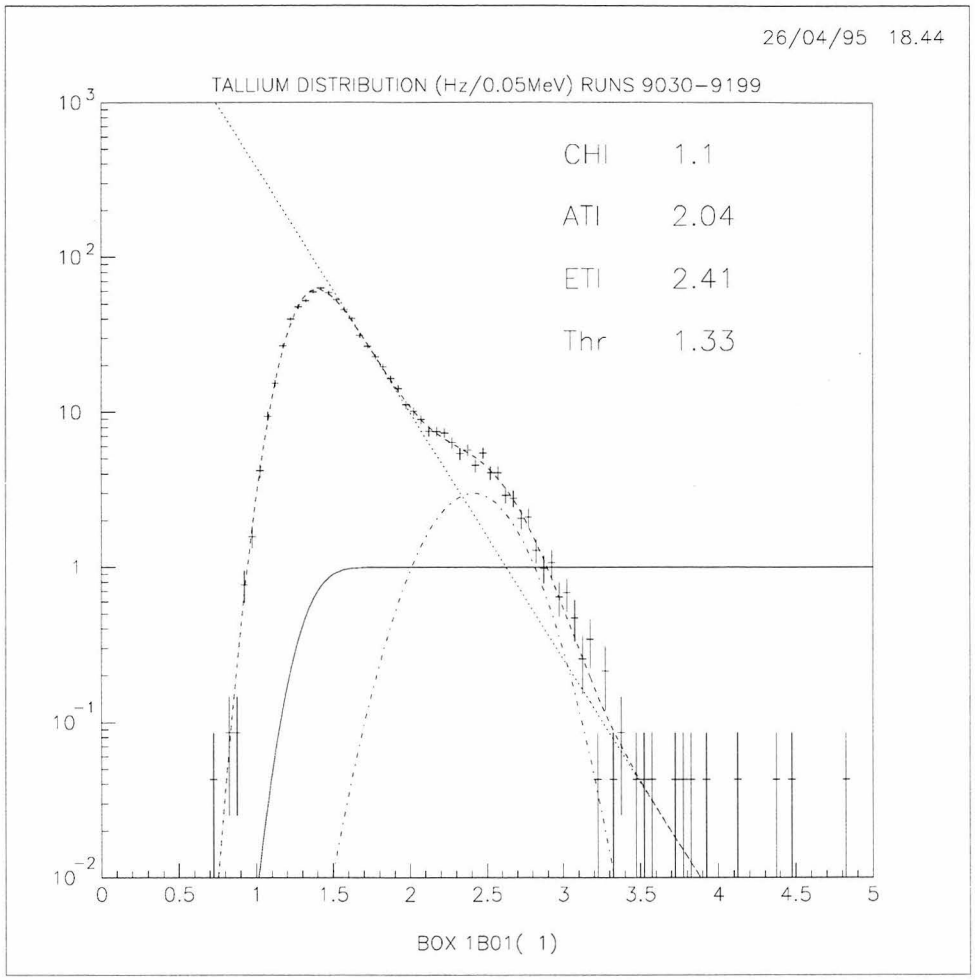

Figure 6.1: The spectrum from the PHRASE circuit of a single box. This spectrum was measured by the PHRASE circuit itself. The three lines are the result of a fit. The straight line is a falling exponential spectrum, the gaussian is centered around the thallium peak, and a threshold function is also drawn.

Equation 6.1 can be re-expressed as follows:

$$\epsilon(x) = \frac{1}{2} + \frac{1}{2}\mathrm{erf}\left(\frac{x}{\sqrt{2}}\right). \tag{6.3}$$

In figure 6.1 the threshold has been fit to 1.3 MeV. More information on the procedure for determining the thresholds of the individual PHRASE circuits can be found in [42]. Since the LIP trigger relies on the PHRASE triggers for its inputs, it is imperative to know what the trigger thresholds were during the period of the search. These thresholds will ultimately set the sensitivity of the search for particles with $\frac{1}{5}\epsilon$ charge and below.

By using muons which pass through very small amounts of scintillator ($\lesssim$ 1cm), the WFD data itself can be used to measure the threshold function of the PHRASE counters. Since there is a linear relationship between the path length of the particle through the counters and the energy deposited, by asking what the efficiency is for triggering the LIP trigger as a function of path length, we can measure the threshold function.

The strategy for doing this calculation is to first count how many times boxes in the LIP trigger fired as a function of energy deposited in them. Figure 6.2 shows this distribution for all boxes where a single track hit three horizontal faces and met all of the cuts described in Chapter 5.5. There is one entry in the histogram for each box hit by the track.

In order to turn the previous distribution into a trigger efficiency as a function of energy, it must be normalized by the number of events which could have caused the box in the LIP trigger to fire. To do this we first make a Monte Carlo of the path lengths of particles passing through the scintillator counters. In order to assure that the proper angular and spatial distributions are chosen, track parameters are taken from actual events, and those tracks are required to pass through boxes which were working properly at the time.

If one knows the positions of all of the scintillator boxes perfectly and there are never any tracking errors, then the distribution of the number of boxes hit as a

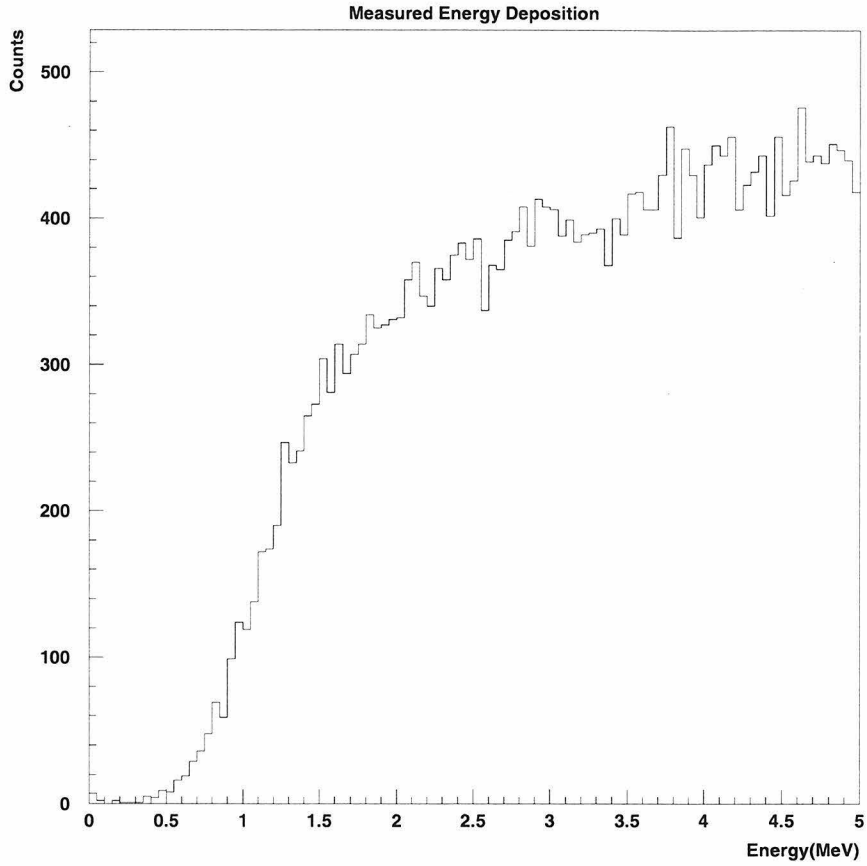

Figure 6.2: Number of counters with a given energy loss. Each box hit by a track is entered once into this histogram. In order for an event to be entered into this histogram, a single track must have hit three horizontal faces.

function of path length (for path lengths less than 19 centimeters) is expected to be flat. However, errors in tracking and uncertainties in the box positions cause this distribution to become sloped. This is because if sometimes a mistake is made in the tracking parameters, the track that is reconstructed will miss the box (even though the particle actually did pass through the box). This becomes more likely for smaller path lengths because the only way to get a very small path length is for the track to hit the box very close to the edge of the counter. This is where an error is most likely to make the track miss the box.

A 2 *cm* gaussian smearing was added to the X and Y intercepts of the Monte Carlo track and the path length was converted to energy by multiplying by $\frac{dE}{dx} =$ 1.84 MeV/cm. This normalization was chosen because it is the energy of a minimum ionizing muon as calculated by the same GEANT simulation used for the calibration. The smearing parameters were an ad hoc choice which seemed reasonable.

Figure 6.3 shows the output of the Monte Carlo superimposed with the actual measured distribution of path lengths $\times$ 1.84 MeV/cm.

The Monte Carlo and the actual data are in reasonable agreement. Since we do not know exactly what measurement errors are present, and thus do not know how to simulate them, we will actually use the path length distribution taken from the data to calculate the efficiency.

Unlike the Monte Carlo, in the data there are actually two effects which cause the distribution of path lengths to not be flat for small energies. As before there is the problem of tracking errors and the knowledge of the position of the box. However, there is also another effect which must be considered. For very small path lengths, the box should never have triggered and so the path length distribution taken from the data is biased.

It turns out for us, however, that this is a small effect compared to the number of times the box is missed due to tracking errors and thus can be ignored. The proof of this is that the Monte Carlo, which includes only tracking errors, reproduces the distribution as seen in the data.

Before we can divide the contents of figure 6.2 by the contents of figure 6.3 to get

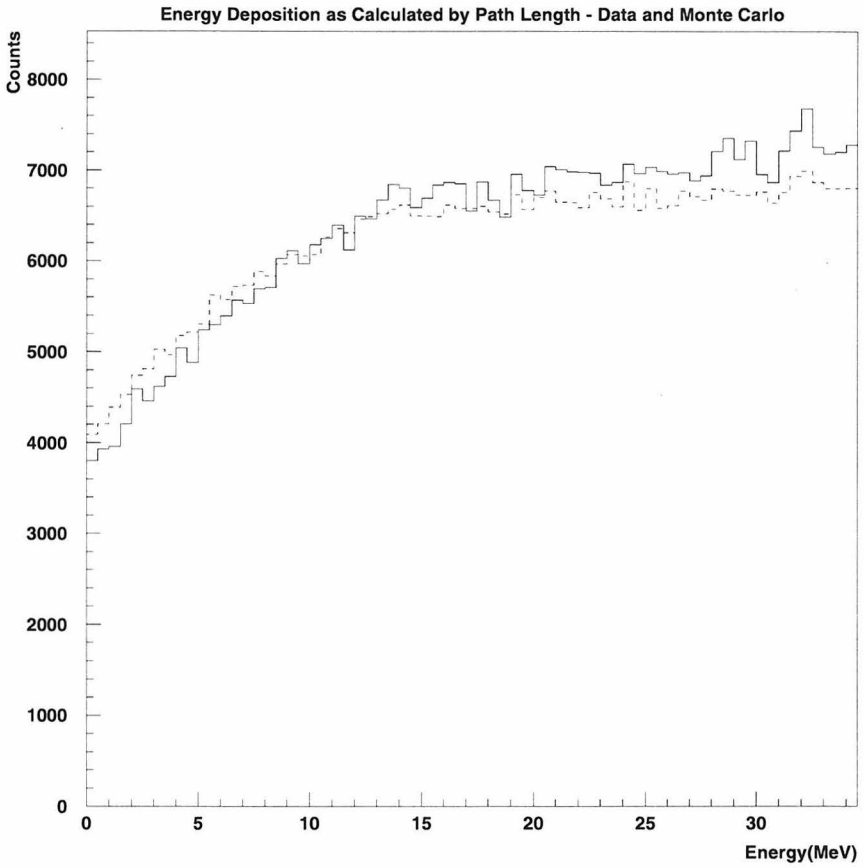

Figure 6.3: The distribution of path lengths converted to energy for both the data and Monte Carlo. The Monte Carlo angular distributions were chosen from real data and the intercepts of the space tracks have been smeared with a 2 cm gaussian.

the triggering efficiency as a function of energy, the two histograms must be properly normalized to each other. Multiplying the path length of the track through the box by 1.84 MeV/cm was only an approximation to the true energy loss. Because of the Landau distribution and photo-electron statistics a set of particles passing through a scintillator counter with the same path lengths will have a range of possible energies.

In order to estimate the fraction of the events contained in figure 6.3 that would actually have the energy obtained by simply multiplying by 1.84 MeV/cm, two more distributions were made. First, figure 6.4 shows the number of events as a function of energy for all events with a path length $\times$ 1.84 MeV/cm less than 15 MeV. As can be seen in this figure some fraction of the events (40%) actually have energy greater than 15 MeV. This is due to the fact that the energy loss follows the Landau distribution.

It is also possible for particles with path lengths $\times$ 1.84 MeV/cm greater than 15 cm to have energies less than 15 MeV. This is due to both the intrinsic width of the Landau distribution and photo-electron statistics. Figure 6.5 shows the number of events as a function of energy for all events with a path length $\times$ 1.84 MeV/cm greater than 15 MeV. As can be seen there are indeed some boxes which have less than 15 MeV of energy deposition.

The fraction of counters with less than 15 MeV of energy is 79.5% of the number of counters which have a path length $\times$ 1.84 MeV/cm less than 15 MeV. Applying this normalization factor we divide the distribution of the number of counters with a given energy deposition by the distribution of the number of counters we expected to trigger, based on the path length distribution multiplied by the normalization factor. The resulting efficiency distribution is shown in figure 6.6. The fact that some efficiencies appear greater than 100% is due to the normalization factor only being an estimate of the true normalization as a function of energy.

The threshold function as described in equation 6.3 is superimposed on the efficiency distribution. The energy threshold used in equation 6.3 is 1.2 MeV and the electronic resolution is 0.4 MeV. The data are well described by such a function and reach a flat efficiency of 100%.

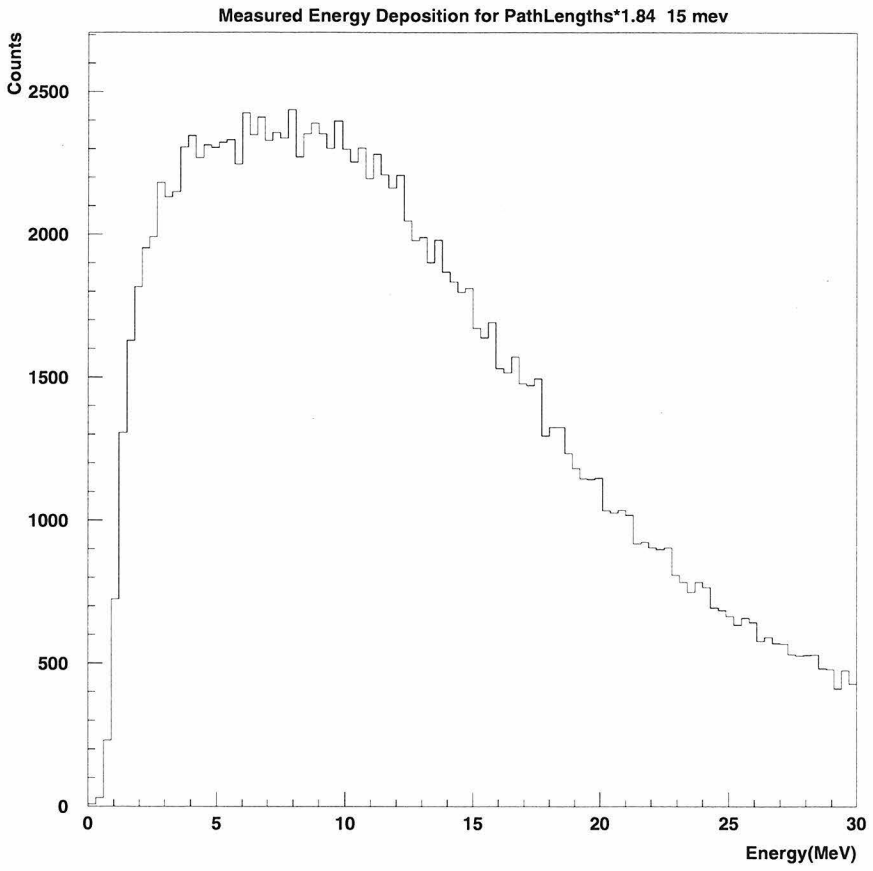

Figure 6.4: The number of counters hit as a function of energy for counters with a path length times 1.84 MeV/cm less than 15 MeV. Only about 60% of the events actually have an energy less than 15 MeV. The rest have fluctuated high due to the Landau distribution.

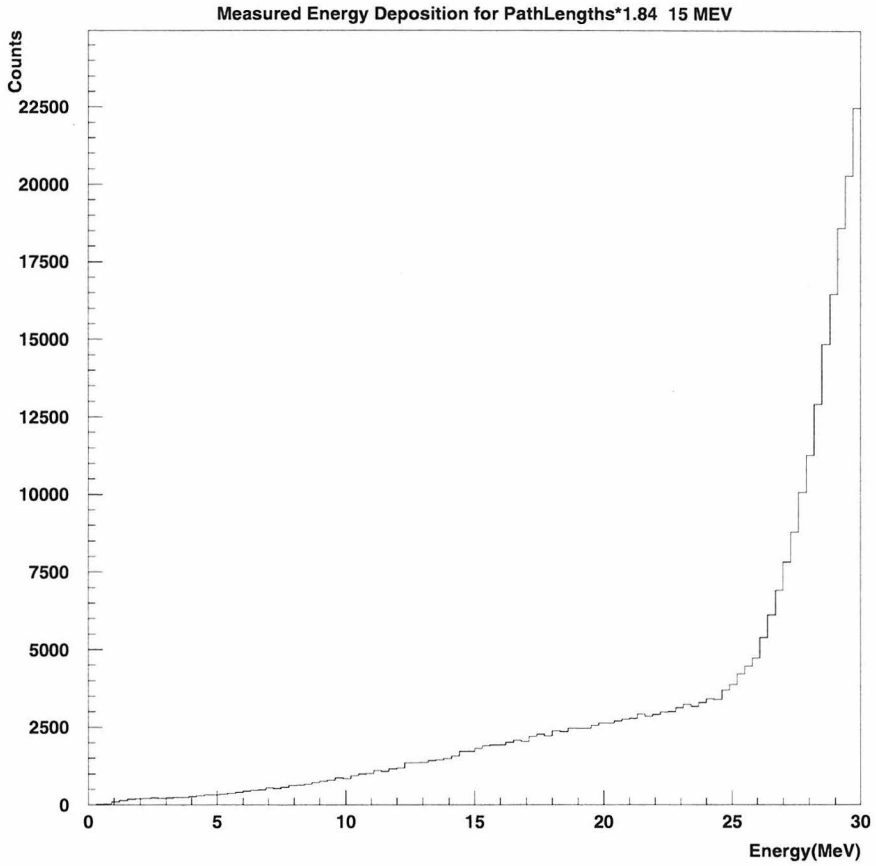

Figure 6.5: The number of counters hit as a function of energy for counters with a path length times 1.84 MeV/cm more than 15 MeV. Some of the boxes fluctuate to less than this value.

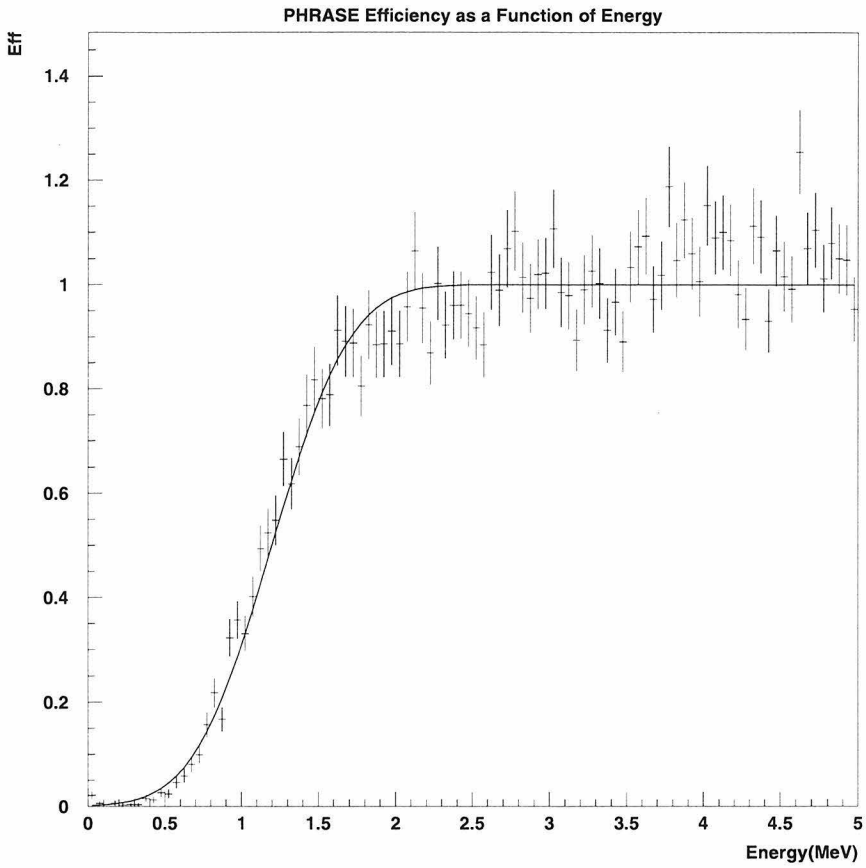

Figure 6.6: The estimated efficiency of triggering the low energy PHRASE trigger and the LIP trigger as a function of energy. The function drawn is the threshold function described in equation 6.3 with a threshold of 1.2 MeV and a resolution of 0.4 MeV.

6.2 Monte Carlo Generated LIPs

With the threshold function at low energy and an explicit cut at higher energy to remove muons from the sample it is possible to calculate the efficiency of this search to particles of different fractional charge. The technique to do this will be to use the same GEANT Monte Carlo that was used to generate the low energy spectrum in Chapter 4 and to propagate LIPs through the scintillator volume with it. In order to simulate LIPs in the GEANT Monte Carlo, muons are propagated through MACRO counters and the following two operations are performed on their energy loss:

1. The energy loss (before the saturation and photo-electron smearing is taken into account) is scaled by the square of the charge of the LIP. For example, if a $\frac{1}{3}e$ charged particle is being generated, then the energy lost is multiplied by $\frac{1}{9}$ in order to obtain the the simulated energy loss of the LIP. There are also logarithmic dependences on the charge in the Bethe-Bloch energy loss formula [17], but over the whole range considered here this effect produces less than a 10% discrepancy, which is to be compared to the 20% smearing due to photo-electron statistics at low energy.

2. In chapter 4 the resolution is given as 18% over the square root of energy. There is also a constant term at higher energies that is due to several effects. Some of these are:

   - The variation in calibration constants from counter to counter
   - The differences in linearity from 1 to 40 MeV from WFD channel-to-channel
   - The quality of the calibration constants over the entire counter when short path lengths and the response function of the counter are taken into account.

In order to calculate what the constant term should be we use the Monte Carlo to generate muons with several different such terms and then compare the resulting

maximum box energy distributions with those obtained from data in Section 5.5. Figure 6.7 is the maximum box energy distribution for single tracks presented earlier in Section 5.5. Superimposed on top of this distribution is the output from three different runs of the Monte Carlo with 1%, 10%, and 20% additional energy smearing. Figure 6.8 is the same for the multiple track sample.

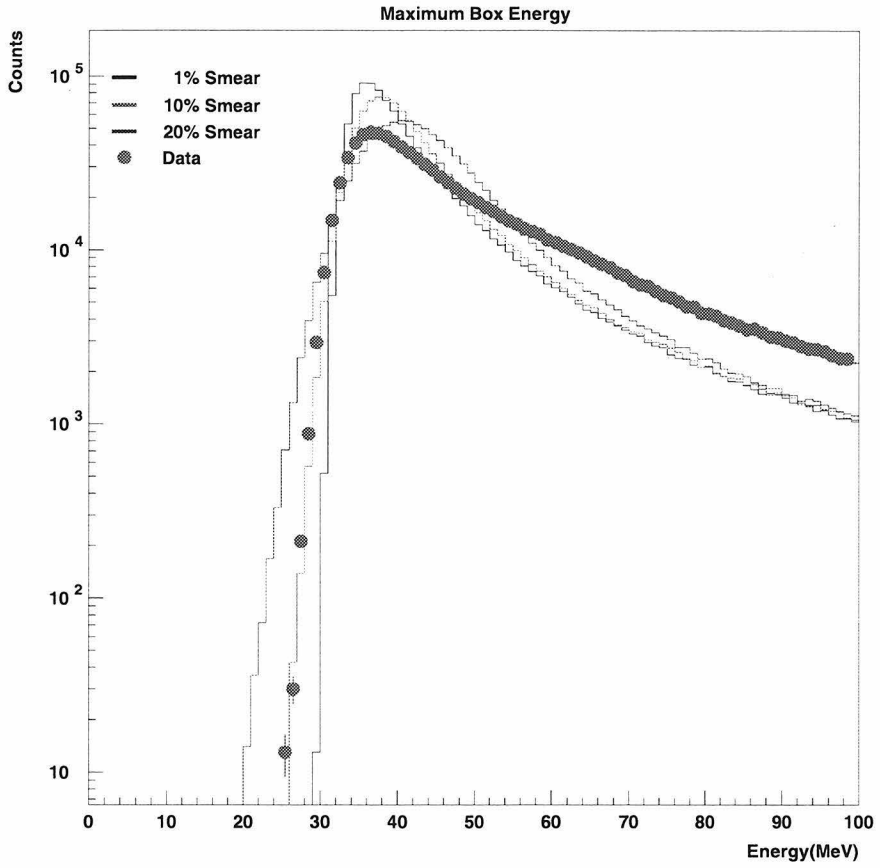

Figure 6.7: The single track maximum box energy distribution. There are three runs of the Monte Carlo superimposed. They have a 1%, 10%, and 20% constant energy term added to the resolution. Each distribution has the same number of events.

The data are consistent with a 10% extra constant term in the energy resolution. Therefore, the energy resolution will now be taken as:

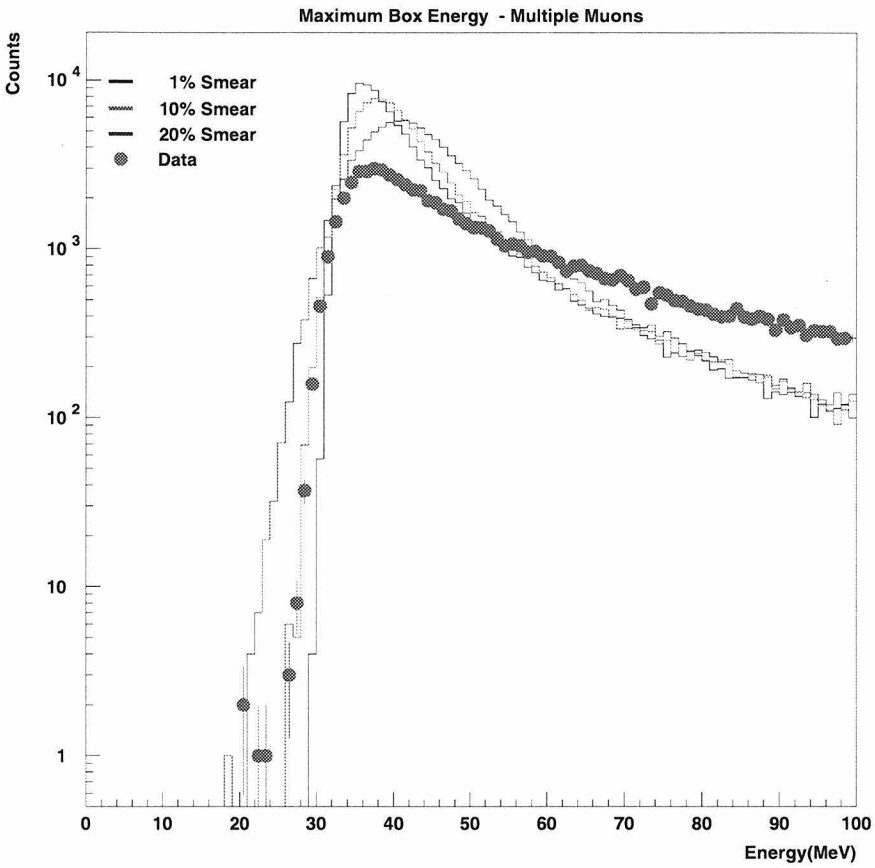

Figure 6.8: The multiple track maximum box energy distribution. There are three runs of the Monte Carlo superimposed. They have a 1%, 10%, and 20% constant energy term added to the resolution. Each distribution has the same number of events.

$$\frac{\Delta E}{E} = 18\% \left(\frac{1 \text{ MeV}}{\text{E}}\right)^{\frac{1}{2}} + 10\%. \tag{6.4}$$

Although the low energy tail of the muon distribution fits the data well, the same cannot be said of the high energy tail. Compared to the Monte Carlo distribution, there are more events in the tail than there are in the peak. This means that there are more events at high energy than we predict with the Monte Carlo. This is actually as we expect. The Monte Carlo is a single box Monte Carlo and does not take into account the extra energy that comes from showers and delta rays from other parts of the detector. For our purposes we are only really interested in the low energy part of the distribution. This is because it is the background to the LIP search. By determining where we no longer expect to see events due to muons, we define the range in which we are sensitive to LIPS.

Figure 6.9 shows the result of the Monte Carlo for $\frac{1}{5}\epsilon$, $\frac{1}{4}\epsilon$, $\frac{1}{3}\epsilon$, $\frac{1}{2}\epsilon$, and $\frac{2}{3}\epsilon$ charged particles. For each charge the maximum box energy distribution is produced.

It is clear from figure 6.9 that, depending on where we define the region to be free of muon events to be, the efficiency for detecting $\frac{2}{3}\epsilon$ charged particles will be greatly affected. Likewise, the PHRASE threshold function will determine the efficiency for detecting $\frac{1}{5}\epsilon$ charged particles and lower.

6.3 Efficiency of Analysis

In order to calculate the efficiency of this search to different fractional charges, LIPs are produced with the Monte Carlo as in figure 6.9; then we check whether or not the energy deposited by that particle is greater than the energy required by the PHRASE to fire and whether the energy deposited is less than the cut applied to exclude muons from the search.

Based on the expected background as calculated and plotted in figure 6.8, we consider any event that has a maximum box energy below 20 MeV to be a LIP candidate. In the efficiency calculation we use 20 MeV as the value of the cut.

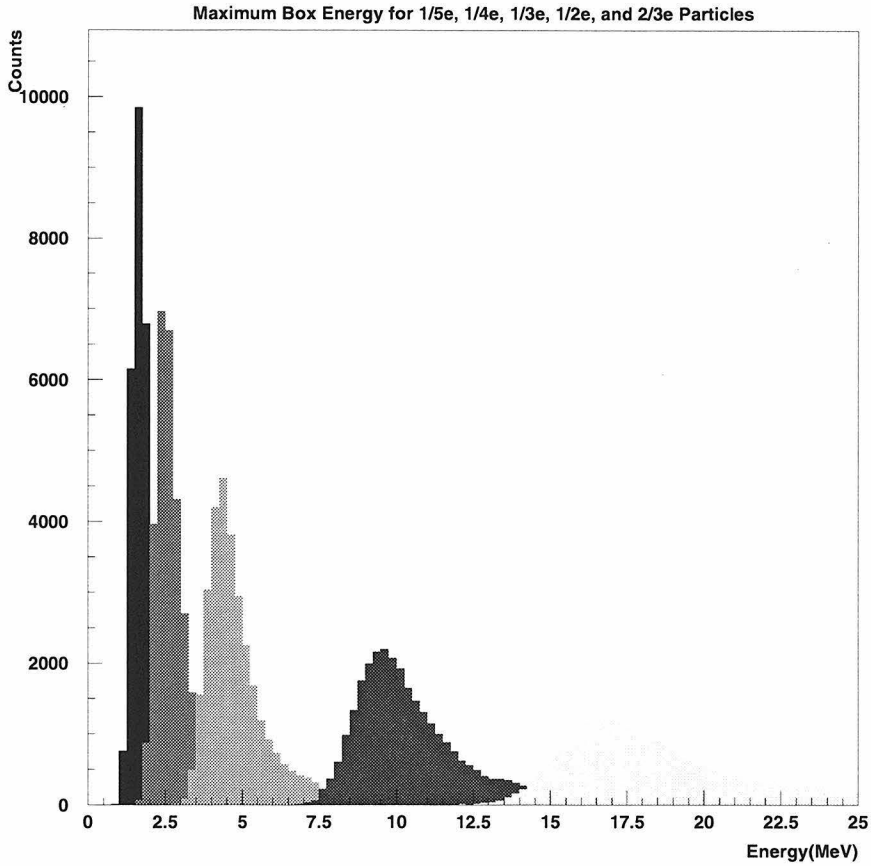

Figure 6.9: The maximum box energy distribution for $\frac{1}{5}$ e, $\frac{1}{4}\epsilon$, $\frac{1}{3}\epsilon$, $\frac{1}{2}\epsilon$, and $\frac{2}{3}\epsilon$ charged particles.

As was noted earlier the data has more events at higher energy than the Monte Carlo. If an actual LIP particle had the same high energy tail as a muon then the efficiency for detecting it would be lower than the Monte Carlo suggests because a larger fraction of the data would be indistinguishable from muons, because the maximum box energy for those events would be larger than 20 MeV.

In order to be conservative, we have calculated the efficiency assuming that LIPs have the same high energy tail as muons. This was accomplished by rescaling the muon maximum box distribution by the square of the desired charge. Since delta ray production (which is the reason the Landau distribution has a high energy tail) depends only on the charge of the incident particle, the shape of the energy loss distribution, and not only the mean, should scale with the square of the charge of the incoming particle. Figure 6.10 shows the calculated efficiency for both the Monte Carlo and the rescaled data.

When calculating the limit the more conservative rescaled data will be used for the efficiency.

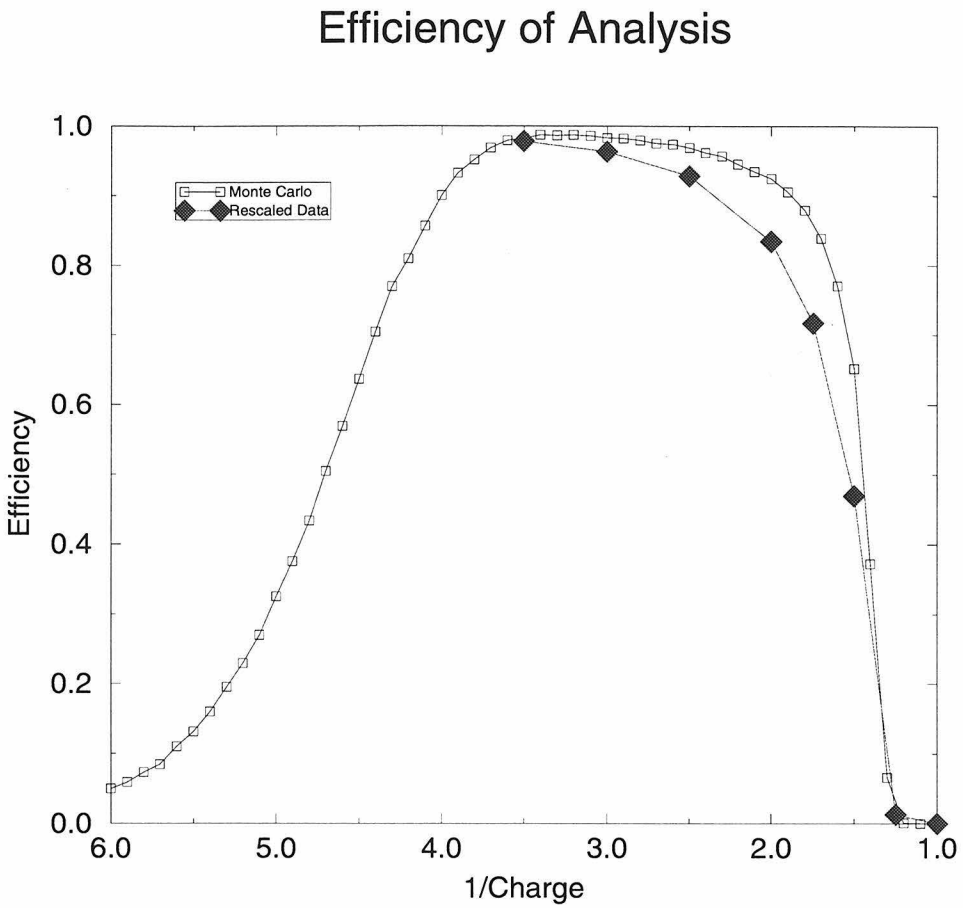

Figure 6.10: Efficiency of the search for different fractional charges. The efficiency is limited at low energies by the PHRASE threshold and the requirement that all three faces of the detector must trigger, and at high energies by the cut at 20 MeV. Both the data from the Monte Carlo and the rescaled muon data are shown.

Chapter 7 Geometrical Acceptance of the Search

Before this result can be converted into a limit, a calculation of the geometrical acceptance must be done, where:

$$Acceptance = \int \epsilon(X, Y, \theta, \phi)\ d\vec{A} \cdot d\vec{\Omega}. \tag{7.1}$$

We calculate the above integral for the case of an open box (i.e., two rectangular planes of area A separated by distance d). Because of our geometry and the fact that no tracks are allowed to pass through the vertical walls, this is an adequate description. It should be noted that, based on the calculation presented in Section 2.4.1, it is assumed if a track passes through all three scintillator planes, it will also pass though ten planes of streamer tubes and at least six of them will fire. The efficiency factor ϵ is the probability that all three planes in the detector have been hit in active boxes inside their fiducial area. Equation 7.1 can be rewritten as follows:

$$Acceptance = \int \epsilon(X, Y, \theta, \phi) dX dY \cos\theta \sin\theta d\theta d\phi. \tag{7.2}$$

The $\cos\theta$ factor comes from the dot product in equation 7.1 and the $\sin\theta$ is part of the solid angle. dX and dY are the coordinates of the top plane, and the integrals over angle are performed such that all tracks pass between the two planes.

In order to make the task computationally easier, we make a transformation so that instead of integrating over angle, we only have to integrate over the two areas of the upper and lower planes. If we make this variable transformation, then we must introduce the proper Jacobian:

$$|J| = \frac{\cos^3\theta}{d^2 \sin\theta}. \tag{7.3}$$

Rewriting equation 7.3 we now have:

$$Acceptance = \int \epsilon(X_1, Y_1, X_2, Y_2) \frac{\cos^4\theta}{d^2} dX_1 dY_1 dX_2 dY_2, \tag{7.4}$$

where the integration is over the areas of the top and bottom plane. Now, if we use the fact that:

$$\lim_{N\to\infty} \frac{b-a}{N} \sum_{i=1}^{N} y(x_i) = \int_a^b y(x) dx, \tag{7.5}$$

where the x_i are uniform random numbers between 0 and 1, we can rewrite equation 7.4 in the form of the following sum:

$$Acceptance = \frac{A_1 A_2}{d^2} \times \frac{1}{N} \sum_{i=1}^{N} \epsilon(X_{1_i}, Y_{1_i}, X_{2_i}, Y_{2_i}) \cos^4\theta_i. \tag{7.6}$$

As was previously mentioned $\epsilon(X_{1_i}, Y_{1_i}, X_{2_i}, Y_{2_i})$ is an efficiency factor in the sum which is 1 if all three faces are hit in good boxes and 0 if not. This is how both cracks and boxes without good calibration constants are taken into account. In practice an open box larger than MACRO is placed around the MACRO geometry and points are chosen randomly on the two planes. ϵ is determined for every event and the sum is carried out for a calculation of the acceptance. Table 7.1 contains the results of the acceptance calculation.

The geometrical acceptance has been calculated separately for each supermodule and inter-supermodule pair. In calculating the limit presented in Chapter 8 these acceptances are multiplied by the live time for that particular supermodule or inter-supermodule pair. The acceptances are calculated for seven sub-periods of running. The calibration constants were calculated separately for each of these periods and there are different operational scintillator counters in each.

SM	1	2	3	4	5	6	7
1	215.9 ± 4.5	215.8 ± 4.5	191.7 ± 4.2	215.9 ± 4.5	167.1 ± 4.0	215.9 ± 4.5	215.9 ± 4.5
2	162.8 ± 3.8	191.3 ± 4.2	204.6 ± 4.4	181.6 ± 4.2	181.6 ± 4.1	181.6 ± 4.1	181.6 ± 4.1
3	153.9 ± 3.8	190.4 ± 4.2	133.8 ± 3.5	174.2 ± 4.0	174.1 ± 4.0	174.1 ± 4.0	174.1 ± 4.0
4	202.2 ± 4.4	214.2 ± 4.5	214.2 ± 4.5	214.2 ± 4.5	214.2 ± 4.5	214.2 ± 4.5	214.2 ± 4.5
5	162.3 ± 3.9	102.1 ± 3.1	225.0 ± 4.6	225.0 ± 4.6	225.0 ± 4.6	225.0 ± 4.6	225.0 ± 4.6
6	107.9 ± 3.2	11.8 ± 1.0	168.5 ± 4.0	181.5 ± 4.1	181.5 ± 4.1	181.5 ± 4.1	153.3 ± 3.8
1/2	71.2 ± 2.2	67.8 ± 2.1	71.2 ± 2.2	71.2 ± 2.2	71.2 ± 2.2	71.2 ± 2.2	71.2 ± 2.2
2/3	33.1 ± 1.4	63.0 ± 2.0	61.5 ± 2.0	55.3 ± 1.9	55.3 ± 1.9	55.3 ± 1.9	55.3 ± 1.9
3/4	52.6 ± 1.8	70.8 ± 2.2	56.4 ± 2.0	70.8 ± 2.2	70.8 ± 2.2	70.8 ± 2.2	70.8 ± 2.2
4/5	56.2 ± 1.9	56.9 ± 1.9	78.8 ± 2.3	78.8 ± 2.3	78.8 ± 2.3	78.8 ± 2.3	78.8 ± 2.3
5/6	64.1 ± 2.1	25.3 ± 1.3	70.8 ± 2.2	75.2 ± 2.2	75.2 ± 2.2	75.2 ± 2.2	75.2 ± 2.2

Table 7.1: The calculated acceptance for each supermodule and inter-supermodule pair. The results of the calculation are presented for each of seven sub-periods of the run. These periods were calibrated separately and each have different operational scintillator counters.

Chapter 8 Conclusions

In the approximately one year of running that this search covers, no candidates for LIPs were observed. This search was sensitive to particles with charges greater than $\frac{1}{5}e$. The detector is sensitive to particles with β of between approximately 0.25 and 1.0. Unlike previous experiments, this search attempted to find LIPs in both single track events and buried among the tracks of multiple muon showers.

For the single track sample, assuming an isotropic flux, in the region of 100% efficiency this corresponds to a 90% C.L. upper flux limit of $\Phi \leq 9.2 \times 10^{-15}\ cm^{-2} sec^{-1} sr^{-1}$.

The two best experiments to compare to are the LSD experiment [21] and the Kamiokande experiment [18]. While LSD claims to have the best scintillator-based limit in the world, Kamiokande has the lowest limit. Both of these experiments only claim sensitivity to $\frac{1}{3}\ e$ and $\frac{2}{3}e$ charged particles.

Table 8.1 summarizes the limits of this search in comparison to other searches:

Search	Charge				
	$\frac{1}{5}$	$\frac{1}{4}$	$\frac{1}{3}$	$\frac{1}{2}$	$\frac{2}{3}$
LSD	-	-	2.3×10^{-13}	Not Quoted	2.7×10^{-13}
This Search	2.8×10^{-14}	1.0×10^{-14}	9.5×10^{-15}	1.1×10^{-14}	2.0×10^{-14}
Kamiokande	-	-	2.1×10^{-15}	Not Quoted	2.3×10^{-15}

Table 8.1: A summary of limits in LIP searches. This limit is compared with limits from the water Čerenkov Kamiokande experiment and the scintillator based LSD experiment. The MACRO experiment is alone in setting a limit on $\frac{1}{5}e$ and $\frac{1}{4}e$ charged particles.

For the entries marked "Not Quoted," the experiments do not report a limit for that charge although the experiment should have been sensitive to that energy deposition. At least in the case of LSD, there were two candidates in the $\frac{1}{2}e$ region which were ignored because they were not considering $\frac{1}{2}e$ charged particles. In the Kamiokande experiment only $\frac{1}{3}e$ and $\frac{2}{3}e$ were searched for.

Unlike the other two searches this search is sensitive to a continuous range of charges from $\frac{1}{5}e$ to close to the charge of an electron. This limit is shown in figure 8.1.

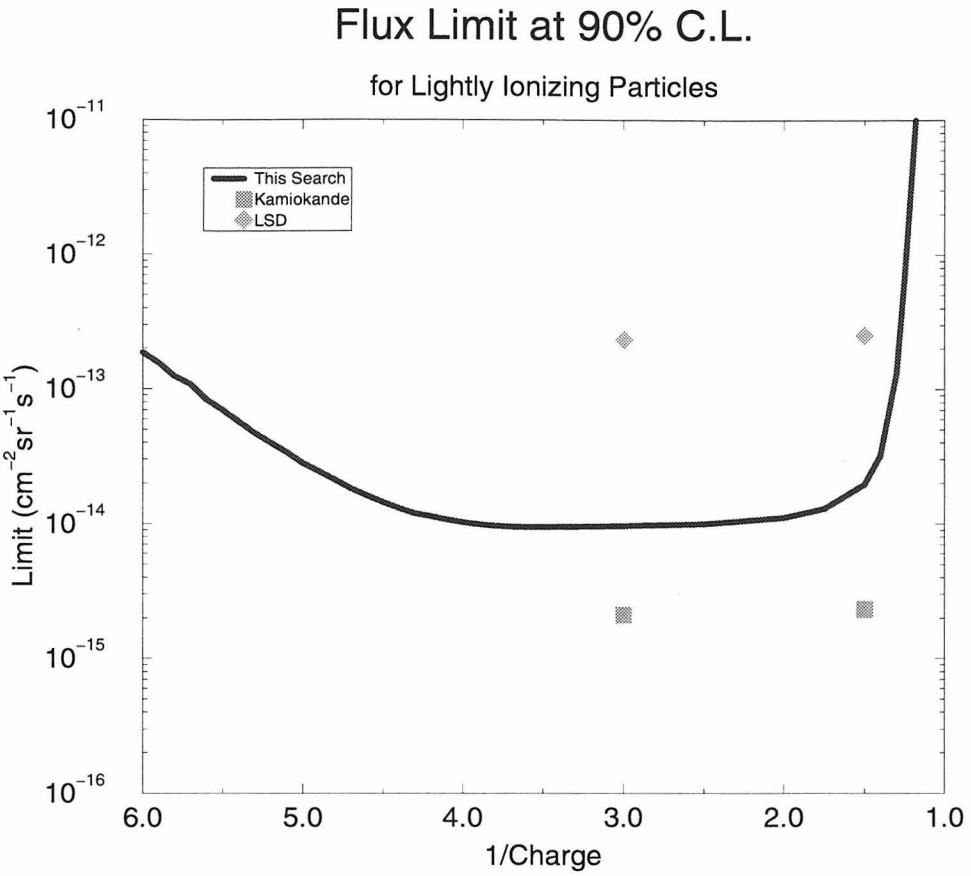

Figure 8.1: The upper limit on LIP fluxes at 90% confidence level established by this search. Also shown are the limits from the searches done at the Kamiokande and LSD experiment. Unlike those experiments we report a limit for a continuous range of charges.

Another thing to note is the qualitative difference in the type of search being done compared with the other searches. While this search had no candidates and required hand scanning of only 3 in 1.2 million events, LSD had 4 candidates out of 5674 events and Kamiokande needed to hand scan over 4800 events.

There are differences between MACRO and the other experiments that should be considered before comparing the limits presented in this search and those of the other experiments. First of all, the limit is calculated for an isotropic flux over all 4π of

solid angle. In this search, MACRO has almost no sensitivity to the portions of that flux which are horizontal. All of the acceptance comes from particles which are going vertically through the detector. The acceptance of the Kamiokande experiment is quite different. Unlike MACRO, much of its acceptance comes from particles coming horizontally.

If LIPs are produced in the rock of the tunnel around MACRO, then an isotropic flux would be a reasonable assumption about the direction they would arrive from. If on the other hand, LIPs are either produced in the upper atmosphere or are impinging on the earth from outer space, it is not a valid assumption at all. Although it is true that LIPs will travel farther through material than muons, they would not be able to travel through the entire earth. A $\frac{1}{5}e$ charged particle would travel 25 times as far as a muon by virtue of its reduced energy loss, but that distance would be nowhere near what was needed to travel all the way from the far side of the earth.

For LIPs coming from somewhere above the surface of the earth, the angular distribution should be similar to the downward going muon flux. For the MACRO experiment, only considering particles which could survive passing through the rock to reach the detector would reduce the calculated acceptance by about a factor of two (since downward but not upward going particles would be accepted). For the Kamiokande experiment the acceptance would be reduced by a larger factor since only that part of the flux with a vertical downward component would be relevant.

Finally, when comparing limits for LIP searches in the cosmic radiation the depth of the experiment should be considered. An experiment on the surface of the earth will be exposed to more muons but subjected to worse backgrounds from sources such as soft photons from showers. Also, the proportion of the flux which contains LIPs increases the deeper the experiment is located. Since particles with fractional charge lose less of their energy when they pass through material than muons, they also range out less quickly. Therefore, the deeper the experiment is located, the higher the fraction of muons which have stopped in the earth relative to the LIPs contained in the flux. The average thickness of rock over the MACRO detector is 3700 meters of water equivalent. The Kamiokande experiment has an overburden of 2700 meters

of water equivalent, and the LSD experiment is covered with 5000 meters of water equivalent.

Appendix A Introduction to Neural Networks

For a more general introduction to neural networks, see reference [43]. In general, a neural network is no more then a non-linear fitting procedure with many adjustable parameters. Neural networks are based on ideas and observations from biology. A biological neuron has many inputs, and if enough of them pass some threshold, then the output of the neuron fires. The same thing can be implemented mathematically. Figure A.1 shows a neuron of a neural network.

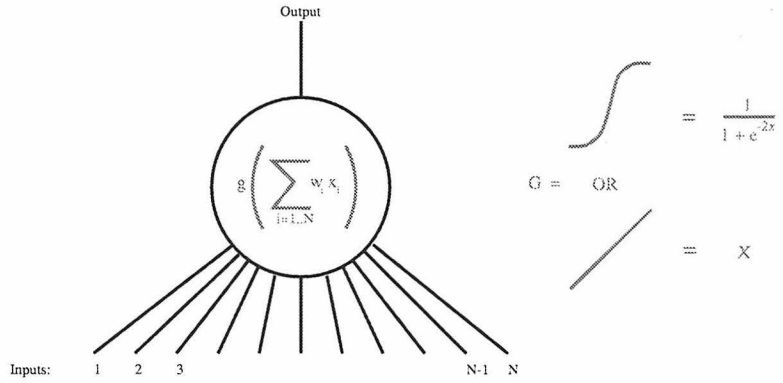

Figure A.1: A neuron for use in a neural network. The neuron has several inputs and only one output. The output is a function of the sum of all of its inputs each multiplied by some weight. The function can either be a non-linear sigmoid function where the output is either forced to be "on" or "off," or a continuous function such as the sum of all of the inputs.

The inputs are all summed with each input assigned its own weight. Then, the sum is passed through a function. In general, this function is non-linear and in practice it is usually in the form of a "sigmoid function." This is a function that is forced to either one or zero. A common form of a sigmoid function is:

$$g(x) = \frac{1}{1 + e^{-2x}} \tag{A.1}$$

It is also possible to have the output of the neuron be linear. In this case, instead

of the neuron either "firing" or being "off," the output of the neuron is simply the sum of all of the inputs multiplied by their respective weights.

To solve a problem using a neural network, many of these neurons are attached together into a network. In a *feed forward* network the neurons are arranged in layers and typically the inputs to each neuron are the outputs of all of the neurons in the previous layer. Such arrangements are referred to as *fully connected* networks.

Each layer in the network has fewer neurons in it than the one before it, until finally in the last layer there are only one or two output neurons. The inputs to the network (some set of variables which have been chosen to represent the problem) are fed into the inputs of the first layer of neurons. Layers of neurons between inputs and outputs are known as *hidden layers*. The number of layers and the number of neurons in each layer are selected depending on computing resources, the amount of data, and the problem being solved.

In classification problems, where the network is asked to identify whether an item belongs to one set or another, all of the neurons including the output neuron are sigmoid functions. This forces the output into a discrete choice (*e.g.*, whether a particle is π or μ). In a problem where the required answer is a continuous variable (such as the mass of a peak or a position in a piece of apparatus), then the output is usually a linear neuron. The neurons of the hidden layers however, are still usually sigmoids. For some examples where networks with continuous outputs have been used in physics, see references [44, 45].

If all of the weights for each neuron are set properly, then for a given set of inputs, the output neuron(s) will give the answer which is desired. The process of setting these weights is known as *training*. A set of training data is prepared for which the desired answer is already known. These data are then presented repeatedly to the network and the weights are adjusted until the output neuron(s) reproduce the desired answers with some accuracy. For more details on training networks, see references [43, 44, 45]. This process is, in fact, a minimization procedure and many different schemes can be used depending on the problem being approached. The popular HEP program JETNET [43] has many of these procedures available in

functions which can be called from C++ or FORTRAN programs.

Appendix B LIP Trigger Technical Specifications

The LIP trigger is a CAMAC module which manages input signals from several different parts of the detector. Each LIP trigger module covers one supermodule's worth of the MACRO detector. It organizes all of the scintillator counters in each supermodule into three logical faces. The counters of the attico (including the upper vertical tanks) are the "top" layer. The center tanks are the "center" layer, and the bottom tanks (along with the lower vertical tanks) are grouped into the "bottom" layer. In addition the OR of half of each layer is passed to the LIP modules in the adjacent supermodules. These are referred to as the "adjacent" inputs and outputs. These inputs allow the LIP to trigger on particles which pass from supermodule to supermodule. This layout is shown in figure B.1.

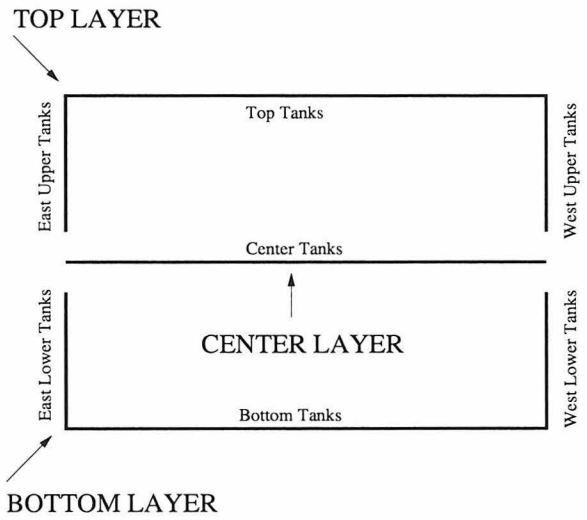

Figure B.1: The organization of the LIP boxes in one supermodule.

In order for a trigger to be formed, the first condition which must be met is a scintillator coincidence either between all three logical layers or between two layers in one supermodule and one layer in another. This condition is called the "scintillator pre-trigger." The occurrence of a scintillator pre-trigger causes a LED to flash and a

signal to be generated at a LEMO connector on the front panel.

After the scintillator pre-trigger, the information about which scintillator tanks have fired is latched for possible later readout. Then, the system waits for a trigger from the streamer tube system. The amount of time the system waits is a fixed number of clock cycles. In actual running it is 6.4 μsecs. If both of these conditions are met, the circuit issues a trigger output and a stop signal to the 200 MHz waveform digitizer system. In the case that the LIP circuit triggers on a particle passing between two supermodules, the LIP in both supermodules trigger independently.

Although it is possible to operate the LIP trigger without the requirement of the streamer tube inputs (in this case the pre-trigger causes both the trigger and wave form digitizer stop), it is nonetheless necessary in practice. Each individual scintillator counter fires at $\approx$ 2-3 kHz. This rate is set by ambient radioactivity in the experimental hall and in the detector itself. There are over 70 tanks in each super-module. With only the scintillator coincidence required, the trigger rate would be several Hz. In addition to taxing the abilities of the acquisition system, almost all triggers would be from random radioactivity.

After a trigger has been produced, six 16 bit CAMAC registers are read out from the LIP. These contain the information about which of the 76 tanks in the SM caused the scintillator trigger. This information is used both in event reconstruction and in deciding which channels of the waveform digitizer should be read out. The use of WFDs (as opposed to a traditional ADC/TDC system) helps to suppress backgrounds that can result from small radioactivity pulses starting an ADC/TDC gate too early. This can result in the partial integration of a pulse which then is reconstructed with a much smaller energy than was actually deposited in the tank.

The LIP trigger itself is completely digital. Because of this, another system must be used to discriminate on energy. The LIP trigger uses the lowest energy-based scintillator triggers available in MACRO. Its inputs are the individual box triggers produced in the PHRASE (one of the gravitational collapse triggers) which have a trigger threshold of $\approx$ 1.2 MeV. More information on the PHRASE can be found in [31].

Specially built cables bring the signals from the PHRASE to the LIP trigger. Since the front panel of the PHRASE required a LEMO connector, blocks of 8 RG174 cables were prepared which had 8 LEMO connectors on one side and a single AMP block connector on the other. The AMP connector allows a high density front panel for the LIP with 84 tank inputs along with the streamer tube inputs, trigger outputs and informational LEDs all in one triple-width CAMAC module.

Once the digital NIM level signals are brought from the PHRASE to the front panel of the LIP, they are transfered from the block AMP connectors of the cables into the AMP headers for the cables on the front panel and then onto a printed circuit board (PCB) which forms the backing of the front panel. The signals then pass through board-to-board interconnects and onto the main LIP PCB which is set at 90° to the front panel board.

PHRASE and streamer tube signals are converted into TTL signals by ECL 100325 ECL to TTL converter chips. Each channel of the 100325 has two inputs. One input is for the incoming NIM signal and one is for a reference voltage that will be used for the triggering comparison. Each of the reference voltage inputs are attached to a voltage plane in the PCB and stabilized with a .1μFarad capacitor. The voltage of the reference plane is controlled by an adjustable voltage regulator and a turn pot. The reference voltage is adjusted so that TTL pulses are are formed whenever the NIM inputs are lower than -0.6 Vs.

All of the logic and readout decisions are handled with XILINX field programmable gate array chips. There are two XILINX chips on each board: a 175 pin XC3090 and a smaller 68 pin XC3020. The main advantages of using XILINX chips instead of discrete logic chips are their density, reusability, and the flexibility they afford if design changes are needed. The chips themselves are completely generic. In order to program their functionality, one uses a computer CAD system to program a 16K PROM (the XILINX XC1765).

The XILINX chips are each wired to a PROM. When power is applied to the chips, they load the information from the PROMs and configure themselves to perform the logic as requested in the design. Although the large XILINX chips cost on the order

of $100, the PROMS cost on the order of $5, and the entire design can be modified simply by changing only the socketed PROM chips.

Logically, the functionality of the trigger is divided between the two chips as follows: the scintillator pre-trigger and the CAMAC readout are contained on the larger 175 pin chip. The combination of the scintillator pre-trigger and the later arriving streamer tube information happens on the second smaller chip. If a streamer tube trigger arrives within 6.4 μsecs after the pre-trigger, then the second chip issues a trigger and stop signal. Otherwise, it issues a clear to the first chip.

The XILINX chips must be operated with a clock. The LIP trigger system now operates with a 5 MHz oscillator. When the discriminated energy inputs arrive at the LIP trigger, they are synchronized to the clock. Once the incoming signals have been synchronized, everything else in the design is completely synchronous. Each synchronizer produces a three clock cycle pulse for possible later readout in a register, and a two clock cycle pulse for use in the logic section of the circuit.

The two clock cycle pulses from all of the scintillator signals are ORed into their respective faces and then ANDed to make the three face scintillator coincidence. If there is a three fold coincidence, a latch signal is sent back to all of the latching counters and a scintillator pre-trigger signal is sent to the second XILINX chip.

Since the logic coincidence is done with the two clock cycle pulses and the coincidence is gated on the clock, a scintillator coincidence is guaranteed to happen if all three faces fire within one clock cycle of each other. The probability of having a coincidence falls from 100% down to zero as the coincidence window goes from one to two clock cycles.

The reason that a signal three clock cycles long is latched instead of the two clock cycle logic signal is to allow for the time it takes for the two clock cycle pulses to propagate to the AND gate, and for the latch signal to make its way back to the latches. The result of the AND gate occurs at the beginning of the second or third clock cycle (relative to the first clock cycle after the first pulse which arrived). The clock must be slow enough both to allow the ORed signals to make it to the AND before the next clock cycle arrives and for the latch signal to travel back to the latches

within that clock cycle.

When the scintillator pre-trigger arrives at the second chip, a gate of 6.4 μsecs is started. If during that gate one of the streamer tube inputs fires then a trigger and stop signal are generated. On the other hand, if by the end of the gate no streamer tube signals have arrived, then a clear signal is generated and sent back to unlatch the frozen latches. The system is then free to look for another scintillator coincidence.

In the case that a trigger has happened the latches stay locked for later readout. All of the latch outputs are attached to tri-state buffers which are in turn attached to a common set of bus lines which can be read out with CAMAC commands. The tri-state buffers are arranged into six groups. The top, center, bottom, east, west, and adjacent tanks can be placed as a group onto the 16 bus lines by asserting the enable on that group of tri-state buffers.

The circuit recognizes two CAMAC commands F9 (clear) and F0 (read). In the case of F0, the A lines are used to address which groups of tanks should be read out.

Appendix C The MACRO Author List

The MACRO Collaboration

M. Ambrosio[12], R. Antolini[7], G. Auriemma[14,a], R. Baker[11], A. Baldini[13], G. C. Barbarino[12], B. C. Barish[4], G. Battistoni[6,b], R. Bellotti[1], C. Bemporad[13], P. Bernardini[10], H. Bilokon[6], V. Bisi[16], C. Bloise[6], C. Bower[8], S. Bussino[14], F. Cafagna[1], M. Calicchio[1], D. Campana[12], M. Carboni[6], M. Castellano[1], S. Cecchini[2,c], F. Cei[13,d], P. Celio[14],V. Chiarella[6], A. Corona[14], S. Coutu[11], G. De Cataldo[1], H. Dekhissi[2,e], C. De Marzo[1], I. De Mitri[9], M. De Vincenzi[14,f], A. Di Credico[7,14], O. Erriquez[1], C. Favuzzi[1], C. Forti[6], P. Fusco[1], G. Giacomelli[2], G. Giannini[13,g], N. Giglietto[1], M. Grassi[13], A. Grillo[7], F. Guarino[12], P. Guarnaccia[1], C. Gustavino[7], A. Habig[8], K. Hanson[11], A. Hawthorne[8], R. Heinz[8], J. T. Hong[3], E. Iarocci[6,h], E. Katsavounidis[4], E. Kearns[3], S. Kyriazopoulou[4], E. Lamanna[14], C. Lane[5], D. S. Levin[11], P. Lipari[14], R. Liu[4], N. Longley[4], M. J. Longo[11], Y. Lu[15], G. Ludlam[3], G. Mancarella[10], G. Mandrioli[2], A. Margiotta-Neri[2], A. Marini[6], D. Martello[10], A. Marzari-Chiesa[16], M. N. Mazziotta[1], D. G. Michael[4], S. Mikheyev[7,i], L. Miller[8], M. Mittelbrunn[5], P. Monacelli[9], T. Montaruli[1], M. Monteno[16], S. Mufson[8], J. Musser[8], D. Nicoló[13,d], R. Nolty[4] C. Okada[3], C. Orth[3], G. Osteria[12], O. Palamara[10], S. Parlati[7], V. Patera[6,h], L. Patrizii[2], R. Pazzi[13], C. W. Peck[4], S. Petrera[10], N. D. Pignatano[4], P. Pistilli[10], V. Popa[2,l], A. Rainó[1], J. Reynoldson[7], F. Ronga[6], A. Sanzgiri[15], F. Sartogo[14], C. Satriano[14,a], L. Satta[6,h], E. Scapparone[2], K. Scholberg[4], A. Sciubba[6,h], P. Serra-Lugaresi[2], M. Severi[14], M. Sitta[16], P. Spinelli[1], M. Spinetti[6], M. Spurio[2], R. Steinberg[5], J. L. Stone[3], L.R. Sulak[3], A. Surdo[10], G. Tarlé[11], F. Tassoni[14], V. Togo[2], V. Valente[6], C. W. Walter[4] and R. Webb[15]

1. Dipartimento di Fisica dell'Università di Bari and INFN, 70126 Bari, Italy
2. Dipartimento di Fisica dell'Università di Bologna and INFN, 40126 Bologna, Italy
3. Physics Department, Boston University, Boston, MA 02215, USA
4. California Institute of Technology, Pasadena, CA 91125, USA

5. Department of Physics, Drexel University, Philadelphia, PA 19104, USA

6. Laboratori Nazionali di Frascati dell'INFN, 00044 Frascati (Roma), Italy

7. Laboratori Nazionali del Gran Sasso dell'INFN, 67010 Assergi (L'Aquila), Italy

8. Depts. of Physics and of Astronomy, Indiana University, Bloomington, IN 47405, USA

9. Dipartimento di Fisica dell'Università dell'Aquila and INFN, 67100 L'Aquila, Italy

10. Dipartimento di Fisica dell'Università di Lecce and INFN, 73100 Lecce, Italy

11. Department of Physics, University of Michigan, Ann Arbor, MI 48109, USA

12. Dipartimento di Fisica dell'Università di Napoli and INFN, 80125 Napoli, Italy

13. Dipartimento di Fisica dell'Università di Pisa and INFN, 56010 Pisa, Italy

14. Dipartimento di Fisica dell'Università di Roma "La Sapienza" and INFN, 00185 Roma, Italy

15. Physics Department, Texas A&M University, College Station, TX 77843, USA

16. Dipartimento di Fisica Sperimentale dell'Università di Torino and INFN, 10125 Torino, Italy

a Also Università della Basilicata, 85100 Potenza, Italy

b Also INFN Milano, 20133 Milano, Italy

c Also Istituto TESRE/CNR, 40129 Bologna, Italy

d Also Scuola Normale Superiore di Pisa, 56010 Pisa, Italy

e Also Faculty of Sciences, University Mohamed I, B.P. 424 Oujda, Morocco

f Also Dipartimento di Fisica, Università di Roma III, Roma, Italy

g Also Università di Trieste and INFN, 34100 Trieste, Italy

h Also Dipartimento di Energetica, Università di Roma, 00185 Roma, Italy

i Also Institute for Nuclear Research, Russian Academy of Science, 117312 Moscow, Russia

l Also Institute for Atomic Physics, 76900 Bucharest, Romania

Bibliography

[1] F. Halzen and D. Martin. *Quarks and Leptons*. John Wiley and Sons, New York, 1984.

[2] D. Perkins. *Introduction to Particle Physics*. Addison Wessley, Menlo Park, California, 1987.

[3] R. Millikan. *Phil. Magazine*, page 209, 1910.

[4] E. D. Bloom et al. High-energy inelastic e p scattering at 6-degrees and 10-degrees. *Phys. Rev. Lett.*, 23:930, 1969.

[5] Richard P. Feynman. Very high-energy collisions of hadrons. *Phys. Rev. Lett.*, 23:1415–1417, 1969.

[6] M. Gell-Mann. A schematic model of baryons and meysons. *Physics Letters*, 8:214, 1964.

[7] C. Wetterich. Half-integer charged hadrons from higher dimensions. *Physics Letters*, 167B:325, 1985.

[8] L. Lyons. Quark search experiments at accelerators and in cosmic rays. *Phys.Rep.*, 129:225, 1985.

[9] H. V. Klapdor-Kleingrothaus and A. Staudt. *Non Accelerator Particle Physics*. IOP, London, 1995.

[10] L. W. Jones. A review of quark search experiments. *Reviews of Modern Physics*, 49:717, 1977.

[11] P. H. Frampton and T.W. Kephart. Fractionally charged particles as evidence for supersymmetry. *Physical Review Letters*, 49:1310, 1982.

[12] S. M. Bar, D. B. Reiss, and A. Zee. Fractional chrages, monopoles, and peculiar photons. *Physical Review Letters*, 50:317, 1983.

[13] Hong-Wei Yu. Su(8) gut models with stable proton, n anti-n oscillations, fractional charges and low mass monopoles. *Phys. Lett.*, 142B:42, 1984.

[14] Katsuji Yamamoto. Fractionally charged leptons in the so(14) gut. *Phys. Lett.*, 120B:157, 1983.

[15] Fang xiao Dong, Pei you Xue, Tung sheng Tu, and Xian jian Zhou. Fractional charges, monopoles and peculiar photons in so(18) gut models. *Phys. Lett.*, 129B:405, 1983.

[16] A. De Rujula, R.C. Giles, and R.L. Jaffe. Unconfined quarks and gluons. *Phys.Rev.*, D17:285, 1978.

[17] W.R. Leo. *Techniques for Nuclear and Particle Physics Experiments*. Springer-Verlag, Heidelberg, 1987.

[18] M. Mori et al. Search for fractionally charged particles in Kamiokande- II. *Phys.Rev.*, D43:2843–2846, 1991. Kamiokande-II Collaboration.

[19] K. Kawagoe, T. Mashimo, S. Nakamura, M. Nozaki, and S. Orito. An underground search for fractionally charged penetrating particles. *Lett.Nuovo Cim.*, 41:604, 1985.

[20] J. Napolitano et al. Search for fractionally charged particles in cosmic rays at large zenith angles. *Phys.Rev.*, D25:2837, 1982.

[21] M. Aglietta et al. Search for fractionally charged particles in the Mont Blanc LSD scintillation detector. *Astropart.Phys.*, 2:29, 1994.

[22] S. Ahlen et al. The first supermodule of the MACRO detector. *Nuclear Instruments and Methods*, A324:337, 1993.

[23] M. Ambrosio et al. Performance of the MACRO streamer tube system in the search for magnetic monopoles. *Astropart. Phys.*, 4:33, 1995.

[24] S. Ahlen *et al.* Search for slowly moving magnetic monopoles with the MACRO detector. *Phys. Lett. B*, 357:481, 1995.

[25] S. Cecchini *et al.* Relevant parameters for the MACRO experiment. Internal MACRO memo 106/92, University of Bologna, 1992.

[26] S. D. Drell, Norman M. Kroll, Mark T. Mueller, Stephen Parke, and Malvin H. Ruderman. Energy loss of slowly moving magnetic monopoles in matter. *Phys. Rev. Lett.*, 50:644, 1983.

[27] E. Iarocci. Plastic streamer tubes and their applications in high-energy physics. *Nucl. Instr. Meth.*, 217:30, 1984.

[28] G. Battistoni et al. Sensitivity of streamer mode to single ionization electrons. *Nucl. Instr. Meth.*, A235:91, 1985.

[29] Fausto Guarino. Private communication.

[30] R. M. Barnett et al. Review of particle physics. *Phys. Rev.*, D54:1–720, 1996.

[31] Pisa group. Description of the phrase system. Internal MACRO memo, University of Pisa, 1989.

[32] W. E. Earle. A four channel, 200 mhz waveform digitizer with a vmebus interface. Internal MACRO memo 1030/91, Boston University, 1991.

[33] E. Kearns. Readout issues for the new waveform digitizer. Internal MACRO memo 1004/94, Boston University, 1994.

[34] R. Liu. Waveform digitizer stop master. Internal MACRO memo 1005/94, California Institute of Technology, 1994.

[35] C. Arpesella. Data taken by C. Arpesella at the Gran Sasso lab.

[36] *GEANT Detector Description and Simulation Tool.* CERN Geneva, Switzerland, 1993.

[37] Charlie Peck. Private communication.

[38] J.B. Birks. *The Theory and Practice of Scintillation Counting.* Pergamon Press, London, 1964.

[39] R. Liu. The Measurment of the MACRO Scintillator Saturation Constant. Internal MACRO memo 1018/93, California Institute of Technology, 1993.

[40] N. Longley. MACRO coordinate systems and transformations among them. Internal MACRO memo 1020/94, California Institute of Technology, 1994.

[41] INFN Pisa Group. Private communication.

[42] F. Cei. *Search for Neutrinos from Stellar Gravitational Collapse with the MACRO Experiment at Gran Sasso.* PhD thesis, Scuola Normale Superiore Pisa, 1996.

[43] Leif Lonnblad, Carsten Peterson, and Thorsteinn Rognvaldsson. *JETNET 3.0 - A Versatile Artificial Neural Network Package*, 1993.

[44] Leif Lonnblad, Carsten Peterson, and Thorsteinn Rognvaldsson. Mass reconstruction with a neural network. *Physics Letters B*, 278:181–186, 1992.

[45] R. Kantowski and Caren Marzban. A neural network for locating the primary vertex in a pixel detector. *Nucl. Instr. Meth.*, A355:582–588, 1995.